

USING 3D PRINTED DMLS MESOSCALE STRUCTURES TO CONTROL THE ELASTIC  
MODULUS OF A MATERIAL

A thesis presented to the faculty of the Graduate School of Western Carolina University in  
partial fulfillment of the requirements for the degree of Master of Science in Technology.

By

Terail Clonts

Director: Dr. Martin Tanaka  
Associate Professor of Mechanical Engineering  
School of Engineering & Technology

Committee Members: Dr. Scott Pierce, School of Engineering & Technology  
Dr. Sudhir Kaul, School of Engineering & Technology

May 2021

## ACKNOWLEDGMENTS

I would like to thank my committee members and director for their assistance and encouragement. In particular, I would like to thank Dr. Martin Tanaka for his continued support in this endeavor. I also extend sincere thanks to the following people, without whom this thesis would not have been possible: Dr. Paul Yanik, Dr. Patrick Gardner, and Monty Graham. Lastly, I offer my warmest regards and thanks to my parents for their continued support.

## TABLE OF CONTENTS

TABLE OF CONTENTS .....	iii
LIST OF TABLES .....	v
LIST OF FIGURES .....	vi
ABSTRACT .....	viii
CHAPTER ONE: INTRODUCTION .....	1
CHAPTER TWO: LITERATURE REVIEW .....	3
2.1 Current Orthopedic Implant Materials .....	3
2.1.1 Problems with current orthopedic implants.....	4
2.2 Mesoscale Structure Description.....	5
2.3 Advantages of Creating Mesoscale Structures Using DMLS .....	6
2.3.1 A brief history of DMLS.....	7
2.3.2 EOS M 290.....	7
2.4 Normal Stress and Strength .....	8
2.5 Normal Strain, Lateral Strain, and Poisson's Ratio.....	9
2.6 Apparent Elastic Modulus .....	10
2.7 Properties on Human Bone .....	10
2.8 Uniaxial Tensile Testing .....	12
2.9 Statistical Analysis .....	14
CHAPTER THREE: METHODS .....	16
3.1 Specimen Design Approach.....	17
3.2 3D Solid Model Creation of Specimens .....	18
3.2.1 Solid specimen 3D model. ....	18
3.2.2 Cubic unit cell 3D model. ....	19
3.2.3 Cubic specimen 3D model. ....	20
3.2.4 Re-entrant hexagonal unit cell 3D model.....	22
3.2.5 Re-entrant x-axis specimen 3D model. ....	23
3.2.6 Re-entrant y and z-axis specimen 3D models. ....	24
3.3 EOS M 290 Printing Cost Estimation .....	27
3.4 EOS M 290 Printing Preparations .....	28
3.4.1 Generating specimen geometry/support.....	28
3.4.2 Orienting specimens.....	31
3.5 EOS M 290 Specimen Creation .....	33
3.5.1 Removing excess powder from EOS M 290. ....	33
3.5.2 Securing and leveling of build plate on EOS M 290. ....	34
3.5.3 Setting the first layer on EOS M 290.....	35
3.5.4 EOS M 290 printing and removal of build plate. ....	35
3.6 Post-Processing Specimens.....	37
3.6.1 Removing specimens from build plate.....	38
3.6.2 Removing support material from specimens.....	39
3.6.3 Specimen quality evaluation.....	40
3.7 Detailed Testing Procedure.....	47
3.7.1 Tensile testing photos.....	52
3.8 Analysis of Experimental Data .....	71
CHAPTER FOUR: RESULTS .....	72

4.1 Uniaxial Tensile Test Results .....	72
4.1.1 Load vs. deflection curves.....	72
4.1.2 Stress vs. strain curves. ....	77
4.1.3 Average curves. ....	82
4.2 Material Property Results .....	84
4.2.1 Apparent yield strength. ....	85
4.2.2 Elongation at yield. ....	86
4.2.3 Poisson's ratio.....	88
4.2.4 Apparent elastic modulus. ....	90
4.2.5 Apparent fracture strength.....	93
4.3 Apparent Elastic Modulus to Volume Ratio .....	95
4.4 Statistical Analysis Results .....	95
CHAPTER FIVE: DISCUSSION.....	101
5.1 Specimen Variant Comparison .....	101
5.2 Apparent Elastic Modulus Comparison to Human Bone/Current Implants .....	106
5.3 Limitations .....	107
CHAPTER SIX: CONCLUSIONS .....	108
REFERENCES .....	110

## LIST OF TABLES

Table 1: Quality Rating of Each Specimen Prior to Tensile Testing .....	46
Table 2: Specimen Tensile Testing Data Collection Sheet .....	50
Table 3: Specimen Tensile Testing Photo File Names .....	51
Table 4: Apparent Yield Strength Results.....	85
Table 5: Elongation at Yield Results .....	87
Table 6: Poisson's Ratio Results .....	89
Table 7: Apparent Elastic Modulus Results .....	91
Table 8: Apparent Fracture Results .....	93
Table 9: Apparent Yield Strength ANOVA .....	96
Table 10: Solid vs. Cubic Apparent Yield Strength t-Test.....	96
Table 11: Summary of P-Values.....	97
Table 12: Apparent Human Bone Apparent Elastic Modulus Comparison .....	106

## LIST OF FIGURES

Figure 1: EOS M 290 Used for Specimen Creation (photo taken by Terail Clonts) .....	8
Figure 2: Example of Load vs. Deflection Curve (created by Terail Clonts) .....	13
Figure 3: Example of Stress vs. Strain Curve (created by Terail Clonts) .....	14
Figure 4: Dimensions of Rectangular Dog-Bone Specimens (created by Terail Clonts) .....	18
Figure 5: Solid Specimen PRT File .....	18
Figure 6: Solid Specimen Cross-Sectional Area.....	19
Figure 7: Cubic Unit Cell PRT File .....	20
Figure 8: Cubic Specimen PRT File .....	21
Figure 9: Cubic Specimen Cross-Sectional Area .....	21
Figure 10: Re-Entrant Unit Cell PRT File.....	22
Figure 11: Re-Entrant x-Axis Specimen .....	23
Figure 12: Re-Entrant x-Axis Specimen Cross-Sectional Area .....	24
Figure 13: Re-Entrant y-Axis Specimen .....	25
Figure 14: Re-Entrant z-Axis Specimen .....	25
Figure 15: Re-Entrant y-Axis Specimen Cross-Sectional Area .....	26
Figure 16: Re-Entrant z-Axis Specimen Cross-Sectional Area.....	26
Figure 17: Microsoft Excel Spreadsheet Cost Estimator .....	27
Figure 18: Solid Specimen SLI File of Geometry/Block Support.....	29
Figure 19: Cubic Specimen SLI File of Geometry/Block Support.....	30
Figure 20: Re-Entrant x, y, z-Axes SLI Files of Geometry/Block Support .....	31
Figure 21: EOS Print 2 Specimen Build Plate Orientation .....	32
Figure 22: EOS M 290 Build Chamber after Cleaning Powder (photo taken by Terail Clonts)...	34
Figure 23: EOS M 290 Build Plate First Failed Print Attempt (photo taken by Terail Clonts) ....	37
Figure 24: Removing Specimens Using a Vertical Bandsaw (photo taken by Terail Clonts) .....	38
Figure 25: Removing Support Material from Specimen (photo taken by Terail Clonts) .....	39
Figure 26: Emery Cloth Used to Deburr Specimens (photo taken by Terail Clonts) .....	40
Figure 27: Post-processed Solid Specimen (photo taken by Terail Clonts).....	41
Figure 28: Post-processed Cubic Specimen (photo taken by Terail Clonts).....	42
Figure 29: Post-Processed Re-Entrant x-Axis Specimen (photo taken by Terail Clonts) .....	43
Figure 30: Post-Processed Re-Entrant y-Axis Specimen (photo taken by Terail Clonts) .....	44
Figure 31: Post-Processed Re-Entrant z-Axis Specimen (photo taken by Terail Clonts).....	45
Figure 32: Instron 5967 Series Used for Tensile Testing (photo taken by Terail Clonts) .....	47
Figure 33: A2 before (A) and after (B) Tensile Testing (photos taken by Terail Clonts) .....	52
Figure 34: A3 before (A) and after (B) Tensile Testing (photos taken by Terail Clonts) .....	53
Figure 35: A4 before (A) and after (B) Tensile Testing (photos taken by Terail Clonts) .....	54
Figure 36: A5 before (A) and after (B) Tensile Testing (photos taken by Terail Clonts) .....	55
Figure 37: E2 before (A) and after (B) Tensile Testing (photos taken by Terail Clonts) .....	56
Figure 38: E3 before (A) and after (B) Tensile Testing (photos taken by Terail Clonts) .....	57
Figure 39: E4 before (A) and after (B) Tensile Testing (photos taken by Terail Clonts) .....	58
Figure 40: E5 before (A) and after (B) Tensile Testing (photos taken by Terail Clonts).....	59
Figure 41: C2 before (A) and after (B) Tensile Testing (photos taken by Terail Clonts).....	60
Figure 42: C3 before (A) and after (B) Tensile Testing (photos taken by Terail Clonts).....	61
Figure 43: C4 before (A) and after (B) Tensile Testing (photos taken by Terail Clonts).....	62
Figure 44: D2 before (A) and after (B) Tensile Testing (photos taken by Terail Clonts) .....	63

Figure 45: D3 before (A) and after (B) Tensile Testing (photos taken by Terail Clonts) .....	64
Figure 46: D4 before (A) and after (B) Tensile Testing (photos taken by Terail Clonts) .....	65
Figure 47: D5 before (A) and after (B) Tensile Testing (photos taken by Terail Clonts) .....	66
Figure 48: B2 before (A) and after (B) Tensile Testing (photos taken by Terail Clonts).....	67
Figure 49: B3 before (A) and after (B) Tensile Testing (photos taken by Terail Clonts).....	68
Figure 50: B4 before (A) and after (B) Tensile Testing (photos taken by Terail Clonts).....	69
Figure 51: B5 before (A) and after (B) Tensile Testing (photos taken by Terail Clonts).....	70
Figure 52: Solid Specimen Load vs. Deflection .....	73
Figure 53: Cubic Specimen Load vs. Deflection.....	74
Figure 54: Re-Entrant x-Axis Specimen Load vs. Deflection.....	75
Figure 55: Re-Entrant y-Axis Specimen Load vs. Deflection.....	76
Figure 56: Re-Entrant z-Axis Specimen Load vs. Deflection .....	77
Figure 57: Solid Specimen True Stress vs. Strain .....	78
Figure 58: Cubic Specimen Apparent Stress vs. Strain .....	79
Figure 59: Re-Entrant x-Axis Specimen Apparent Stress vs. Strain .....	80
Figure 60: Re-Entrant y-Axis Specimen Apparent Stress vs. Strain .....	81
Figure 61: Re-Entrant z-Axis Specimen Apparent Stress vs. Strain .....	82
Figure 62: Mesoscale Specimen Average Load vs. Deflection .....	83
Figure 63: Mesoscale Specimen Average Apparent Stress vs. Strain .....	84
Figure 64: Apparent Yield Strength Comparison .....	86
Figure 65: Elongation at Yield Comparison.....	88
Figure 66: Poisson's Ratio Comparison.....	90
Figure 67: Apparent Elastic Modulus Comparison .....	92
Figure 68: Apparent Fracture Strength Comparison.....	94
Figure 69: Apparent Yield Strength t-Test Summary .....	98
Figure 70: Poisson's Ratio t-Test Summary .....	99
Figure 71: Apparent Elastic Modulus t-Test Summary .....	100

## ABSTRACT

### USING 3D PRINTED DMLS MESOSCALE STRUCTURES TO CONTROL THE ELASTIC MODULUS OF A MATERIAL

Terail Wayne Clonts

Western Carolina University (May 2021)

Director: Dr. Martin Tanaka

Direct Metal Laser Sintering (DMLS) is an additive manufacturing (AM) technique that uses a laser to fuse metallic powders by sintering the powder layer by layer. This study used a DMLS machine to print 316L stainless steel parts with varying internal geometries in order to manipulate the elastic modulus of a mesoscale material. Parameters may be established that allow the elastic modulus of a part to be controlled through the mesoscale structure of the material. The ability to control the stiffness of a part is applicable in the creation of orthopedic implants in order to reduce stress shielding. Specimens with differing mesoscale configurations were designed using 3D CAD software and created with DMLS. Uniaxial tensile testing was performed on each specimen in order to determine the elastic modulus. The solid specimen variant had a greater modulus than all variants containing mesoscale structures, and roughly one-fourth the modulus of human bone. The elastic modulus of the mesoscale structures were roughly 1.9 to 3.7 times greater than that of the solid variant. As expected, the Poisson's ratio for the re-entrant hexagonal x-axis-oriented specimen was negative because of the nature of the structure, but this was the only structure that exhibited this behavior. Overall, it was determined that the elastic modulus of a 3D metal part can be controlled using mesoscale design.



## CHAPTER ONE: INTRODUCTION

Joint replacement surgeries are among the most commonly performed procedures in the United States. They are so common, in fact, that they ranked within the top three most common surgeries in the United States during 2019 (Dallas, 2019). According to a study presented by Mayo Clinic in 2014, an estimated 4.7 million Americans had undergone total knee arthroplasty (TKA) and 2.5 million had undergone total hip arthroplasty (THA) and were living with implants (Mayo Clinic, 2014).

Joint replacement surgeries are prevalent throughout the population of the United States; therefore, it is important to explore the negative effects that the surgeries may have on individuals. A primary negative effect of these surgeries is bone deterioration that occurs after the insertion of the orthopedic implant. Bone deterioration may occur in areas that receive unnatural amounts of stress due to the presence of an orthopedic implant. Stress shielding can cause an implant to loosen due to loss of bone in the shielded area (Science Alert, 2007). The ability to reduce effects of stress shielding caused by an orthopedic implant would extend the time before the implant needs replacing.

Stress shielding occurs when loads are carried by the prosthesis and regions of the bone are “shielded” from stress (Cheruvu, Venkatarayappa, & Goswami, 2019). This is problematic because bones that are fixated to the implant will deteriorate because the bones do not receive natural amounts of stress due to the presence of the implant. Prostheses are made from metal alloys, ceramic materials, and/or strong plastics (Surgeons, 2016). The elastic modulus of these materials does not match the modulus of the bone that is being replaced.

The ability to control the elastic modulus of an orthopedic implant could counteract the effects of stress shielding by matching the modulus of the implant and the replaced bone. Elastic modulus values matching those of the implant could be achieved by using mesoscale structures. Mesoscale structures are structures containing features that lie within the mesoscale (0.1 mm and 10.0 mm). Internal mesoscale geometries within the orthopedic implant would allow the elastic modulus of the implant to be controlled. The mesoscale geometries may be varied within areas of an implant that require greater or less amounts of stress.

A production method known as additive manufacturing (AM) could be used to produce these mesoscale structures. AM enables the creation of 3D parts by depositing material, layer by layer, to create the three-dimensional (3D) geometry. AM processes can be used to create parts that are not as easily achieved in existing subtractive manufacturing processes, such as computer numeric control (CNC) machining. Direct Metal Laser Sintering (DMLS) is an AM process that uses a laser to fuse metallic powders by selectively sintering the powder layer by layer. The process may also be referred to as Selective Laser Melting (SLM). The process can produce parts up to 99.5% relative density, which enables the user to create near full density functional parts (AIP Publishing, 2015).

The objective of this study is to determine if the elastic modulus of a metal part can be controlled using mesoscale structures. These structures will be designed using 3D CAD, manufactured using DMLS, and tensile tested. The Poisson's ratio of the re-entrant hexagonal mesoscale structure will also be investigated to determine if it exhibits auxetic behavior.

## CHAPTER TWO: LITERATURE REVIEW

### **2.1 Current Orthopedic Implant Materials**

Orthopedic implants are made from a variety of materials including metal, ceramic, and/or polyethylene (a type of hard plastic) (Douglass E. Padgett & Russel E. Windsor, 2013). Using an implant that has similar mechanical properties to bone is advantageous in orthopedic applications. It is important to select a material with a modulus of elasticity that is close to that of bone. Stainless steel was and continues to be the choice material for a wide range of orthopedic implants. Most of the medical grade stainless steel is an alloy called 316L (Tapscott & Wattowa, 2020).

**2.1.1 Problems with current orthopedic implants.** Over time, an orthopedic implant may move, break, or stop working properly. If this happens, an individual may require additional surgery to repair or replace the implant (U.S. Food & Drug Administration, 2019). The problem results from the deterioration of bone near or in contact with the implant. The elastic modulus of bone is anisotropic, meaning that it changes with direction along the object (Hart, et al., 2017). Titanium alloy implants incorporate other metals in order to reduce the modulus of the metal to 50-70 GPa and therefore more closely approximate the modulus of human bone (Hannon, 2016). However, these elastic modulus values are still roughly 3 to 4 times greater than human bone so there is potential to shield neighboring bone from stresses that they would have otherwise experienced. This is known as stress shielding, which is defined as occurring when some of the loads are taken by the prosthesis and shielded from going to the bone (Cheruvu, Venkatarayappa, & Goswami, 2019). Stress shielding from the implant may cause the neighboring bone to deteriorate, therefore loosening the implant and requiring additional surgeries. The ability to control the elastic modulus of the implant through its internal mesoscale structure design would be beneficial in combating stress shielding in orthopedic implants.

## **2.2 Mesoscale Structure Description**

One must understand the meaning of a mesoscale structure in order to recognize its significance in controlling the modulus of orthopedic implants. The scale of parts in additive manufacturing can be divided into three sub-groups: microscale, mesoscale and macroscale. Mesoscale design features are associated with sizes between 0.1 mm and 5.0 mm; therefore, mesoscale structures are defined as structures containing features that lie within the mesoscale (Chao, 2015). For example, a mesoscale feature exists between the molecular level (microscale) and those features associated with the shape of the part (macroscale). Mesoscale properties are not easily understood because they are too large to be analyzed by microscale tools and are too small to be observed by macroscale tools. A mesoscale material's behavior is difficult to sufficiently simulate due to this fact (Schecker, 2015).

Three different classification methods exist for mesoscale structures: foam structures, 2D lattice structures, and 3D lattice structures. Foam structures may be a closed-cell foam or an open-cell foam structure. 2D lattice structures have high tensile and compression strengths while remaining relatively light. 3D lattice structures have trusses composed of struts and nodes in a 3D repeated arrangement (Tang & Zhao). 3D lattice structures are used to achieve maximum part performance while minimizing weight. The mesoscale structures, cubic and re-entrant hexagonal, used in this study can be classified as 3D lattice structures.

### **2.3 Advantages of Creating Mesoscale Structures Using DMLS**

In order to manufacture mesoscale structures, an AM process such as DMLS could be used. It is important to understand the advantages of the process that make it ideal for the production of mesoscale structures. DMLS is advantageous since it allows for the creation of 3D parts with few limitations to the complexity of the geometry of the part (Lindstrom, 2012). The additive nature of the process allows the user to create parts that contain complex geometries that would not be possible with subtractive manufacturing processes. The complex external geometry of a steel alloy part can be created more easily using an additive metal manufacturing process such as DMLS, rather than a traditional subtractive metal manufacturing process such as Computer Numeric Control (CNC) machines (Linke, 2017). Additionally, the additive nature of the DMLS process allows for the creation of internal mesoscale structures within a part. It would be impossible to create these internal mesoscale structures if a part was created using CNC machines.

An additional advantage of using DMLS to manufacture mesoscale structures is that the weight of the part may be reduced without losing functionality. The ability to manipulate the internal mesoscale structure of a part would allow the designer to remove material from within the part at desired locations, which in turn reduces the weight of the part without sacrificing functionality. In fact, functionality of the part may be improved based on the configuration of the internal mesoscale structure. The medical field uses DMLS to produce knee and hip replacements that require lightweight, complex geometries (Hendrickson, 2015).

**2.3.1 A brief history of DMLS.** An explanation of the history of DMLS is needed in order to understand its significance in creating mesoscale structures. DMLS was born from the creation of Selective Laser Sintering (SLS) in the 1980's at The University of Texas at Austin's Mechanical Engineering Department. The creation of SLS began with an undergraduate student at the university named Carl Deckard. When Deckard was finishing his senior year in 1984 and was making the transition to graduate school, he had developed an idea that involved using a beam of directed energy to melt powdered particles together to create a part. After completing his master's degree in 1986, Deckard chose to pursue a doctorate degree and the University of Texas at Austin and advance the technology. The technology was eventually sold to 3D Systems, Inc. in 1999 who were inventors of a process known as stereolithography (STL) (Lindstrom, 2012).

A German manufacturer known as Electro Optical Systems (EOS) is one of 3D Systems competitors in the additive manufacturing business. EOS is primarily focused on the creation of metal parts using DMLS (EOS, 2017). EOS created the EOS M 290, which was the DMLS machine used in this study.

**2.3.2 EOS M 290.** The EOS M 290 (EOS, New York, New York) was released in 2014 for the additive manufacturing of high-quality metal parts (EOS, 2017). Parts may be produced directly from computer-aided design (CAD) data on a 250mm x 250mm x 325mm build plate. The EOS M 290 also offers a wide range of materials to select from. These materials include various types of metals such as aluminum, stainless steel, tool steel, and some super alloys (EOS, 2017). The material used in this study was 316L stainless steel. Figure 1 displays the EOS M 290 that was used to create 316L stainless steel dog-bone specimens containing mesoscale structures.

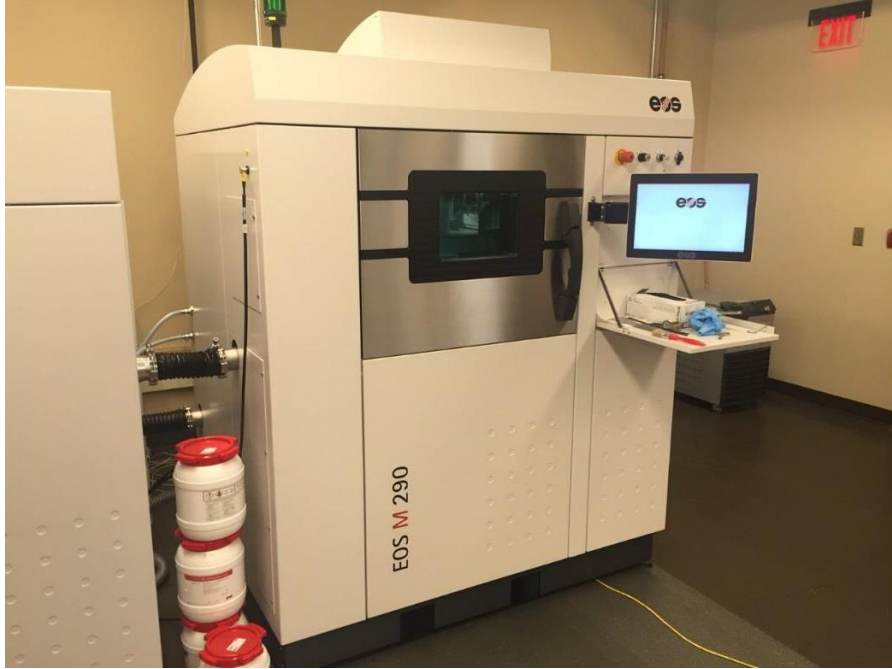


*Figure 1: EOS M 290 Used for Specimen Creation (photo taken by Terail Clonts)*

## **2.4 Normal Stress and Strength**

Stress develops in a material when it is placed under a load. In the case of normal stress, a member is often loaded by an axial force. It can be described by the equation,

$$\sigma = \frac{F}{A} \quad [1]$$

where,  $\sigma$  is the normal stress,  $F$  is the applied force ( $F$ ) and  $A$  is the cross-section. Thus, the stress can be easily calculated for members with regular cross sections under axial loading. The level of stress within a material is more difficult to determine in members with non-uniform cross sections and those that contain structures that are not aligned with the loading direction, like in mesoscale structures. These irregularities can cause bending stress and shear stress in addition to normal stress. It can also cause stress concentrations to develop, increasing stress in some areas (Science Direct, 2021).



The yield strength of a part refers to the maximum stress that the material can withstand before the part begins to plastically deform. It can be observed as a shift from linear behavior of the stress-strain curve. Fracture strength is defined as the stress level where the part physically separates.

## 2.5 Normal Strain, Lateral Strain, and Poisson's Ratio

A material property known as normal strain is defined as the response of a material when placed under normal stress (NDT Resource Center, 2018). When a material is placed under a loading condition such as tension, the resulting stress causes the material to deform. Normal strain ( $\epsilon$ ) is a unitless number and can be described in the equation below as the ratio of the change in length of the material ( $\Delta L$ ) to the original length of the material ( $L$ ). Axial strain describes the deformation along the axis that the load is applied, while lateral strain describes the deformation transverse to the loading direction.

$$\epsilon = \frac{\Delta L}{L} \quad [2]$$

An additional material property of interest in this study is Poisson's ratio. Poisson's ratio is defined as the negative of the ratio of the lateral strain to the axial strain for a uniaxial stress state (Engineers Edge, 2020). The length of a part will increase along the axis in response to an applied tensile load. For the volume of the part to remain constant, the lateral dimension of the part must decrease when the tensile load is applied. The ratio of lateral to axial strain is known as Poisson's and can be viewed in the equation below where Poisson's ratio ( $\nu$ ) is the negative ratio of lateral strain ( $\epsilon_{lateral}$ ) to axial strain ( $\epsilon_{axial}$ ).

$$\nu = - \frac{\epsilon_{lateral}}{\epsilon_{axial}} \quad [3]$$

An interesting characteristic of mesoscale structures is their ability to have a negative Poisson's ratio. The hourglass shape of the re-entrant hexagonal mesoscale structure in this study will result in an increase in the both the axial and lateral dimensions when a tensile load is applied (Zhang & Yang, 2016). Other materials like this exist and are known as anti-rubber, dilation materials, or auxetic materials (University of Wisconsin-Madison, 2017). Different variations of polymers have been produced in previous studies, like polyethylene and polypropylene variants, that exhibit auxetic behavior like the re-entrant hexagonal structure in this study (Hu & Zulifqar, 2017).

## **2.6 Apparent Elastic Modulus**

A material property known as Young's modulus, a.k.a, the elastic modulus, refers to the ability of a material to resist elastic deformation in response to an applied force (Burnett, 2016). The equation below describes Young's modulus ( $E$ ) as a ratio of stress ( $\sigma$ ) to strain ( $\epsilon$ ).

$$E = \frac{\sigma}{\epsilon} \quad [4]$$

It is important to consider the apparent elastic modulus when analyzing a material that contains mesoscale structures. While the true modulus is a property of the material, the apparent modulus takes into account open volume within the cross-section. As a result, the apparent elastic modulus of a mesoscale structure will be less than the modulus of a solid structure (Straffellni, Fontanari, & Molinari, 1999).

## **2.7 Properties on Human Bone**

Human bone is generally classified into two types: cortical bone and trabecular bone. Cortical bone is also known as compact bone and trabecular bone is also known as cancellous or spongy bone. Cortical bone is primarily found in the shaft of the bone and the outer shell at the end of the joints. Trabecular bone is found inside the bone at the end of the joints, beneath the cortical bone. Cortical bone is much denser than trabecular bone (University of Michigan, n.d.).

The true and apparent elastic modulus of cortical and trabecular bone can be identified for comparison to the modulus of the 316L stainless steel specimens created in this study. The distinction between true and apparent elastic modulus lies within the cross-sectional area used for the calculation. The apparent elastic modulus includes the area of the pores within the cross-section and applies to the bone in its entirety, including the cortical and trabecular aspects. The true elastic modulus excludes the cross-sectional area of the pores and is specific to each, the cortical or trabecular, aspect of the bone tissue (Morgan, Unnikrisnan, & Hussein, 2018).

According to a study in the Journal of Biomechanics (Rho, Ashman, & Turner, 1991), the true elastic modulus of cortical bone was 20.7 GPa. The study also found that the true elastic modulus of trabecular bone was 14.8 GPa. These values are the moduli of each particular aspect of the bone tissue. An additional study in the Journal of Biomechanics found that the apparent elastic modulus of a human radius was 16 GPa (Bosisio, Talmant, Skalli, Laugier, & Mitton, 2006). This value is the elastic modulus of the bone in its entirety and accounts for both the cortical and trabecular bone tissue. Being that the cortical aspect of the bone tissue has a higher modulus than the trabecular aspect, the fact that the apparent modulus of bone lies between the true values of each aspect is reasonable. Ideally, the elastic modulus of the cubic and re-entrant hexagonal mesoscale structures would match that of bone.

Human bone is a porous material instead of a solid, much like a mesoscale structure, therefore it is important to consider the true and apparent densities of the materials. True density is defined as the quotient of mass over the volume of a material without consideration of pores. True density involves the true volume of a material, without the volume of the pores within the material. Apparent density is defined as the relationship between the mass and volume of a material, including the pores. The apparent volume is used in calculating the apparent density, which includes the volume of the pores within the material (Rodriguez-Ramirez, Mendez-Lagunas, & Torres, 2012).

## 2.8 Uniaxial Tensile Testing

An understanding of uniaxial tensile testing is needed because it was performed on specimens created in this study to measure mechanical property values. During uniaxial tensile testing, a sample is placed under an axial load in tension until failure is reached (Instron, 2017). Uniaxial tensile testing is performed on a tensile testing machine such as the Instron 5967 Series Universal Testing Machine used in this study. The Instron will generate a load vs. deflection curve for the specimen similar to the illustration below in Figure 2.

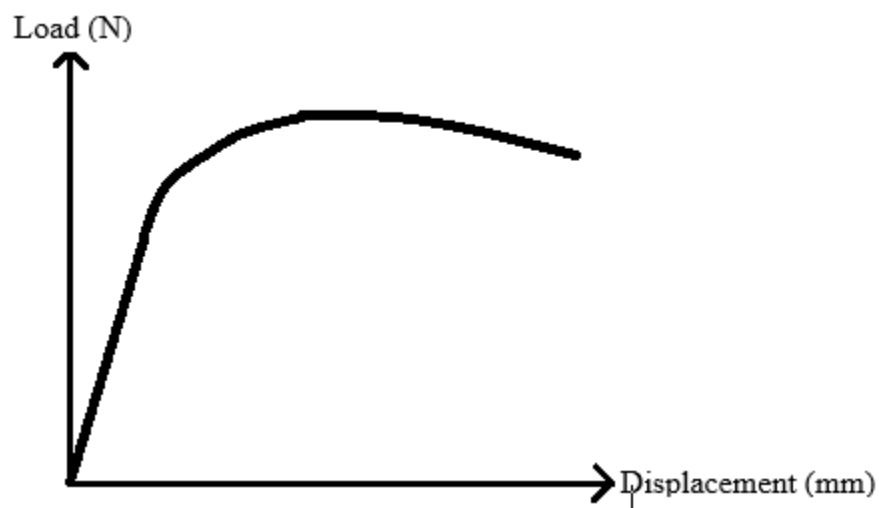
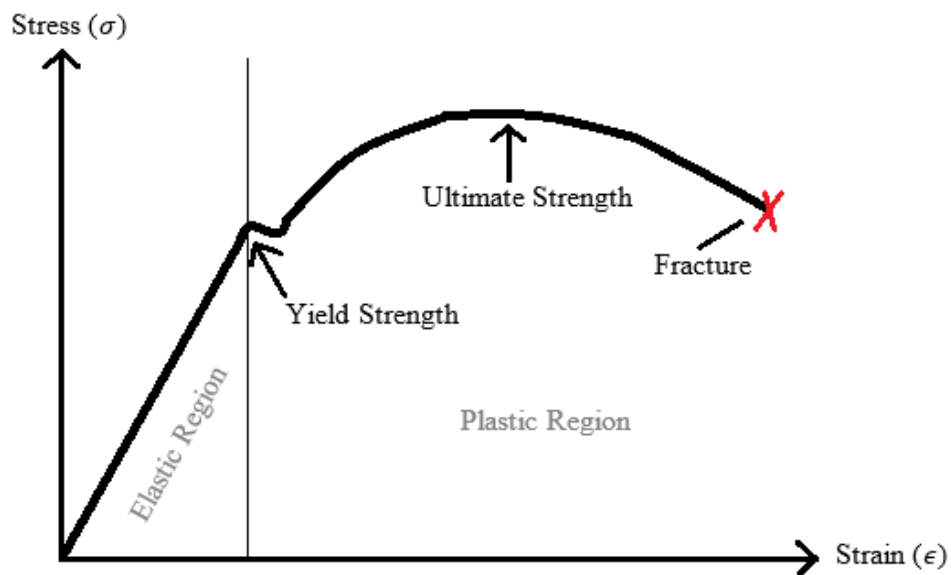


Figure 2: Example of Load vs. Deflection Curve (created by Terail Clonts)

The Instron will also export a Microsoft Excel Spreadsheet containing load and displacement data for the specimen that was tested. Using these values, one can generate a stress vs. strain curve for the specimen. The stress vs. strain curve will display the values of the mechanical properties of interest in this study. The curve also displays the elastic and plastic deformation regions of the specimen that was tested. Elastic deformation is referred to as the region in which a part may yield without deforming. The slope of the curve within this region represents the elastic modulus of the material. Plastic deformation is the region to the left of the yield strength in which a part will no longer return to its original length once unloaded. The fracture strength of the specimen is displayed on the curve as well, which represents the stress at which the specimen is broken in half. A stress vs. strain curve similar to the one that can be created from the Instron load and deflection data exported in the Microsoft Excel Spreadsheet is illustrated below in Figure 3.



*Figure 3: Example of Stress vs. Strain Curve (created by Terail Clonts)*

## **2.9 Statistical Analysis**

A one-way Analysis of Variance (ANOVA) is a statistical method used to determine the statistical difference between the means of three or more groups. In an ANOVA, a F-statistic is produced that measures if the means of different samples are statistically significant by using the ratio between group variability to within group variability. This value can then be compared to a F-critical value in order to determine statistical difference. A significance level, alpha, is chosen prior and set at 0.5, typically. A p-value is also calculated and compared to the alpha value in order to determine the probability of getting a result at least as extreme as the one that was observed. The F-statistic should be used alongside the p-value when deciding if the results are statistically significant. Something is significant if the F-statistic is larger than the F-critical value, however all of the results are significant if the p-value is less than the alpha value. We can reject the null hypothesis if the p-value is less than the alpha value (Statistics How To, 2021).

An ANOVA does not tell which specific groups differed, therefore post hoc t-tests were needed. A t-test is a type of inferential statistics that is used to determine whether there is a significant difference between the means of two groups (Siegle, n.d.). It is used to state with some certainty that the difference between the means of the two groups is not due to random chance.

The probability of a particular outcome can be identified when the dependent variable is assumed to fit a normal distribution. A significance level,  $\alpha$ , is chosen prior and set at 0.5, like in the ANOVA. A t-test calculates a t value that is then compared to a critical t value found on a table in order to determine if the difference between the means of two groups are statistically significant (PennState, 2021). A p-value less than or equal to  $\alpha$  would result in rejecting the null hypothesis and accepting the alternative hypothesis. The null hypothesis states that there is not a statistical difference between the means of the two groups, while the alternative hypothesis states that there is.

A two-tailed, independent samples t-test was used in this study to determine if the mesoscale structure had a statistical significance on the mechanical properties that were measured. The independent samples t-test compares the means of two independent groups. A two-tailed t-test places the region of rejection, the p-value, on both sides of the sampling distribution.

## CHAPTER THREE: METHODS

Five variations of dog-bone tensile testing samples were created so that their elastic moduli could be determined. These structures were designed using 3D CAD, manufactured using DMLS, and tensile tested. An outline of the objectives that were completed during this study is provided below:

- a) The dog-bone specimen geometry was selected, and five varying mesoscale structures were designed. A 3D solid model of each of the five specimen variants was then created.
- b) DMLS was used to create each of the five variants of specimens. Five specimens of each variation were created, resulting in a total of twenty-five specimens. The material used to create the specimens was 316L Stainless Steel.
- c) A tensile test was performed on each of the specimen variants in order to measure their elastic modulus.



### 3.1 Specimen Design Approach

The American Society for Testing and Materials' (ASTM) A 370 – 08a standard was used as a referenced when designing the specimens. This document includes standard test methods and definitions for mechanical testing of steel products including 316L Stainless Steel used in this study. The sub-size 6mm wide rectangular specimen was selected as the preferred geometry for testing. The geometry was chosen with consideration that the Instron 5960 Series Universal Testing Machine used in this study has a maximum force capacity of 30 kN. Calculations were made in order to determine the maximum width and thickness of the 316L Stainless Steel rectangular cross-section that would allow the specimen to reach failure. The calculations were performed in order to determine the maximum allowable width and thickness of the rectangular cross-section of the test specimen are shown below. The maximum allowable width of a square cross-section was determined to be 7.86 mm. The dimensions of the specimens used in this study are shown below as well (Figure 4).

$$A_{cross-section} = \frac{F_{Instron}}{\sigma_{316L\ Stainless\ Steel}}$$

$$A_{cross-section} = \frac{30,000\ N}{485\ N/mm^2}$$

$$A_{cross-section} = 61.86\ mm^2$$

$$l = \sqrt{A_{cross-section}}$$

$$l = \sqrt{61.86\ mm^2}$$

$$l = 7.86\ mm$$

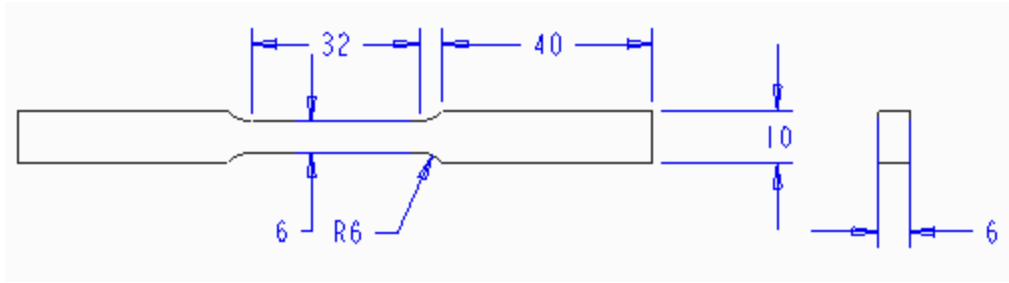


*Figure 4: Dimensions of Rectangular Dog-Bone Specimens (created by Terail Clonts)*

### 3.2 3D Solid Model Creation of Specimens

Each of the five specimen variants were then modeled in Creo Parametric 3.0 (PTC, Boston, Massachusetts). A Parametric Technology Corporation (PRT) file was generated for each specimen variant after saving the created 3D solid model. The PRT files could then be saved as various other file types. These file types could then be imported into software used for analysis and fabrication of specimens.

**3.2.1 Solid specimen 3D model.** The specimen variant with a solid cross-section was created first. The specimen model was created by extruded a single sketch symmetrically along the top datum plane. The volume of the solid structure within the necked down region of the specimen was  $1,152 \text{ mm}^3$ . The PRT file of the solid specimen that was created is shown below in Figure 5. Figure 6 displays the cross-sectional area of the solid specimen, which was  $36 \text{ mm}^2$ .



*Figure 5: Solid Specimen PRT File*

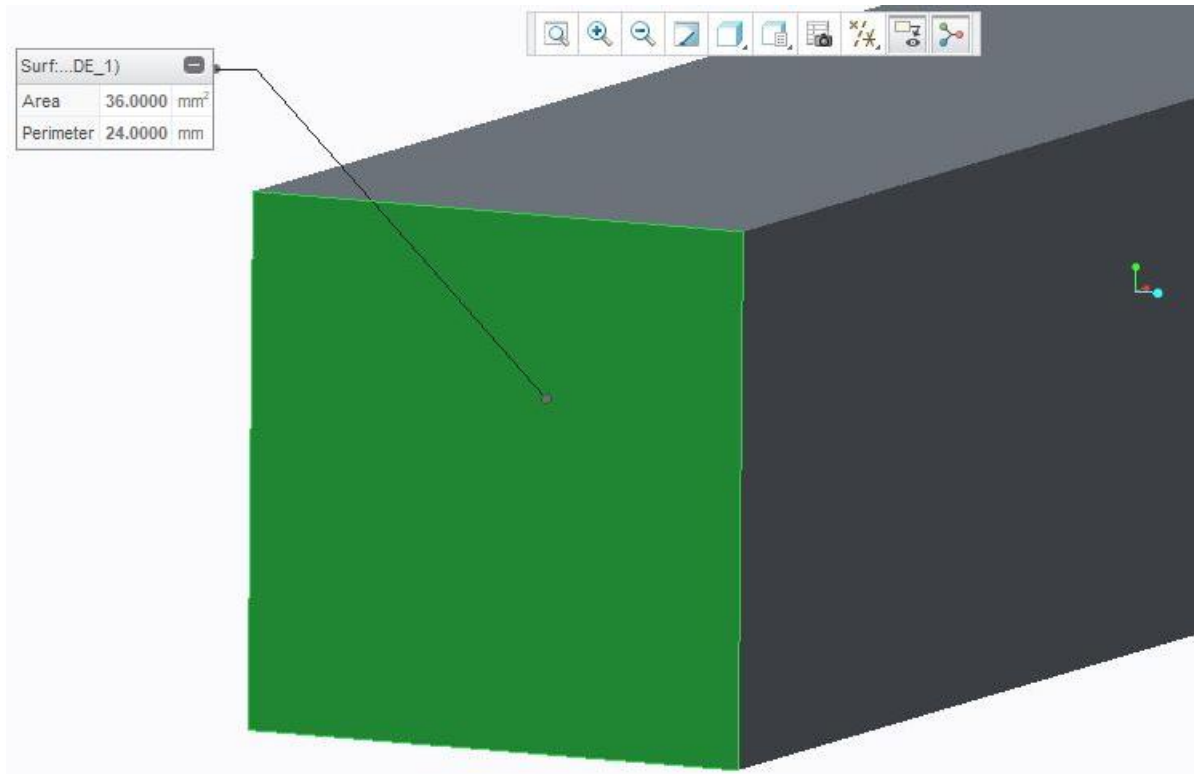


*Figure 6: Solid Specimen Cross-Sectional Area*

**3.2.2 Cubic unit cell 3D model.** The first mesoscale structure model that was created is known as a cubic structure. The modeling of the cubic mesoscale structure began by creating the unit cell. The unit cell consists of twelve square struts arranged in a cubic configuration. The model of the cubic unit cell began by creating a 3 mm extrusion of a 3 mm x 3 mm rectangular sketch. Three rectangular cuts along the x, y and z axes of the extruded rectangle were then made in order to create the desired geometry. The completed PRT file of the cubic unit cell is shown below in Figure 7.

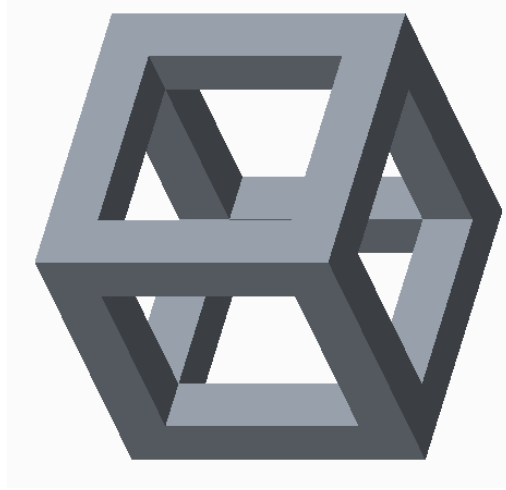


*Figure 7: Cubic Unit Cell PRT File*

**3.2.3 Cubic specimen 3D model.** The cubic unit cell from Figure 8 was then directionally patterned two times in the x and y direction in order to create a 2 x 2 cubic structure. The 2 x 2 cubic structure was then geometrically patterned in the z direction twelve times in order to create a 2 x 2 x 12 cubic structure. Scaling of the 2 x 2 x 12 cubic structure then occurred to ensure that it would fill the 6 mm x 6 mm x 32 mm volume of the reduced section of the sub-size standard specimens. The dimensions of each strut within the cubic structure were  $0.99 \text{ mm}^2 \times 2.01 \text{ mm}$ .

A rectangular cut was then made through the reduced section of the previously created solid specimen model so that the cubic mesoscale structure could be placed within. An assembly was then created, and the 2 x 2 x 12 cubic structure was constrained within the reduced section of the solid specimen model. The volume of the cubic mesoscale structure within the necked down region of the specimen was  $300.6 \text{ mm}^3$ . The PRT file of the cubic specimen that was created in this study is shown below in Figure 8. Figure 9 displays the cross-sectional area of the cubic specimen, which was  $3.888 \text{ mm}^2$ .

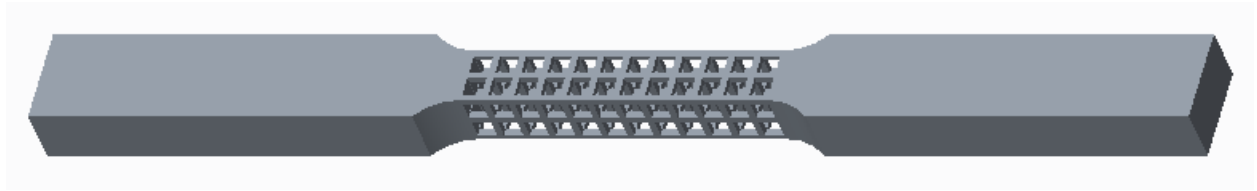


*Figure 8: Cubic Specimen PRT File*

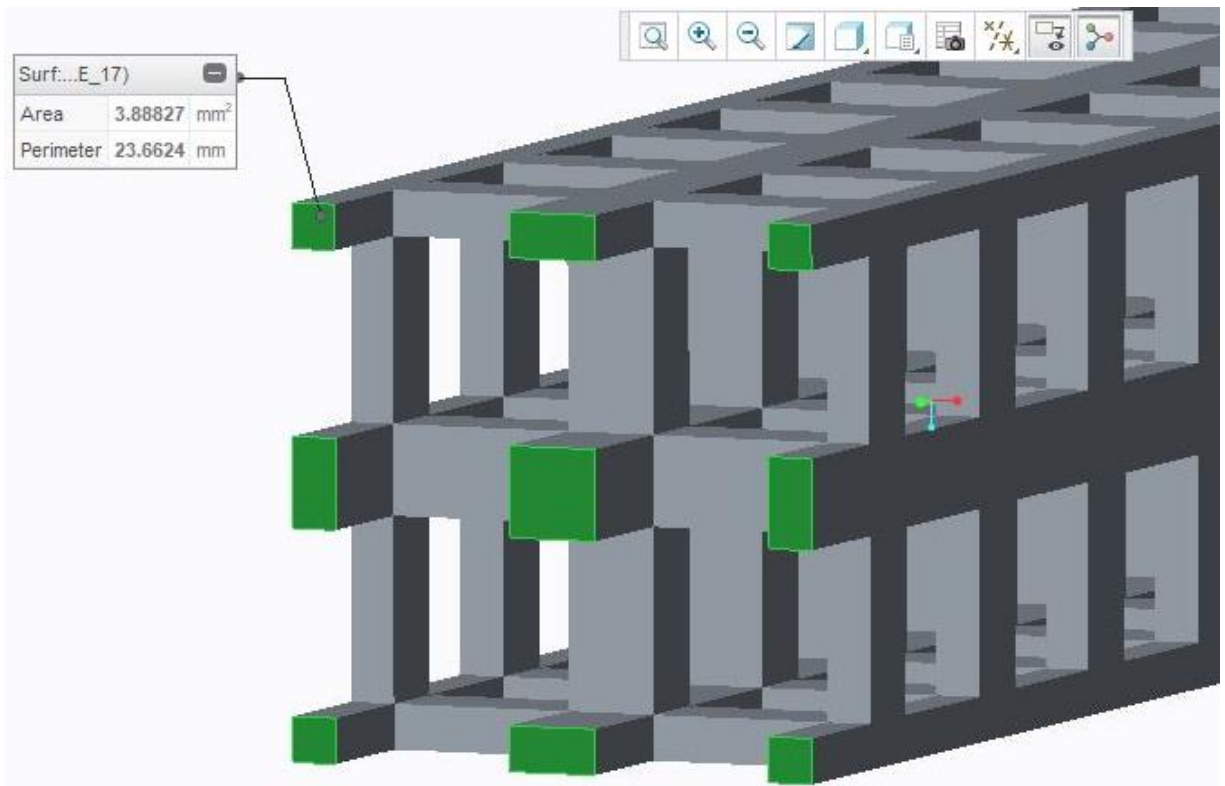


*Figure 9: Cubic Specimen Cross-Sectional Area*

**3.2.4 Re-entrant hexagonal unit cell 3D model.** The second mesoscale structure model that was created is known as a re-entrant hexagonal structure. The modeling of the re-entrant hexagonal mesoscale structure began by creating the unit cell. The unit cell consists of thirty-eight square struts arranged in an inverted hexagonal configuration. The model of the cubic unit cell began as an extruded rectangle in order to create the center strut. A second extruded rectangle was created along the side of the first and patterned radially four times in order to create the center struts. A datum plane was offset from the top plane so that the five existing struts could be mirrored over it. Using the ten existing struts as references, two identical sketches were created on each side of the unit cell and mirrored over each respective plane in order to create the final struts of the cubic cell. The PRT file of the re-entrant hexagonal unit cell is shown below in Figure 10.

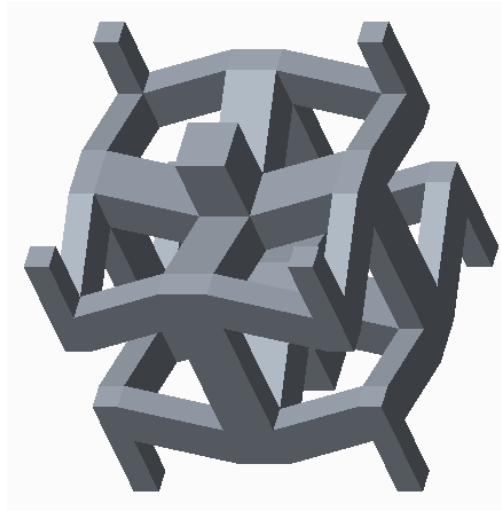


*Figure 10: Re-Entrant Unit Cell PRT File*

**3.2.5 Re-entrant x-axis specimen 3D model.** The re-entrant hexagonal unit cell from Figure 10 was then directionally patterned two times in the x and y direction in order to create a 2 x 2 re-entrant hexagonal structure. The 2 x 2 re-entrant hexagonal structure was then geometrically patterned in the z direction ten times in order to create a 2 x 2 x 10 re-entrant hexagonal structure. Scaling of the 2 x 2 x 10 re-entrant hexagonal structure then occurred to ensure that it would fill the 6 mm x 6 mm x 32 mm volume of the reduced section of the sub-size standard specimens. The dimensions of each strut within the re-entrant hexagonal x-axis-oriented structure were 0.49 mm  $\times$  0.52 mm  $\times$  1.04mm.

A rectangular cut was then made through the reduced section of the solid specimen model so that the re-entrant hexagonal mesoscale structure could be placed within. An assembly was then created, and the 2 x 2 x 10 re-entrant hexagonal structure was constrained within the reduced section of the solid specimen model. The volume of the re-entrant hexagonal x-axis-oriented structure within the necked down region of the specimen was 300.6 mm<sup>3</sup>. The PRT file of the re-entrant hexagonal x-axis-oriented specimen is shown below in Figure 11. Figure 12 displays the cross-sectional area of the re-entrant hexagonal x-axis-oriented specimen, which was 2.171 mm<sup>2</sup>.

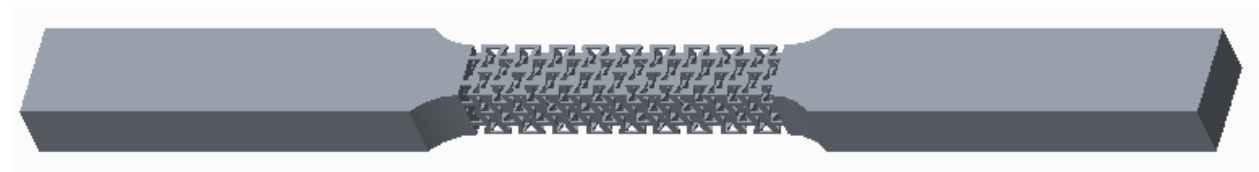


*Figure 11: Re-Entrant x-Axis Specimen*

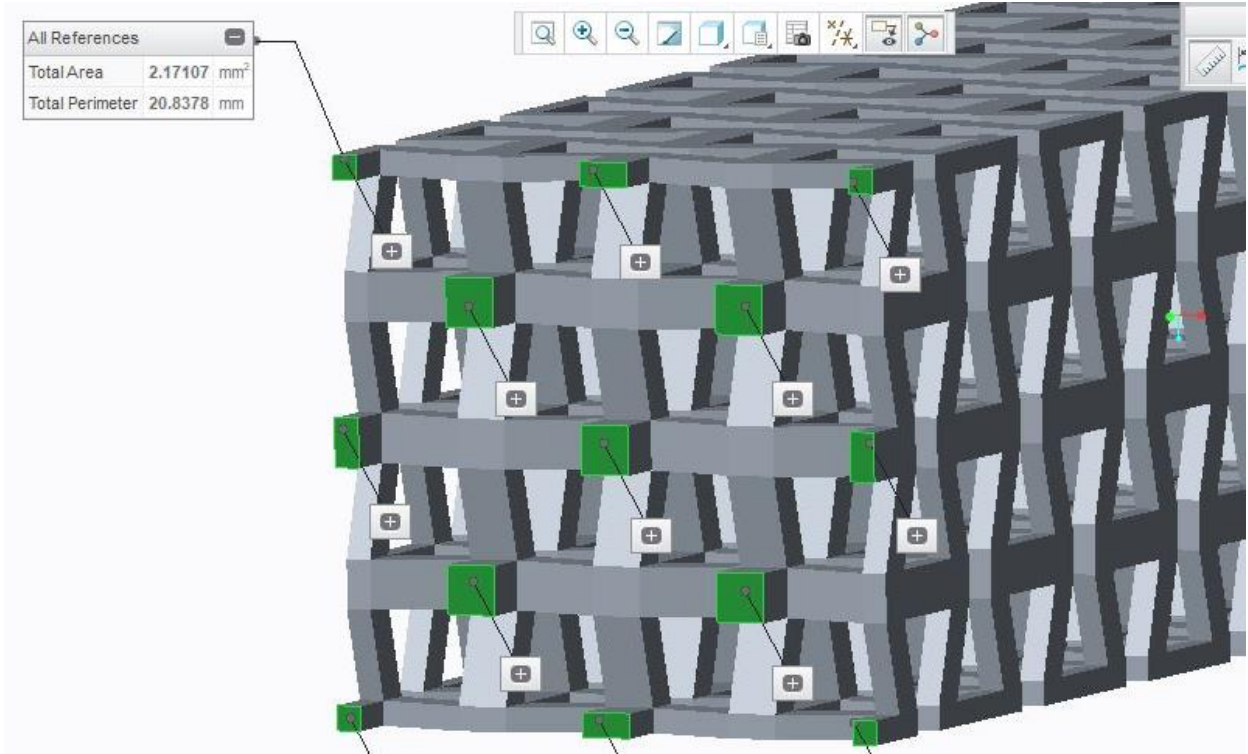


*Figure 12: Re-Entrant x-Axis Specimen Cross-Sectional Area*

**3.2.6 Re-entrant y and z-axis specimen 3D models.** The final two specimen variants were created by orienting the re-entrant hexagonal mesoscale structure along its y-axis and its z-axis and constraining them within the reduced section of the solid specimen model. The dimensions of the struts within both structures were the same as the struts within the x-axis orientation. The volume of both structures within the necked down region of the specimen was the same as well, at  $300.6 \text{ mm}^3$ . The volume of each of the mesoscale structures was designed to be the same so that the only difference between the specimen variants would be the mesoscale structures themselves.



The PRT files of the re-entrant hexagonal y-axis and z-axis-oriented specimen, respectively, are shown below in Figures 13-14. Figure 15 displays the cross-sectional area of the re-entrant hexagonal y-axis-oriented specimen, which was 4.342 mm<sup>2</sup>. Figure 16 displays the cross-sectional area of the re-entrant hexagonal z-axis-oriented specimen, which was 4.342 mm<sup>2</sup>.as well.

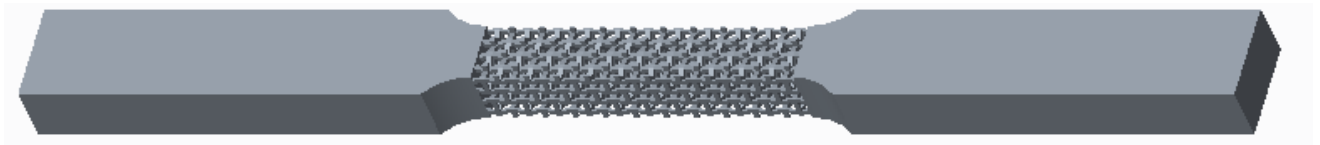


*Figure 13: Re-Entrant y-Axis Specimen*

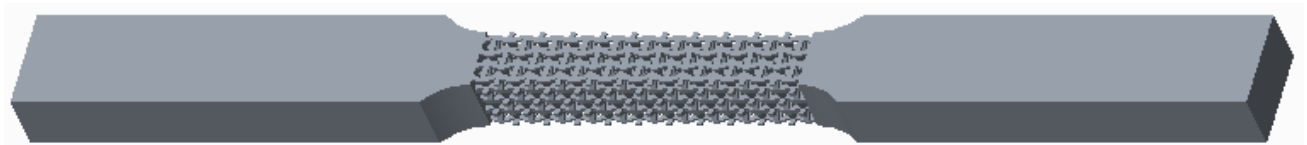


*Figure 14: Re-Entrant z-Axis Specimen*

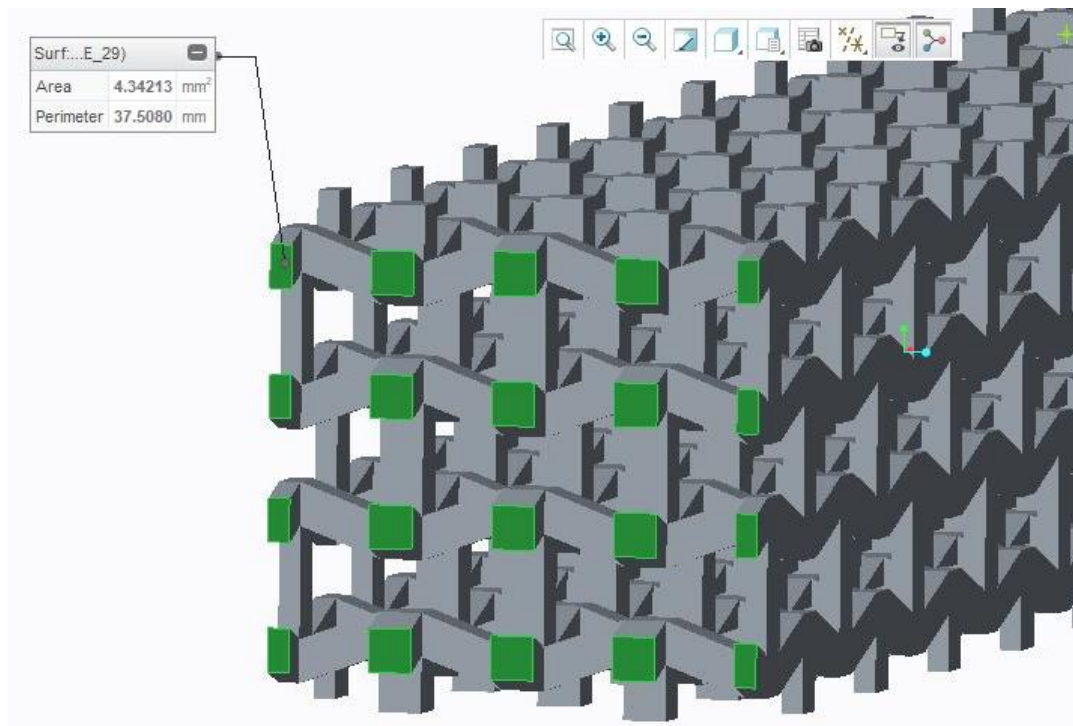


*Figure 15: Re-Entrant y-Axis Specimen Cross-Sectional Area*

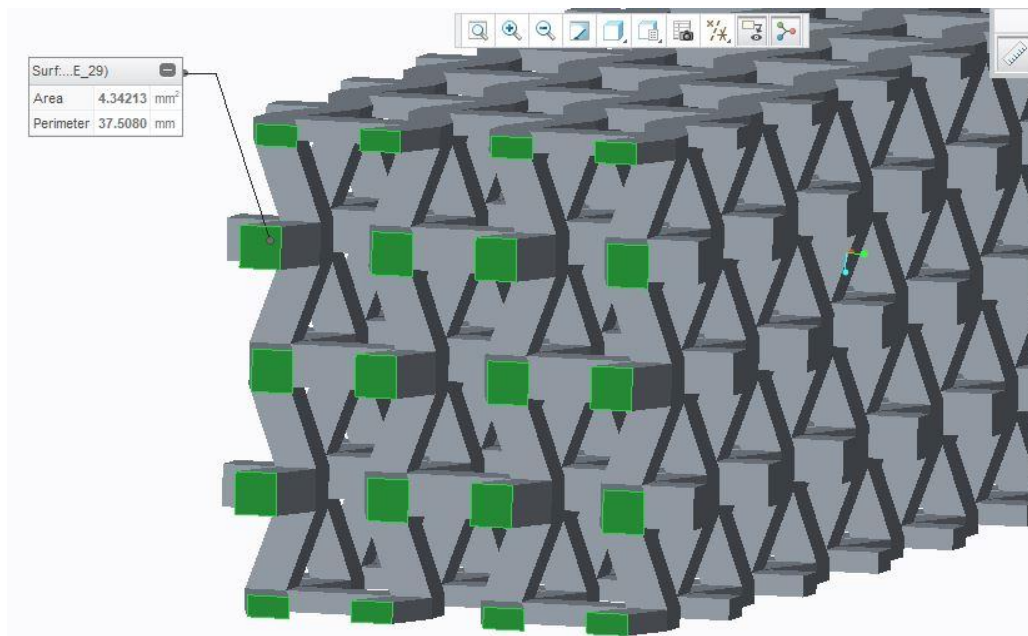


*Figure 16: Re-Entrant z-Axis Specimen Cross-Sectional Area*

Cost estimations were made before printing to ensure that the cost of the print was not above the budget for the project. The total volume of all twenty-five specimens was entered into a Microsoft Excel spreadsheet (154.26 cm<sup>3</sup>), as well as the number of hours that the print will take (32 hours), to determine the total cost of the build. The total cost of the build was determined to be within budget at \$884.65. Permission to begin specimen printing on the DMLS was then given by the Rapid Tooling and Prototyping Center at Western Carolina University. Figure 17 shows the Microsoft Excel spreadsheet cost estimator that was used to determine the total cost of the build.

[illegible]

Figure 17: Microsoft Excel Spreadsheet Cost Estimator

### **3.4 EOS M 290 Printing Preparations**

Creo Parametric 3.0 was then used to save each of the twenty-five specimen's PRT files as an Initial Graphics Exchange Specification (IGES) file so that they could be imported into Materialise Magics for printing. Once imported into Magics, the resulting Slice Layer Interface (SLI) files were then imported again into an additional software known as EOSPRINT 2 that allowed the user to orient the parts upon the build plate of the EOS M 290.

**3.4.1 Generating specimen geometry/support.** Materialise Magics (Materialise, Leuven, Belgium) is the software that was used to generate SLI files for each specimen's geometry and support material. The PRT file for each specimen must be saved as an IGES file in Creo Parametric 3.0 before importing it into Magics.

The SLI file generation for the specimens began by creating a new scene for each specimen variant to be imported into. The IGES file of the solid specimen variant was then imported into Magics. The translate tool was used to elevate the solid specimen seven millimeters off of the build plate in the z-direction. Seven millimeters was chosen to ensure that the support that would later be generated would be thick enough for the specimen to be removed. A vertical band saw was used to remove the specimens from the build plate after completion of the print. This seven millimeter distance was thick enough for the band saw to remove the specimens without cutting into the build plate itself.

The tool to automatically generate support was then selected. The support type that the automatic support generation tool chose was a solid support structure. A solid support structure is not optimal because it makes post-processing more difficult since the solid support is difficult to remove from the part's geometry. The support generation selection was edited and a block support was chosen instead. Block support is preferable to solid support for 316L Stainless Steel parts printed on the EOS M 290. The hatching pattern of block supports are much easier to remove from the geometry of the part after the print has completed since it does not fully contact the bottom surface of the part.

The solid specimen geometry with its block support structure was then exported by clicking on the EOS tab and selecting the destination folder. A folder containing the SLI files of the solid specimen geometry and the block support structure was then created and placed into the selected destination folder. The SLI files of the geometry and the block support that were generated for the solid specimen variant are shown below in Figure 18.

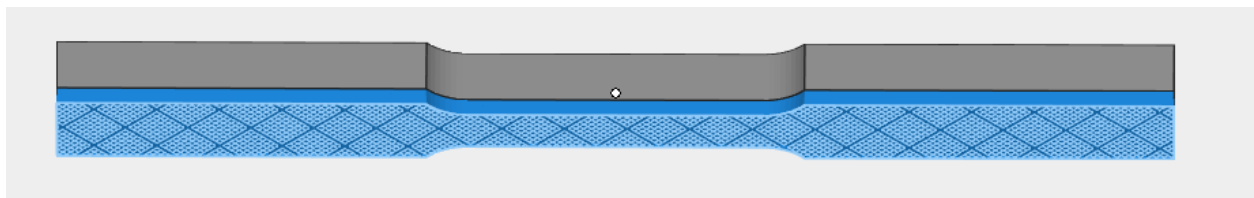


*Figure 18: Solid Specimen SLI File of Geometry/Block Support*

The same process was performed to generate the SLI files for the cubic specimen variant. Part-to-part supports were initially generated between each of the squares of the cubic specimen. These supports were deleted due to the difficulty that they created during post-processing. The spaces between each of the horizontal struts of the cubic structure were too small to allow the part-to-part support to be removed. The cubic specimen was still able to be adequately printed on the EOS M 290 without the part-to-part supports between the horizontal struts of the structure. The SLI files of the geometry and the block support that were generated for the cubic specimen variant are shown below in Figure 19.



*Figure 19: Cubic Specimen SLI File of Geometry/Block Support*

The same process was performed to generate the SLI files for the re-entrant hexagonal specimen variants oriented along their x, y and z-axis. The SLI files of the geometry and the block support that were generated for the re-entrant hexagonal specimen variants oriented along their x, y, and z-axis, respectively, are shown below in Figure 20.

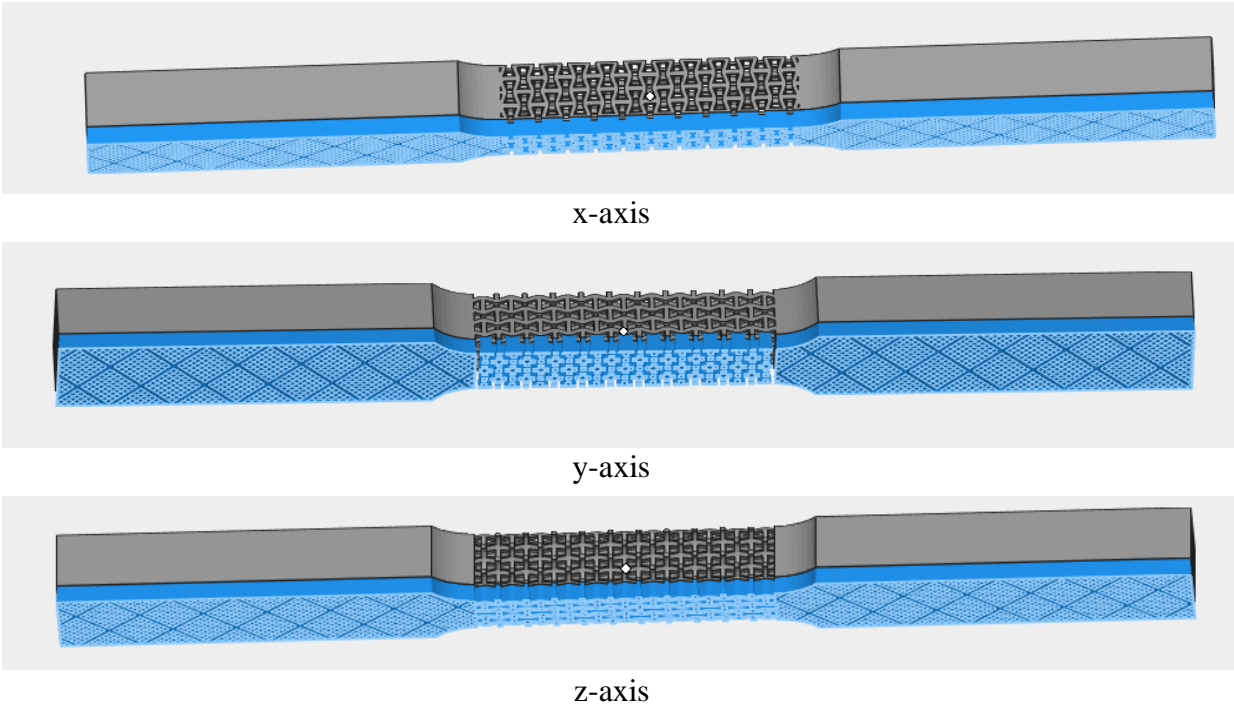


*Figure 20: Re-Entrant x, y, z-Axes SLI Files of Geometry/Block Support*

**3.4.2 Orienting specimens.** The SLI files for the geometries and supports of each of the five variants of specimens were then imported in a software known as EOSPRINT 2 (EOS, New York, New York). This software was used so that the each of the specimen could be oriented upon the build plate of the EOS M 290 in the way in which it would be printed on the machine. Each specimen was placed at a forty-five-degree angle in relation to the recoater blade of the EOS M 290. The purpose of the angle was so that the recoater blade did not contact the entirety of each specimen as it passed from left to right across the build plate while printing the parts. The angle helped minimize the possibility that the recoater blade would contact the specimens during the print and bend them. The particular part that is bent by the recoater blade will often cause the print job to pause. The job may not be continued until that particular failed part upon the build plate is cancelled.

Each of the five variants of specimens were then multiplied five times each once they were oriented at a forty-five-degree angle upon the build plate. The multiplication of each of the five specimens resulted in twenty-five specimens existing on the build plate. The specimen build plate orientation was then saved and exported to the EOS M 290 for fabrication. The orientation of the specimens within the EOSPRINT 2 software is shown below in Figure 21.

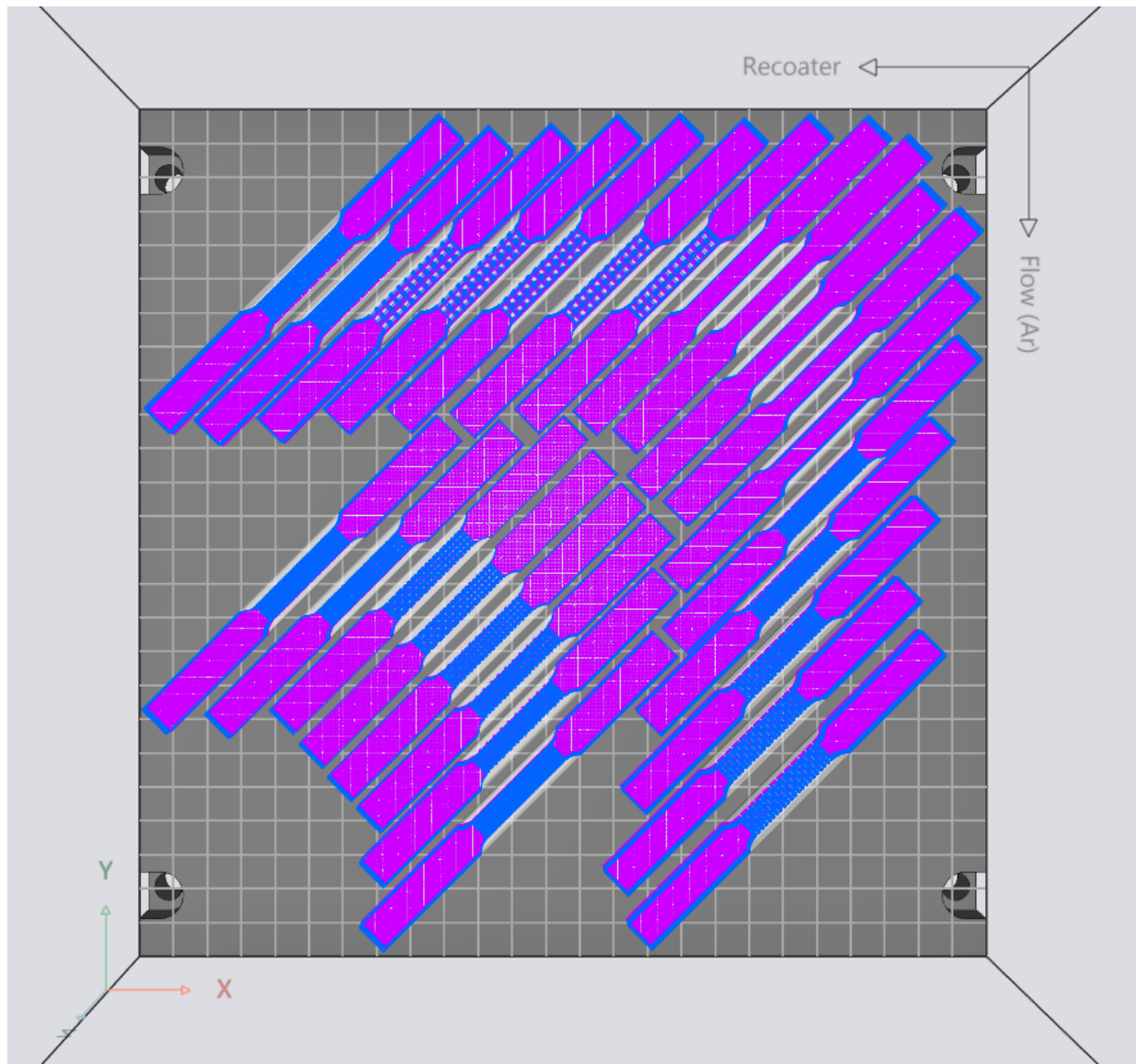


*Figure 21: EOS Print 2 Specimen Build Plate Orientation*



### 3.5 EOS M 290 Specimen Creation

Specimens were then created using the EOS M 290. Default laser power, hatch distance, layer thickness, and scan speed parameters were used during the build. Attention was not given to the values of these parameters because they were known to create successful builds.

Appropriate safety measures were followed while operating the machine. Protective gear that included a respirator, gloves, and safety glasses were worn while operating the machine to avoid inhaling the fine metallic powder which had the consistency of flour. The door to the printing chamber was closed during printing to reduce the risk of explosion.

**3.5.1 Removing excess powder from EOS M 290.** In order to begin printing the specimens, all components of the EOS M 290 were powered on. First, the excess metallic powder from the machine was thoroughly cleaned using the vacuum that was attached. The detachable piece in the front of the machine was cleaned, removed, and placed aside until printing began. The build plate was also removed from the machine. All excess powder from the left chamber was removed and sifted back into the right chamber. A grounded sift was used to remove all condensate from the unused powder. The excess powder within the central chamber that housed the build plate, within the left chamber that housed the excess powder from the previous print, and on the outer edges of the right chamber was cleaned. The recoater blade was then cleaned, as well as the surrounding walls of the build chamber. After all excess powder was cleaned, the lens at the top of the chamber was removed, wiped clean, and reinserted. The inside of the build chamber of the EOS M 290 after cleaning all excess powder is displayed below in Figure 22.

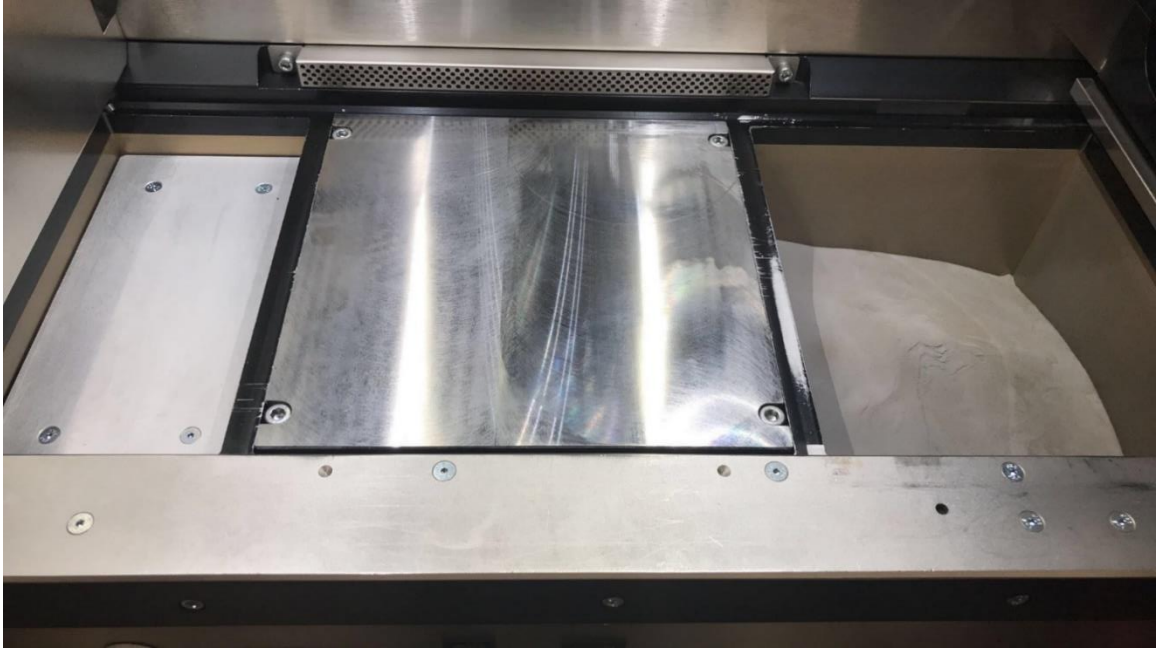


*Figure 22: EOS M 290 Build Chamber after Cleaning Powder (photo taken by Terail Clonts)*

**3.5.2 Securing and leveling of build plate on EOS M 290.** After reinserting the lens, a new build plate was inserted into the machine's central chamber. The plate was secured with screws that were hand tightened. The heat from the process caused the screws to tighten further. The plate was then leveled after it was fixtured to the central chamber mount. A bubble level was used to level the plate from left to right by using the left and right arrows on the machine. When leveling the build plate from forwards to backwards, the recoater blade was moved over the central chamber that houses the secured build plate and the forward and backward arrows on the machine were used. A larger feeler gauge was chosen and slid between the recoater blade and the build plate. The gauge slid easily between the two before the build plate was moved closer to the recoater blade. In order to complete the leveling of the plate, the build plate was continually moved upward towards the recoater blade as increasingly smaller feeler gauges passed between the two.

**3.5.3 Setting the first layer on EOS M 290.** The first layer was set after leveling the build plate. The thickness of the first layer of the print was equivalent to the thickness of each layer within the print. Default layer thickness of 0.1 mm was used for the printing operation in this study. The build plate was lowered away from the recoater blade so that the space between was slightly greater than the desired thickness of the first layer. Feeler gauges were used to determine this desired distance. The recoater blade was returned to its home position and the right chamber was raised upwards enough so that the recoater blade would deposit the metallic powder housed inside over top of the build plate as it traveled from right to left. The recoater blade was manually moved leftwards and powder was deposited onto the build plate. Being that the original distance between the recoater blade and the build plate was known; the build plate was able to be moved upwards in known increments. The recoater blade was repeatedly moved back to its home position and moved leftward in order to evenly distribute the first layer of powder across the plate so that the desired first layer thickness was achieved.

**3.5.4 EOS M 290 printing and removal of build plate.** The printing process was ready to begin once the first layer was set. The detachable piece that was removed during cleaning was replaced. The door to the printing chamber was then closed. The machine then pressurized the chamber, purged oxygen from the chamber, and heated up the build plate. This process takes several minutes. Progression bars were displayed on the machine and appeared green, which indicated that no errors were present. The machine could now begin the printing process.

After the printing process was complete and the machine prompted that printing chamber was able to be opened safely, the excess powder from the central chamber containing the print was sifted into the right chamber. Once most of the powder was sifted, the attached vacuum was used to clean the excess powder from around the parts on the build plate. The build plate was then removed from the printing chamber and the excess powder from the underside of the plate was cleaned.

All twenty-five dog-bone specimens were successfully created using the EOS M 290 on the second printing attempt. The first attempt failed as a result of the recoater blade contacting multiple specimens on the build plate. Orientation of the specimens on the build plate had to be modified prior to the second attempt. Specimens oriented along the top edge of the build plate were offset in a downward fashion so that the recoder blade would gradually contact their surfaces. The build plate containing the first failed attempt of specimens is shown below in Figure 23. The location of the failure can be observed in the upper-left corner of the figure. The failure resulted from the recoder blade directly contacting the surfaces of the specimens oriented along the top edge of the build plate. The orientations of the specimens were modified before the final print so that each of the specimens that were previously oriented along the top edge of the build plate were offset in a downward fashion avoiding direct contact with the recoater blade.

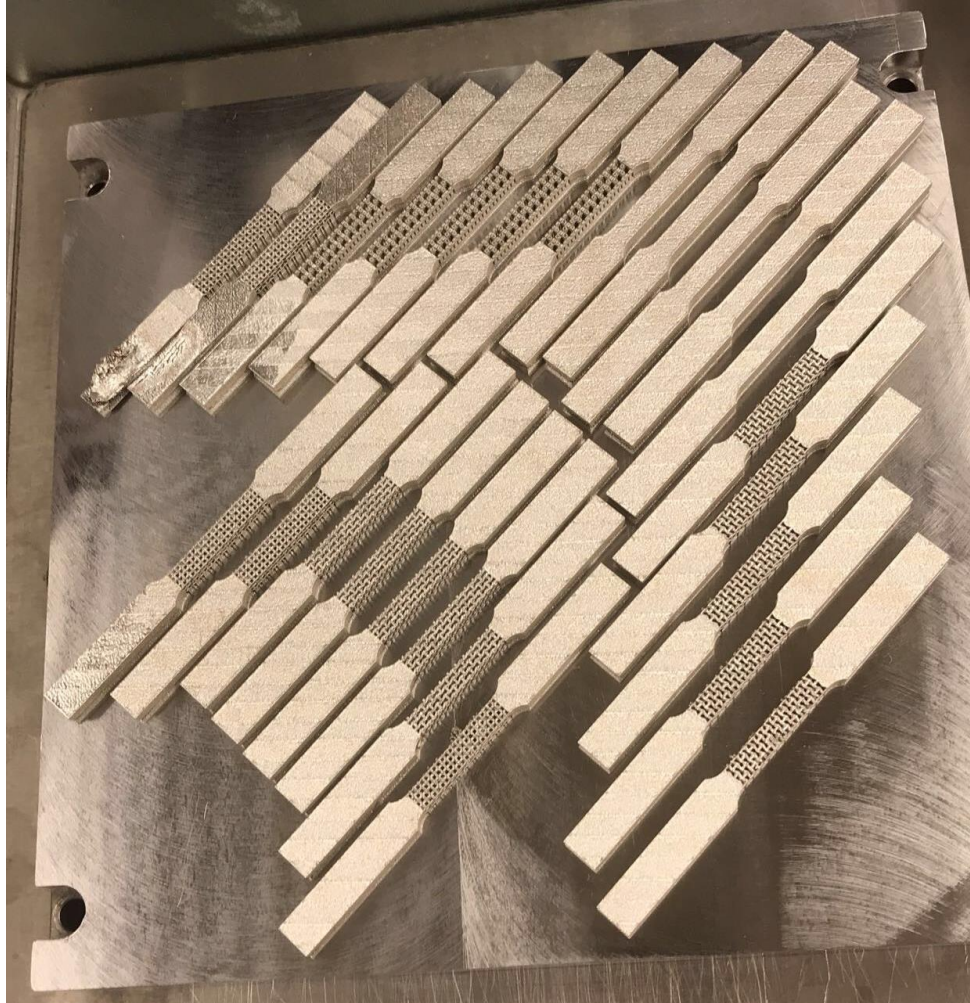


*Figure 23: EOS M 290 Build Plate First Failed Print Attempt (photo taken by Terail Clonts)*

### **3.6 Post-Processing Specimens**

Specimen post-processing began with the removal of the dog-bone specimens from the build plate with a vertical bandsaw. The remaining support material was then removed from each of the specimens and the build plate using a Hass vertical mill located within the machine shop at Western Carolina University. Finally, emery cloth was used to remove any burs from the specimens. Specimens were labeled for identification and the condition of each specimen was recorded. Each step will be described in detail in the following sections.

**3.6.1 Removing specimens from build plate.** The specimens were removed from the build plate using a vertical bandsaw. The build plate was fixtured so that the blade of the bandsaw would contact the surface of the support material. Precautions were taken so that the blade only contacted the support material and did not contact the plate or the specimens. The removal of the specimens from the build plate using a vertical bandsaw is displayed below in Figure 24.



*Figure 24: Removing Specimens Using a Vertical Bandsaw (photo taken by Terail Clonts)*



**3.6.2 Removing support material from specimens.** An initial attempt with a chisel to remove the support material from the specimens resulted in fracturing one of the specimens. A Haas vertical mill was used to remove the support material from the remaining specimens in order to avoid further damage to the remaining specimens. Each of the specimens were fixtured within the mill with the support material facing upward. A face mill tool with eight carbide tipped blades was inserted into the machine and a tool offset of .127 mm was created from the top surface of each specimen. Manual passes of .127 mm were made until the thickness of each specimen was roughly 6 mm. The specimens were un-fixtured periodically during the removal of support material and measured with calipers to ensure their desired thickness was attained. Figure 25 below displays a specimen fixtured inside of the Haas vertical mill during support material removal.



*Figure 25: Removing Support Material from Specimen (photo taken by Terail Clonts)*

Four-hundred grit emery cloth was then used to remove any burs from the specimens. The emery cloth was placed over a file for deburring to avoid further damaging any remaining specimens (Figure 26).



*Figure 26: Emery Cloth Used to Deburr Specimens (photo taken by Terail Clonts)*

**3.6.3 Specimen quality evaluation.** The specimens were assigned a letter (A-E) and a number (1-5). Solid specimens were labeled A1-A5. Cubic specimens were labeled E1-E5. Re-entrant specimens oriented along the x-axis were labeled C1-C5. Re-entrant specimens oriented along the y-axis were labeled D1-D5. Re-entrant specimens oriented along the z-axis were labeled B1-B5. The twenty-five post-processed dog-bone specimens including the solid, cubic, and re-entrant specimen oriented along the x, y, and z-axis, respectively, can be viewed below in Figures 27-31.





*Figure 27: Post-processed Solid Specimen (photo taken by Terail Clonts)*

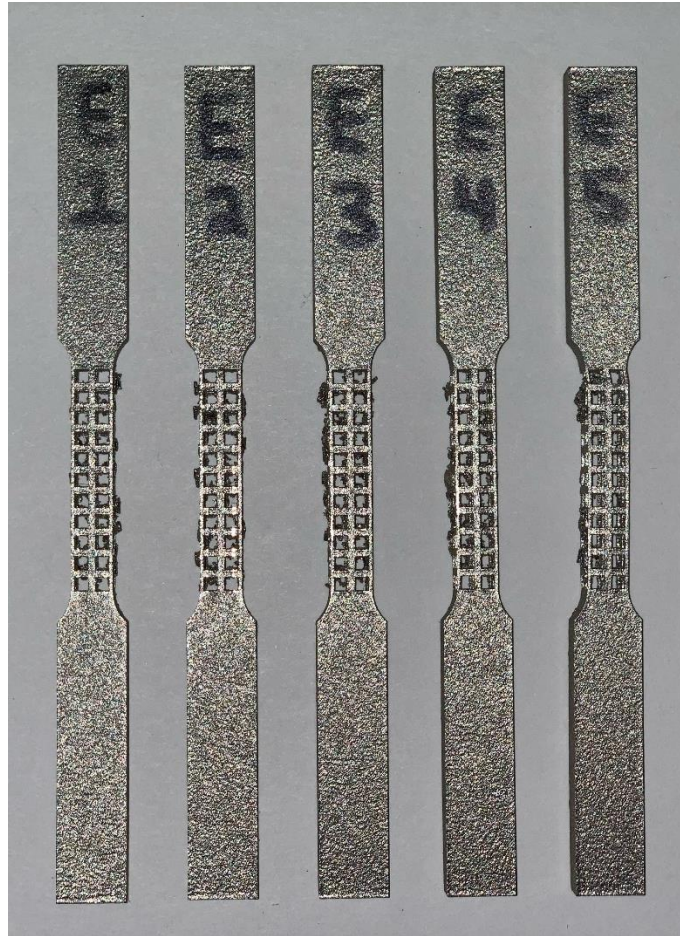


*Figure 28: Post-processed Cubic Specimen (photo taken by Terail Clonts)*



*Figure 29: Post-Processed Re-Entrant x-Axis Specimen (photo taken by Terail Clonts)*



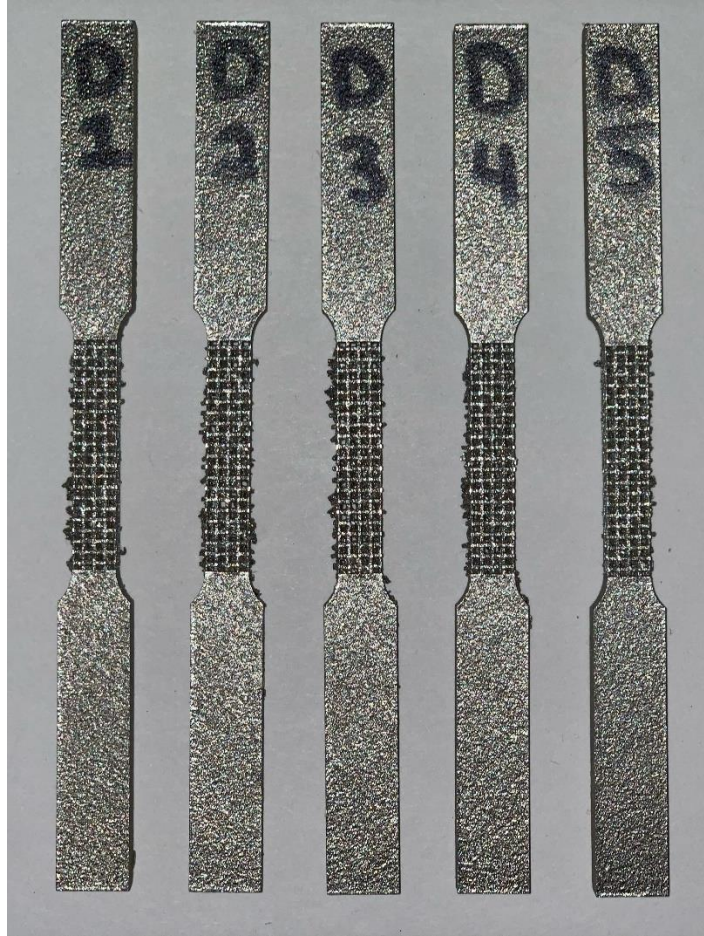


*Figure 30: Post-Processed Re-Entrant y-Axis Specimen (photo taken by Terail Clonts)*

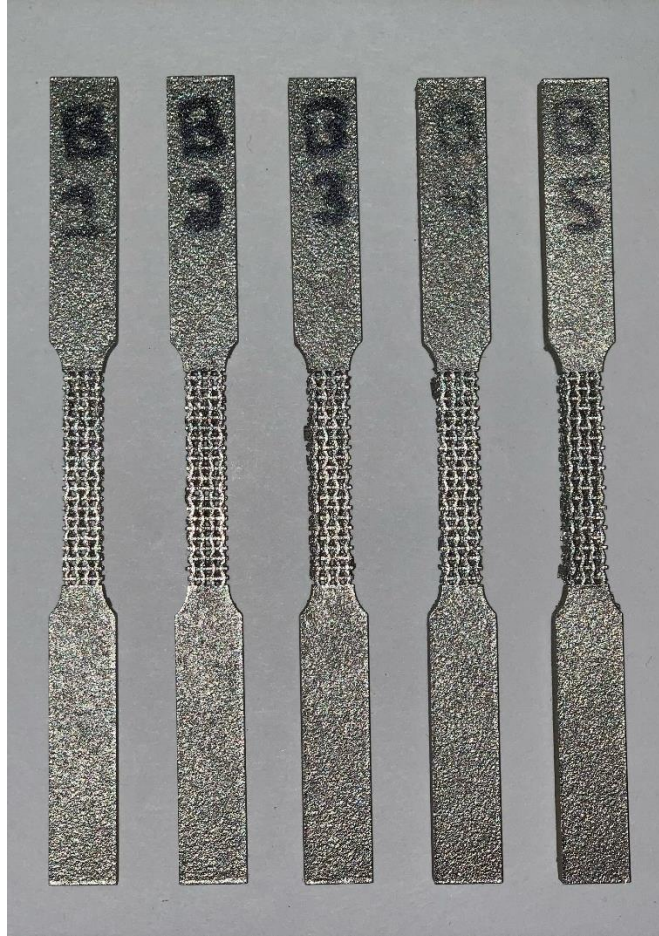


*Figure 31: Post-Processed Re-Entrant z-Axis Specimen (photo taken by Terail Clonts)*

Each specimen was inspected for damage prior to performing tensile testing. A quality rating was assigned to each of the twenty-five specimens. The ratings were referred to after tensile testing was completed in order to explain variation in results. Table 1 displays the quality rating assigned to each of the twenty-five specimens. The quality rating of each specimen ranges from a scale of 1 to 5 and is dependent on the number of struts that are damaged within the mesoscale structure of the specimen. A quality rating of 1 represents a fractured specimen. The remaining ratings are as follows: 2 = Poor (20+ damaged struts), 3 = Fair (10-19 damaged struts), 4 = Good (1-9 damaged struts), and 5 = Excellent (0 damaged struts).

Table 1: Quality Rating of Each Specimen Prior to Tensile Testing

	Specimen Variants				
	Solid	Cubic	Re-entrant x	Re-entrant y	Re-entrant z
A1	1				
A2	5				
A3	5				
A4	5				
A5	5				
E1		1			
E2		4			
E3		4			
E4		4			
E5		3			
C1			1		
C2			3		
C3			3		
C4			4		
C5			1		
D1				1	
D2				2	
D3				2	
D4				2	
D5				2	
B1					1
B2					4
B3					4
B4					4
B5					4

### 3.7 Detailed Testing Procedure

Figure 32 shows the Instron 5967 Series Universal Testing Machine (Instron, Norwood, Massachusetts) that was used to perform tensile testing on the dog-bone specimens. The particular system used in this study had a maximum force capacity of 30 kN. The extensometer was connected to the machine to acquire axial strain data.



*Figure 32: Instron 5967 Series Used for Tensile Testing (photo taken by Terail Clonts)*

Precautions were taken so that the clamping force of the Instron's crosshead did not damage the mesoscale structures within the test specimens. A regulator existed on the machine that allowed for the appropriate clamping force of the crosshead to be reached without deforming the specimens. The regulator was used to increase the clamping force on the grips in increments of ten pounds per square inch (psi) on the regulator. The crosshead of the Instron was then raised after every incremental increase of clamping force until the compressive load on the specimen from the crosshead was eliminated. This process was repeated until the regulator reached 70 psi. The load and deflection were balanced once the final pressure was reached.

Axial strain was measured by a 2630-100 series clip-on extensometer (Instron, Norwood, Massachusetts) attached to each specimen prior to fixturing it within the jaws of the machine. An existing test method that was saved on the computer associated with the Instron was modified to include axial strain data from the extensometer. The extensometer was removed from each specimen before fracture in order to avoid damaging the device. Axial displacement, load, and time data from each test were exported from the Instron to a Microsoft Excel spreadsheet. Each tensile test was paused periodically in order to measure transverse displacement with a caliper.



Permanent deformation occurred to each specimen after undergoing the tensile test, which did not allow it to be tested a second time. The first test needed to be correct, therefore plastic specimens were used in preparation. A specimen, such as specimen C5, that had been previously damaged by post-processing procedures was tested first. One specimen from each of the five variations was tested at a time so that others remained in case of errors found later in the testing procedure. A forementioned error was found within the testing method after testing one specimen from each variation. The crosshead speed of the Instron was initially set to three mm/min. The speed was then changed to one mm/min after discovering that the specimen variations containing mesoscale structures fractured too quickly to gather adequate data. The five specimens (A1, B1, C1, D1, and E1) that were tested at three mm/min could no longer be used for comparison.

The width and thickness of each test specimen, as well as the distance between the extensometer knife edges, were measured using a caliper. The measured values mentioned above, as well as the file names of the Microsoft Excel spreadsheet data, was recorded on a data collection sheet for each individual test specimen in the order that they are listed. Specimens were tested in this order as well. Table 2 displays the data collection sheet for all 25 specimens.

*Table 2: Specimen Tensile Testing Data Collection Sheet*

	<b>Width (mm)</b>	<b>Thickness (mm)</b>	<b>Length Between Edges (mm)</b>	<b>Spreadsheet Data File Name</b>
<b>A2</b>	6	6	27.3	A2_Specimen_RawData_Complete.xlsx
<b>B2</b>	6	6	27.3	B2_Specimen_RawData_Complete.xlsx
<b>C2</b>	6	6	27.3	C2_Specimen_RawData_Complete.xlsx
<b>D2</b>	6	6	27.3	D2_Specimen_RawData_Complete.xlsx
<b>E2</b>	6	6	27.3	E2_Specimen_RawData_Complete.xlsx
<b>A3</b>	6	6	27.3	A3_Specimen_RawData_Complete.xlsx
<b>B3</b>	6	6	27.3	B3_Specimen_RawData_Complete.xlsx
<b>C3</b>	6	6	27.3	C3_Specimen_RawData_Complete.xlsx
<b>D3</b>	6	6	27.3	D3_Specimen_RawData_Complete.xlsx
<b>E3</b>	6	6	27.3	E3_Specimen_RawData_Complete.xlsx
<b>A4</b>	6	6	27.3	A4_Specimen_RawData_Complete.xlsx
<b>B4</b>	6	6	27.3	B4_Specimen_RawData_Complete.xlsx
<b>C4</b>	6	6	27.3	C4_Specimen_RawData_Complete.xlsx
<b>D4</b>	6	6	27.3	D4_Specimen_RawData_Complete.xlsx
<b>E4</b>	6	6	27.3	E4_Specimen_RawData_Complete.xlsx
<b>A5</b>	6	6	27.3	A5_Specimen_RawData_Complete.xlsx
<b>B5</b>	6	6	27.3	B5_Specimen_RawData_Complete.xlsx
<b>D5</b>	6	6	27.3	D5_Specimen_RawData_Complete.xlsx
<b>E5</b>	6	6	27.3	E5_Specimen_RawData_Complete.xlsx

Load vs. displacement curves were generated for each specimen from the load and displacement data acquired from testing. Stress-strain curves were generated for each specimen as well. Yield strength, elongation at yield, elastic modulus, and fracture values were then determined from the stress-strain curves. Poisson's ratio for each specimen was calculated using axial and transverse strain data.

Two photos of each test specimen were taken during the tensile test. The first photo was taken before tensile testing and the second was taken after fracture. The photos for each specimen are shown, beginning with the solid specimens (A2-A5). Cubic specimen (E2-E5) photos are next, followed by re-entrant hexagonal x-axis-oriented (C2-C4), y-axis-oriented (D2-D5), and z-axis-oriented specimens (B2-B5), respectively. Each photo file name was carefully chosen to ensure the images did not get mixed up. Table 3 displays the file name for each photo in the ascending order that it was taken.

*Table 3: Specimen Tensile Testing Photo File Names*

	<b>File Name After Loading</b>	<b>File Name After Fracture</b>
<b>A1</b>	A1_AL	A1_Fracture
<b>B1</b>	B1_AL	B1_Fracture
<b>D1</b>	D1_AL	D1_Fracture
<b>E1</b>	E1_AL	E1_Fracture
<b>A2</b>	A2_AL	A2_Fracture
<b>B2</b>	B2_AL	B2_Fracture
<b>C2</b>	C2_AL	C2_Fracture
<b>D2</b>	D2_AL	D2_Fracture
<b>E2</b>	E2_AL	E2_Fracture
<b>A3</b>	A3_AL	A3_Fracture
<b>B3</b>	B3_AL	B3_Fracture
<b>C3</b>	C3_AL	C3_Fracture
<b>D3</b>	D3_AL	D3_Fracture
<b>E3</b>	E3_AL	E3_Fracture
<b>A4</b>	A4_AL	A4_Fracture
<b>B4</b>	B4_AL	B4_Fracture
<b>C4</b>	C4_AL	C4_Fracture
<b>D4</b>	D4_AL	D4_Fracture
<b>E4</b>	E4_AL	E4_Fracture
<b>A5</b>	A5_AL	A5_Fracture
<b>B5</b>	B5_AL	B5_Fracture
<b>D5</b>	D5_AL	D5_Fracture
<b>E5</b>	E5_AL	E5_Fracture

**3.7.1 Tensile testing photos.** Figure 33A displays a photo taken of the solid specimen A2 before tensile testing and Figure 33B display a photo taken after fracture on the Instron. Each of the sequential figures within this section are formatted the same. Each of the solid specimen variants (A2-A5) tended to fracture within the necked down region of the specimen. The solid specimens each had a ductile fracture as well, meaning that the fracture occurred as a result of a large amount of deformation.

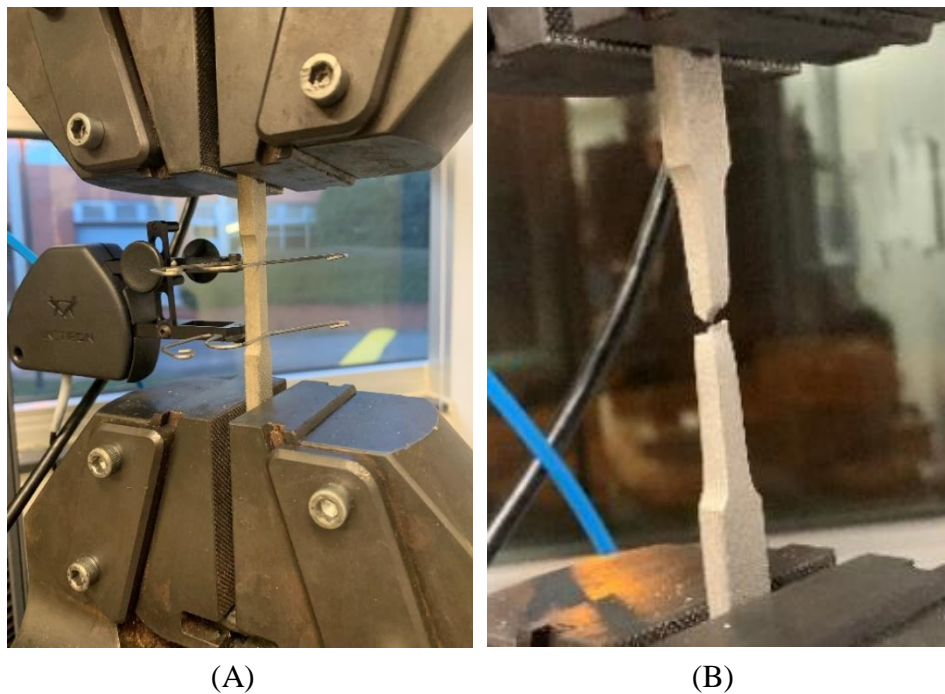


*Figure 33: A2 before (A) and after (B) Tensile Testing (photos taken by Terail Clonts)*

The fracture of specimen A3 (Figure 34) was within the same location of the necked down region as specimen A2. However, the appearance of the fracture was slightly different. The fracture of specimen A3 was in an opposite diagonal direction than that of specimen A2.

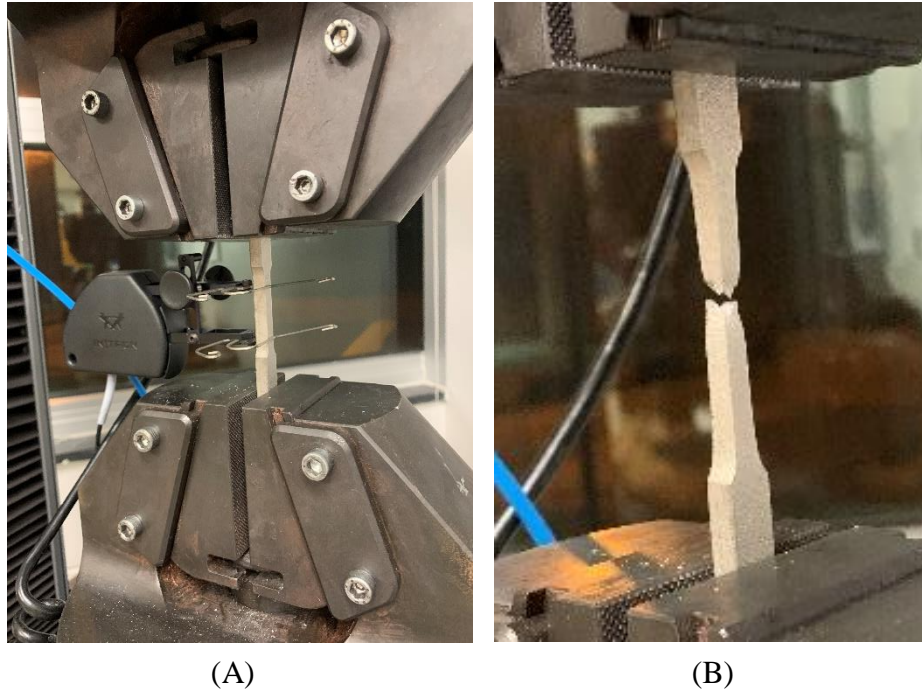


*Figure 34: A3 before (A) and after (B) Tensile Testing (photos taken by Terail Clonts)*

The solid specimen A4 (Figure 35) fractured at a location slightly above the previous two specimens. The appearance of the fracture was different than the previous solid specimens as well. The fracture was more perpendicular to the axis that the load was applied.

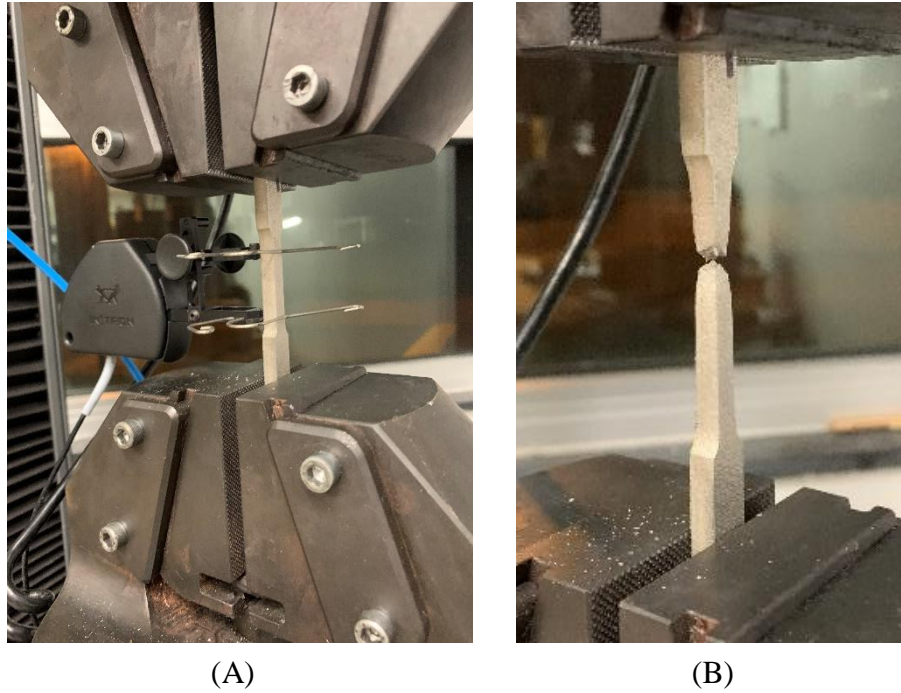


*Figure 35: A4 before (A) and after (B) Tensile Testing (photos taken by Terail Clonts)*

The solid specimen A5 (Figure 36) fractured within the same location of the necked down region as specimen A4. The appearance of the fracture was almost identical to the solid specimen A4 fracture. Both fractures were more perpendicular to the loading axis than any of the other solid specimens.

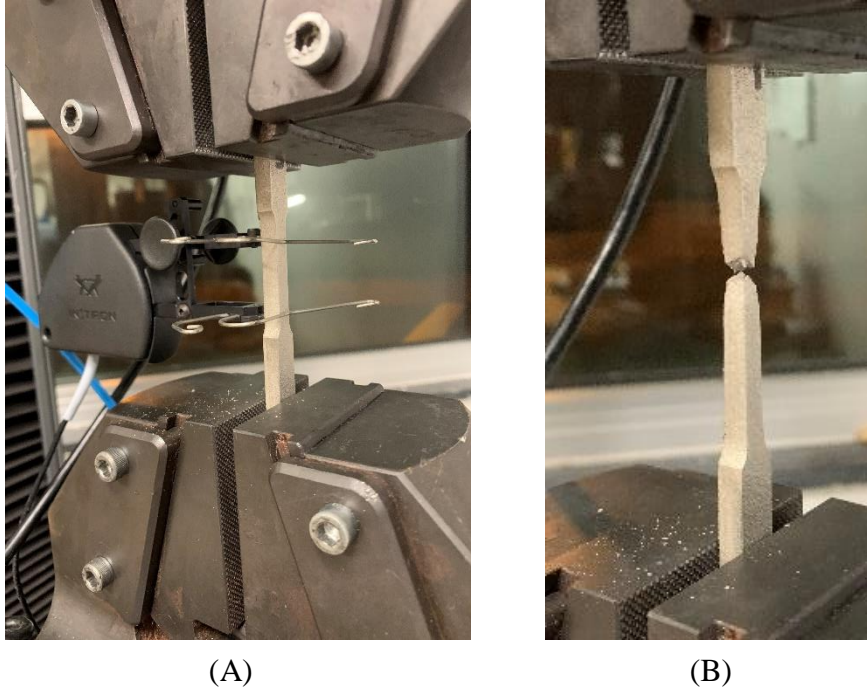


*Figure 36: A5 before (A) and after (B) Tensile Testing (photos taken by Terail Clonts)*

Figure 37 displays the photos taken of cubic specimen E2. Each of the cubic specimen (E2-E5) fractures appeared to be a brittle fracture, meaning that there was little deformation before the fracture occurred. The cubic specimen E2 fractured within the necked down section of the specimen. The direction of the fracture was not perpendicular to the axis that the load was applied, instead the fracture occurred in a diagonal direction.



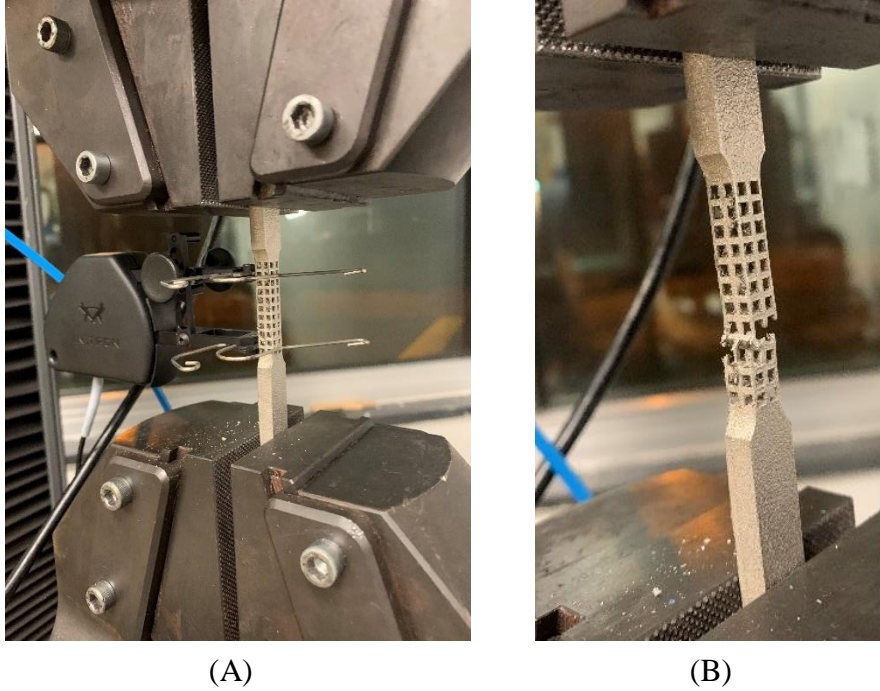


*Figure 37: E2 before (A) and after (B) Tensile Testing (photos taken by Terail Clonts)*

The cubic specimen E3 (Figure 38) fractured at the transition between the mesoscale structure and the solid top grip of the specimen. The specimen fractured at this location because the struts of the mesoscale structure connecting to the top grip were damaged from the printing process. The damage can be seen in Figure 38A above the top clip of the extensometer.



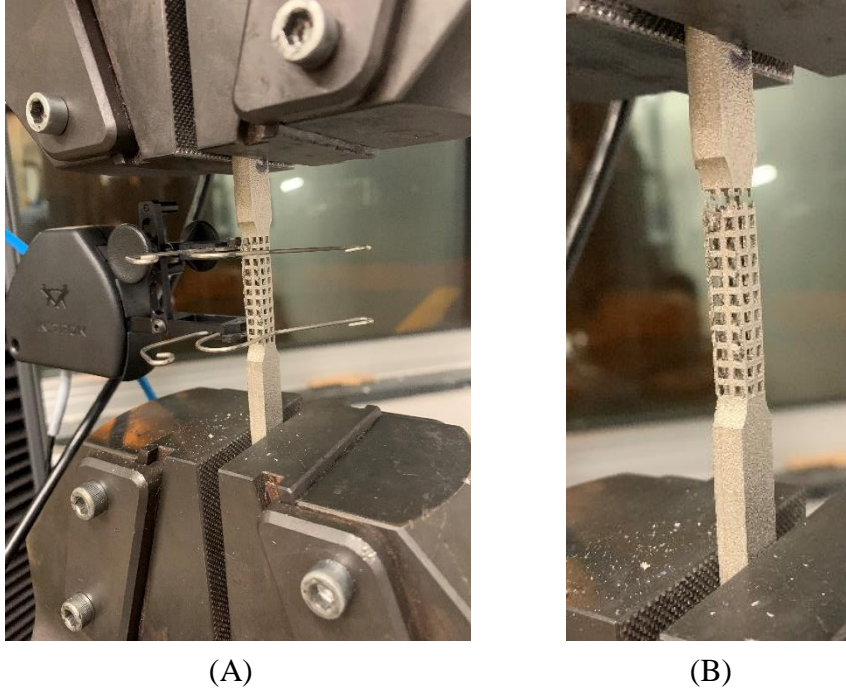


*Figure 38: E3 before (A) and after (B) Tensile Testing (photos taken by Terail Clonts)*

The cubic specimen E4 (Figure 39) fractured at the same location as specimen E3. The location of the fracture can be explained by the damaged struts as well. Many of the outer struts of the mesoscale structure of specimen E4 were damaged and is apparent when looking at Figure 33B.

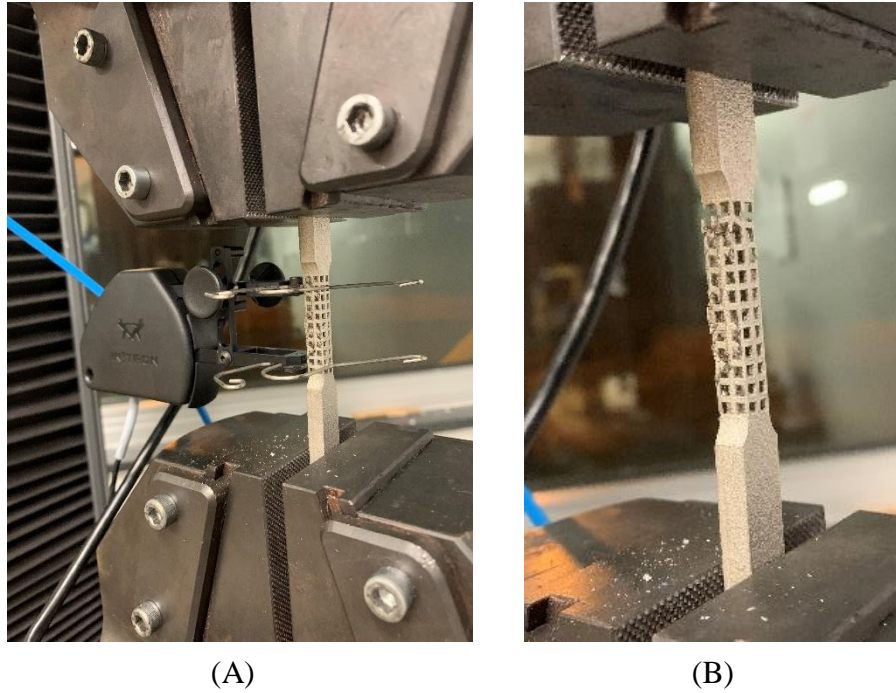


*Figure 39: E4 before (A) and after (B) Tensile Testing (photos taken by Terail Clonts)*

The cubic specimen E5 (Figure 40) fractured at the same location as the two previous specimens. Similar to specimen E3, many of the struts at the fracture location were damaged from the printing process. However, unlike specimen E4, the remaining struts within the structure were not damaged badly.

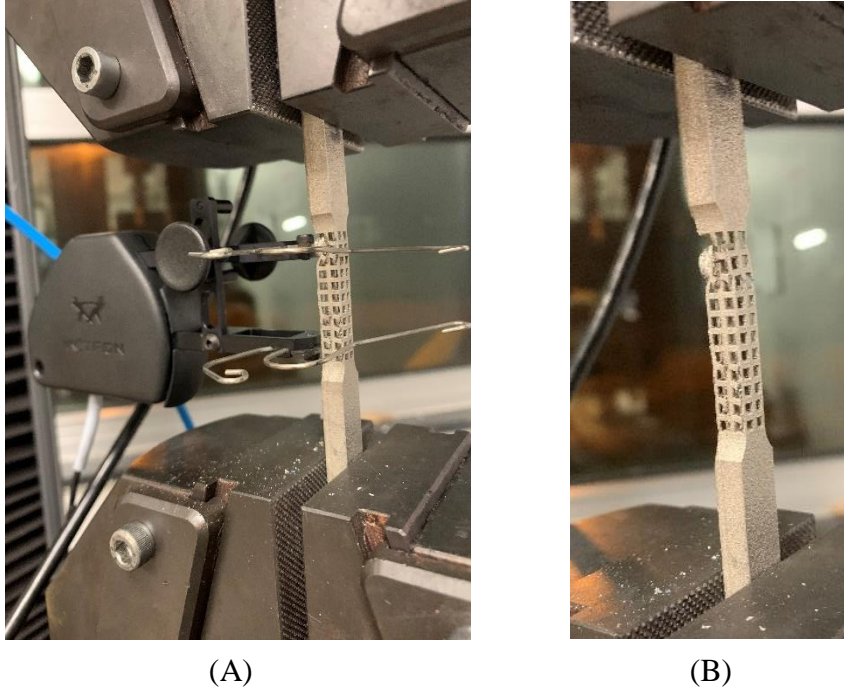
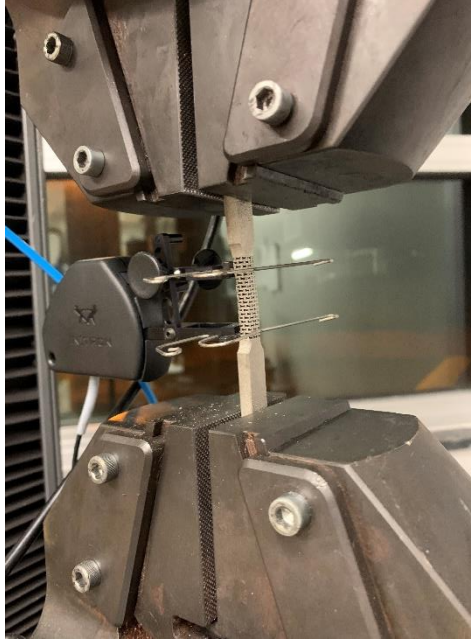


*Figure 40: E5 before (A) and after (B) Tensile Testing (photos taken by Terail Clonts)*

Figure 41 displays the photos taken of the re-entrant hexagonal x-axis-oriented specimen C2. Each of the specimens within the variant (C2-C4) appeared to have a brittle fracture like in the cubic specimen variant. Specimen C2 fractured at the transition between the mesoscale structures and the solid bottom grip of the specimen. The fracture was perpendicular to the axis that the load was applied and is not easily noticed in Figure 41B.



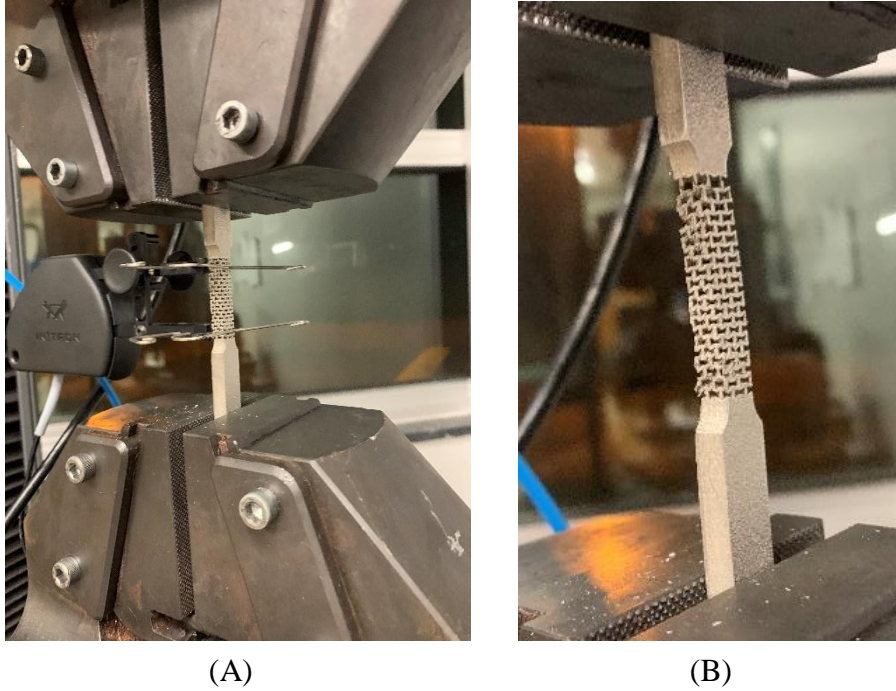
(A)



(B)

*Figure 41: C2 before (A) and after (B) Tensile Testing (photos taken by Terail Clonts)*

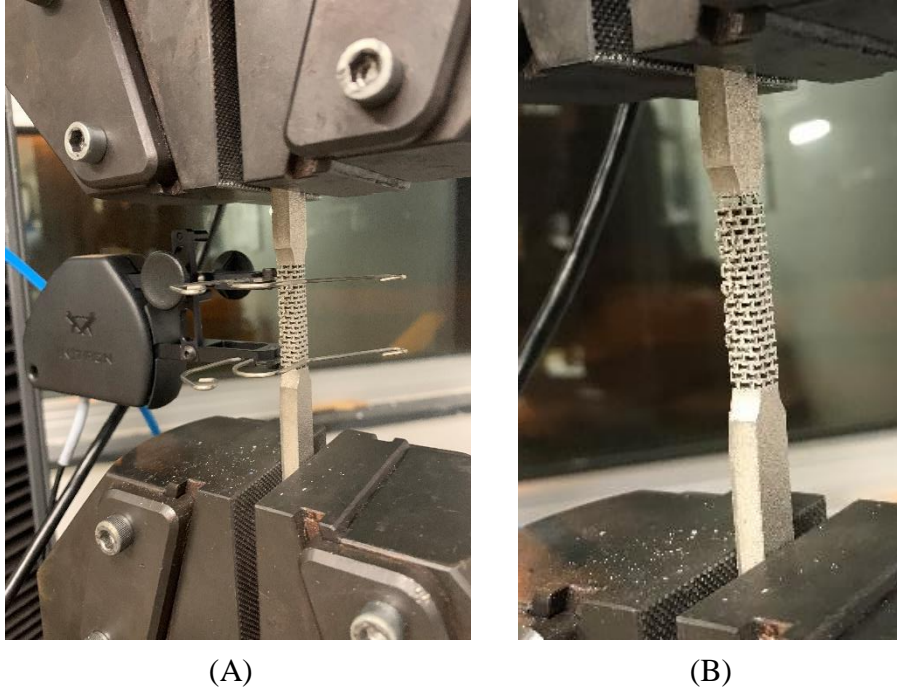
The re-entrant hexagonal x-axis-oriented specimen C3 (Figure 42) fractured at the transition between the mesoscale structures and the solid top grip of the specimen. The location of the fracture was due to the struts connecting to the top grip being damaged from the printing process. The struts at the bottom of the structure were damaged as well, although fracture did not occur at that location.



*Figure 42: C3 before (A) and after (B) Tensile Testing (photos taken by Terail Clonts)*

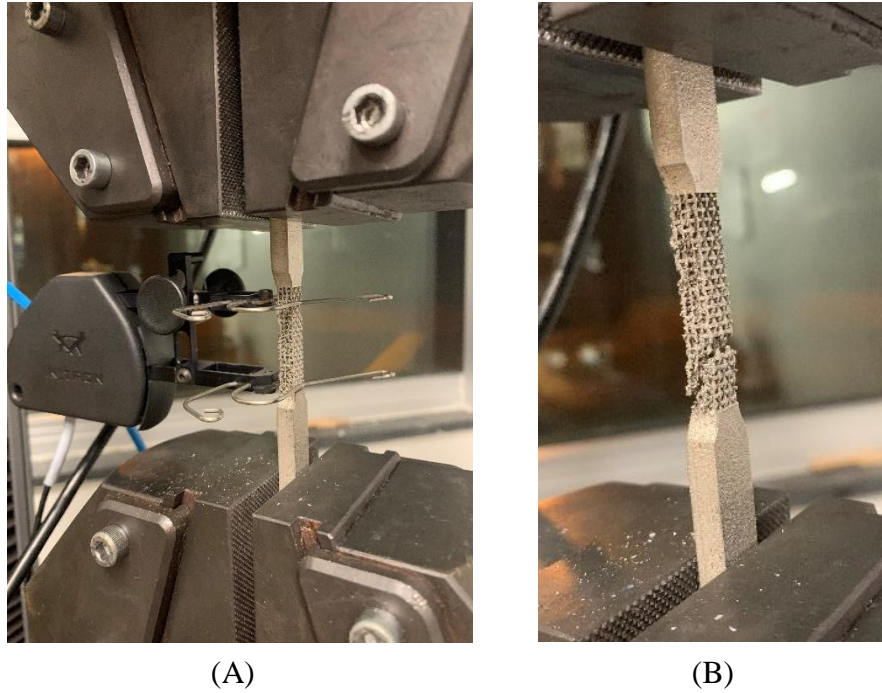
The re-entrant hexagonal x-axis-oriented specimen C4 (Figure 43) fractured at the same location as specimen C3. The location of the fracture was due to damaged struts, similar to specimen C3. However, many of the other struts within the structure were not damaged.





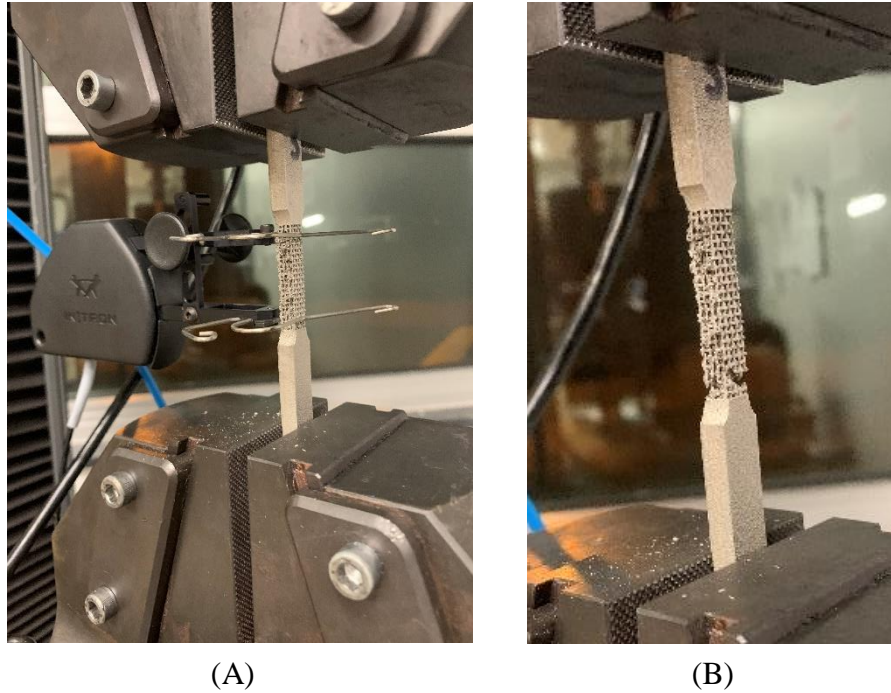
*Figure 43: C4 before (A) and after (B) Tensile Testing (photos taken by Terail Clonts)*

Figure 44 displays the photos taken of the re-entrant hexagonal y-axis-oriented specimen D2. Each of the specimens within this variant (D2-D5) appeared to have a brittle fracture like in the two previous mesoscale specimen variants. The re-entrant hexagonal y-axis-oriented specimen D2 fractured within the necked down section of the specimen containing the mesoscale structure. The fracture direction was diagonal in nature and began at the solid bottom grip of the specimen.



*Figure 44: D2 before (A) and after (B) Tensile Testing (photos taken by Terail Clonts)*

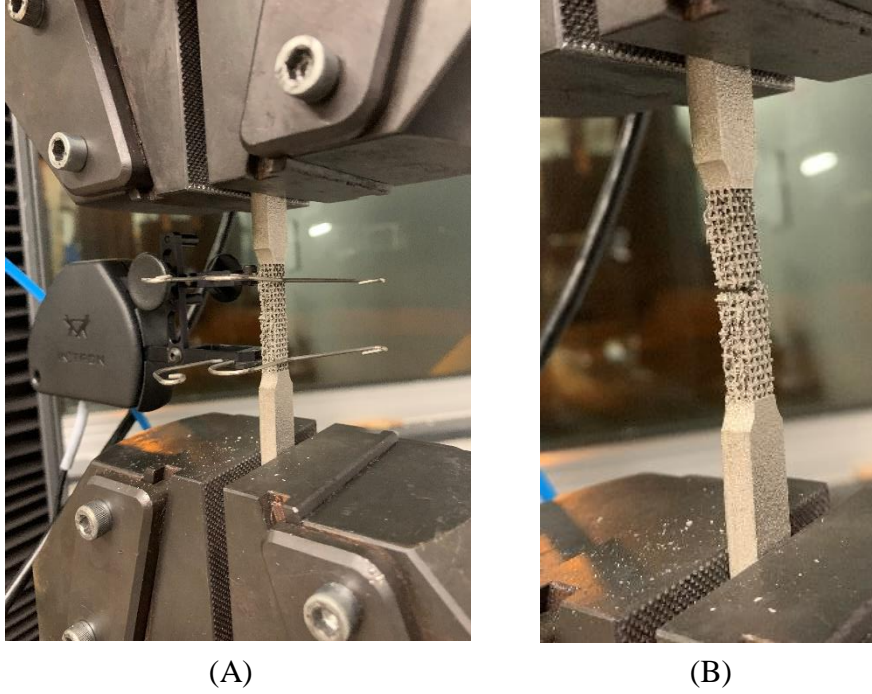
The re-entrant hexagonal y-axis-oriented specimen D3 (Figure 45) fractured slightly above the transition between the mesoscale structure and the solid bottom grip of the specimen. The struts of the mesoscale structure were damaged badly throughout. Excess support material existed on the structure as well because it was difficult to remove due to the orientation of the structure.



*Figure 45: D3 before (A) and after (B) Tensile Testing (photos taken by Terail Clonts)*

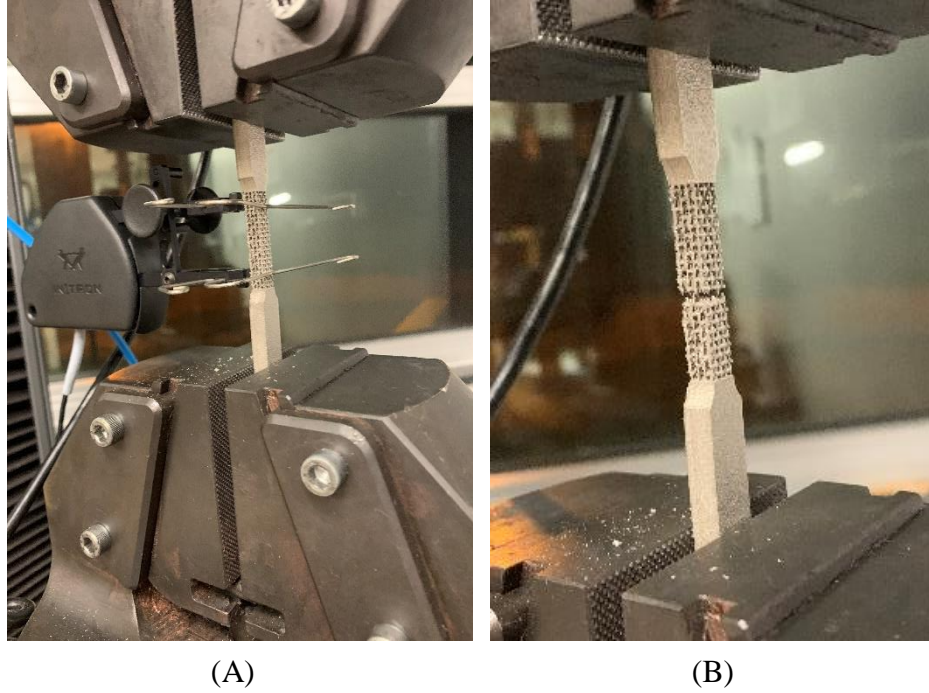
The re-entrant hexagonal y-axis-oriented specimen D4 (Figure 46) fractured within the necked down region of the specimen. The direction of the fracture was perpendicular to the axis that the load was applied. Specimen D4 did not contain as many damaged struts as the previous specimens within the variant.





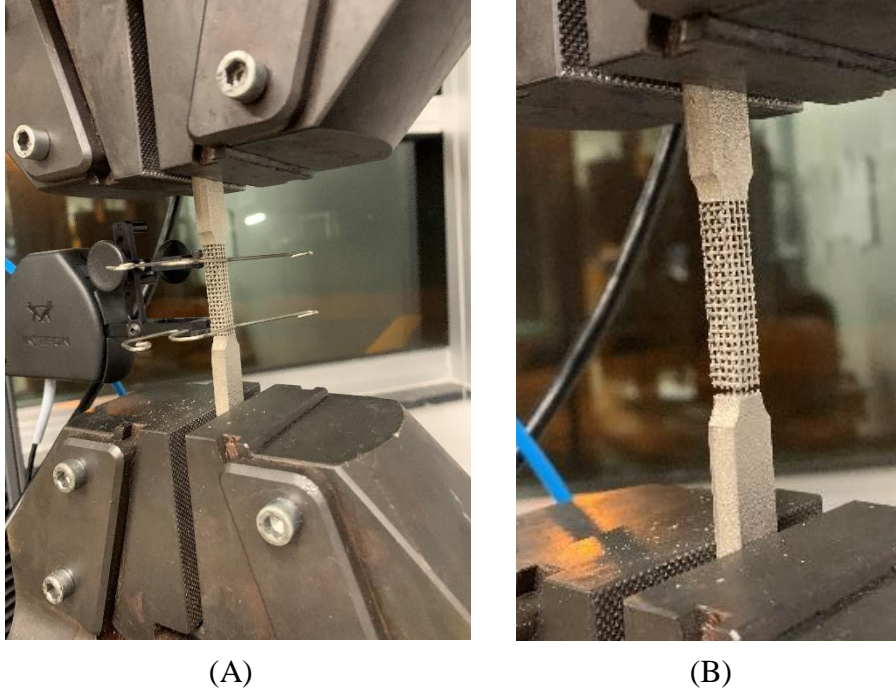
*Figure 46: D4 before (A) and after (B) Tensile Testing (photos taken by Terail Clonts)*

The re-entrant hexagonal y-axis-oriented specimen D5 (Figure 47) fractured within the necked down region of the specimen like in specimen D4. Fewer broken struts existed in this specimen as well. The direction of the fracture was perpendicular to the axis that the load was applied, but the location of the fracture was slightly lower than in specimen D4.



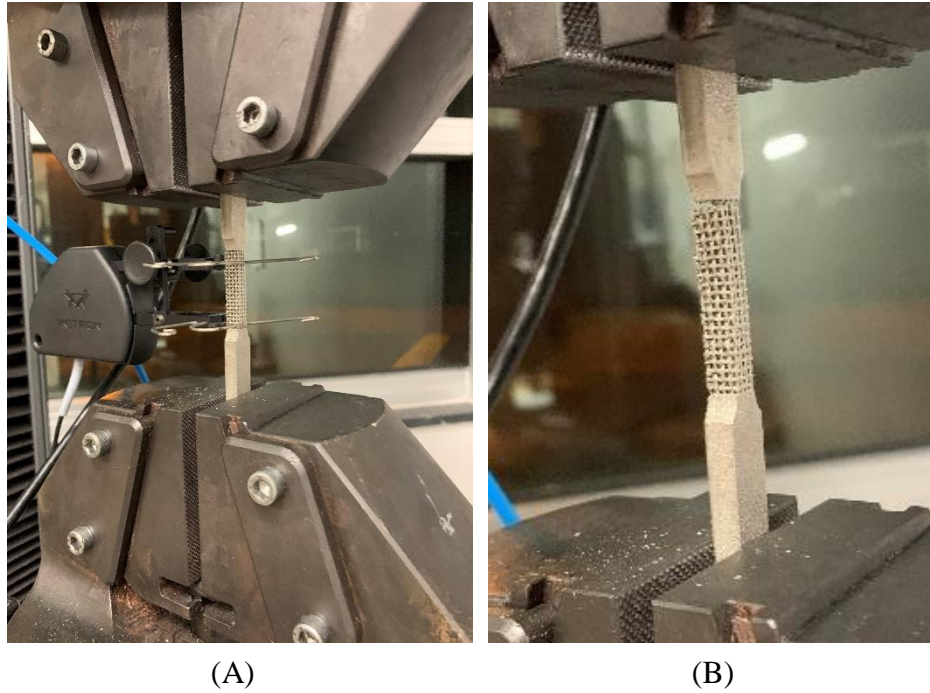
*Figure 47: D5 before (A) and after (B) Tensile Testing (photos taken by Terail Clonts)*

Figure 48 displays the photos taken of the re-entrant hexagonal z-axis-oriented specimen B2. Once again, each of the fractures within the variant (B2-B5) appeared to be brittle like in the other mesoscale variants. Specimen B2 fractured at the transition between the mesoscale structure and the solid bottom grip of the specimen. The direction of the fracture was perpendicular to the axis that the load was applied.



*Figure 48: B2 before (A) and after (B) Tensile Testing (photos taken by Terail Clonts)*

The re-entrant hexagonal z-axis-oriented specimen B3 (Figure 49) fractured at the transition between the mesoscale structure and the solid top grip of the specimen. The direction of the fracture was perpendicular to the axis that the load was applied, like in specimen B2. The structure appeared to have bent slightly at the top as a result of the fracture.



*Figure 49: B3 before (A) and after (B) Tensile Testing (photos taken by Terail Clonts)*

The re-entrant hexagonal z-axis-oriented specimen B4 (Figure 50) fractured at the same location as specimen B3. Both specimens B3 and B4 had similar amounts of damaged struts. The appearance of the fracture was almost identical to the fracture of specimen B3 as well, aside from appearing to not be as bent.

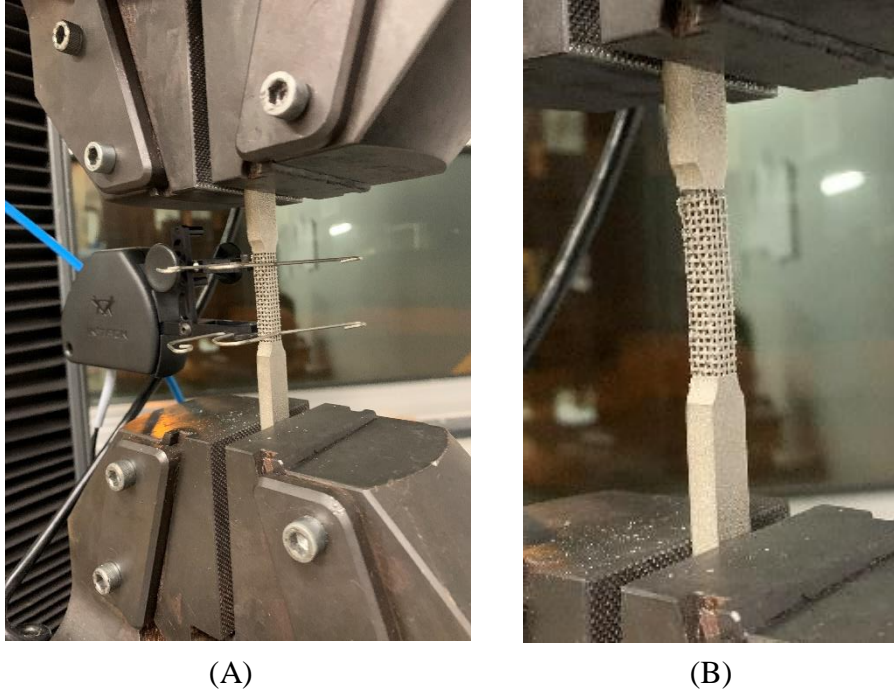
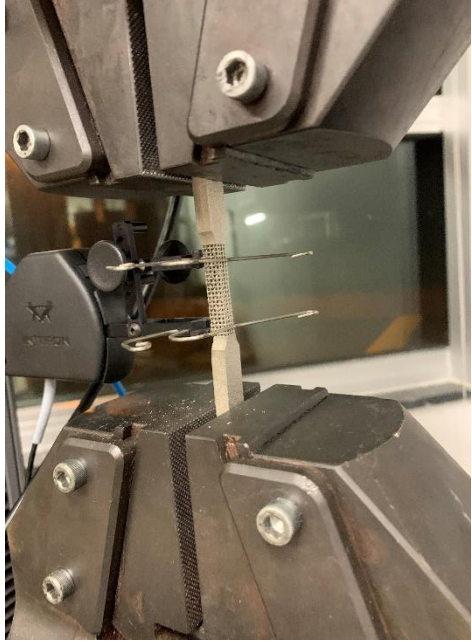


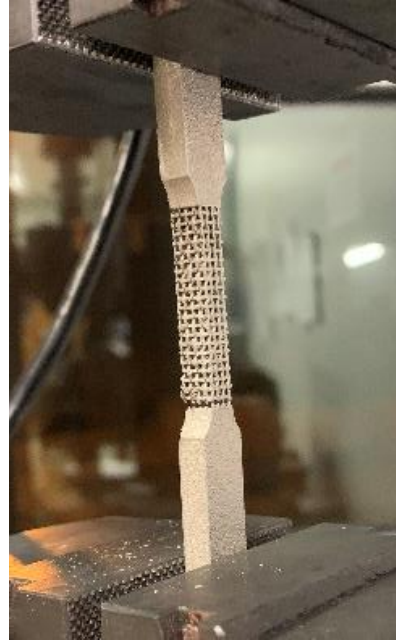
*Figure 50: B4 before (A) and after (B) Tensile Testing (photos taken by Terail Clonts)*

The re-entrant hexagonal z-axis-oriented specimen B5 (Figure 51) fractured at the same location as specimen B2. The fracture appeared almost identical to the fracture of specimen B2 as well. However, specimen B5 still had a single strut along the fracture that was intact.





(A)



(B)

*Figure 51: B5 before (A) and after (B) Tensile Testing (photos taken by Terail Clonts)*

### **3.8 Analysis of Experimental Data**

Microsoft Excel was used to perform a one-way ANOVA and post hoc two-tailed, independent samples t-tests on the specimen variants. A p-value of 0.05 was selected for the ANOVA and for each t-test. The ANOVA compared the material property means of all specimen variants, while the t-tests compared the mean of a particular specimen variant to the associated mean of each of the other variant. The material properties included apparent yield strength, elongation at yield, Poisson's ratio, apparent elastic modulus, and apparent fracture strength.

The ANOVA determined if there was a statistically significance in the difference in the overall material property, while the t-tests determined where the differences occurred by comparing each specimen mean individually. The t-test was used to compare the difference between the independent variable (specimen variant) and the dependent variable (particular mechanical property). Equal variances were assumed in these t-tests. The null hypothesis was that the mesoscale structure had no statistical significance on the particular measure material property, while the alternative hypothesis was that it did. A Bonferroni correction was used to adjust the alpha value in the t-tests so that the probability of observing at least one significant result due to chance remained below the desired significance level of 0.05. This was done by dividing the alpha value by the number of comparisons, therefore adjusting the alpha value to 0.01.

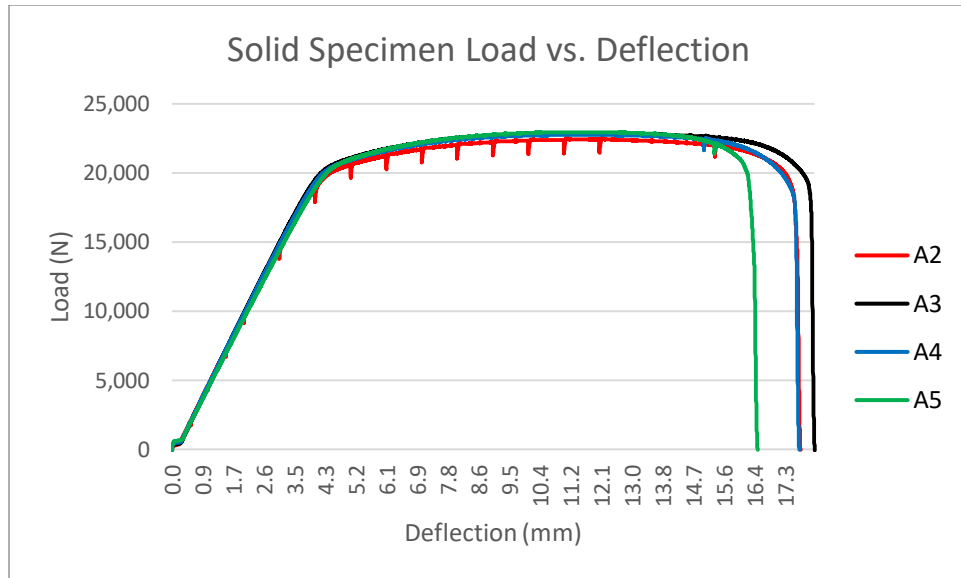
## CHAPTER FOUR: RESULTS

### 4.1 Uniaxial Tensile Test Results

Results from tensile tests performed on each specimen are displayed within this section. Instron tensile testing results include load vs. deflection curves and apparent stress vs. strain curves. The curves can be distinguished by color and each specimen variant is displayed on the same graph: the solid specimen (A2-A5), the cubic specimen (E2-E5), followed by re-entrant hexagonal x-axis-oriented (C2-C4), y-axis-oriented (D2-D5), and z-axis-oriented specimen (B2-B5) variants, respectively. A load vs. deflection curve and an apparent stress vs. strain curve has the same shape due to stress, which is the force applied to the specimen divided by the cross-sectional area, being a constant in the calculation.

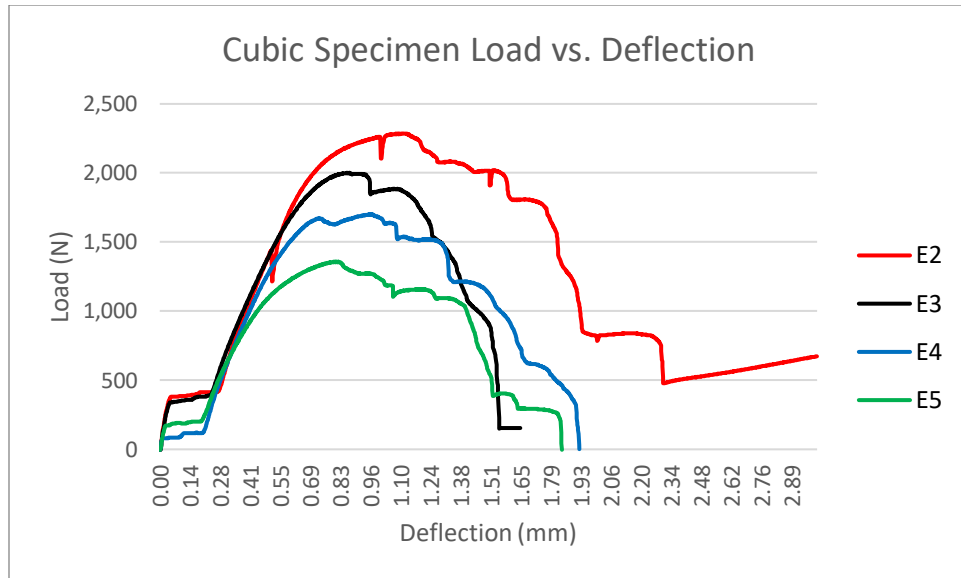
**4.1.1 Load vs. deflection curves.** Figure 52 displays the load vs. deflection curves for the solid specimen variant. Each of the solid specimens were able to withstand similar loads, aside from having varying deflections. Specimens A2 and A4 had curves that were almost identical in shape. The solid specimen variant deflected further and withstood greater loads than any of the mesoscale specimen variants because of its solid cross-section.





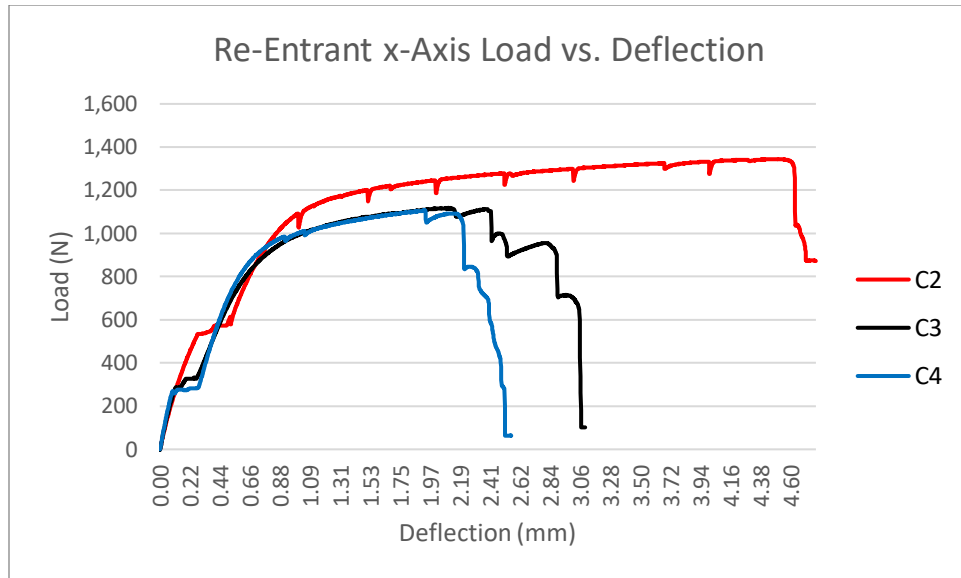
*Figure 52: Solid Specimen Load vs. Deflection*

Figure 53 displays the load vs. deflection curve for the cubic specimen variant. Each of the cubic specimen curves had similar slopes until a load of roughly 1000 N was reached. After that, each of the cubic specimen curves varied in load and deflection.



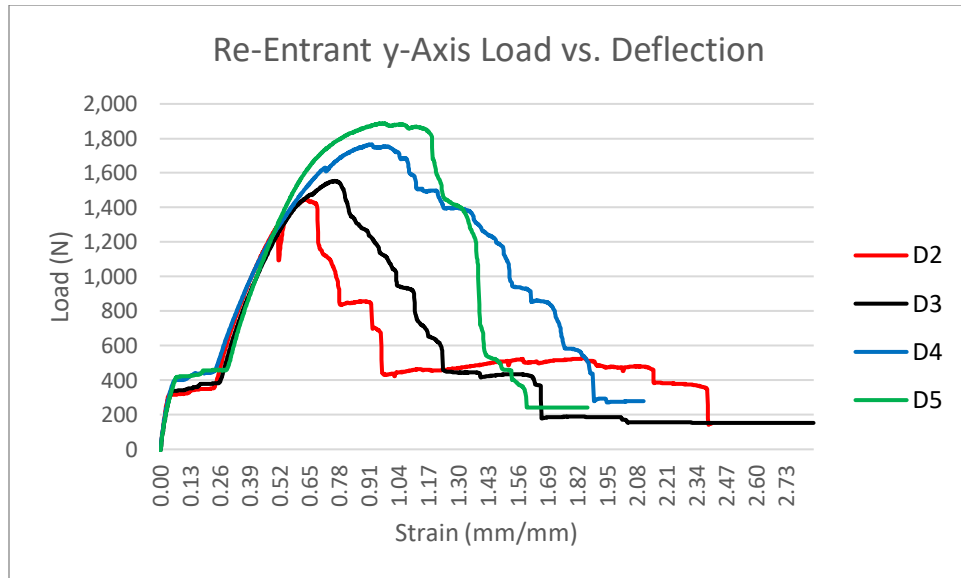
*Figure 53: Cubic Specimen Load vs. Deflection*

Figure 54 displays the load vs. deflection curve for the re-entrant x-axis-oriented specimen variant. Specimen C2 deflected further than the other two specimens that were tested. Specimens C3 and C4 had curves that were almost identical, aside from their deflection after a load of roughly 1,050 N.



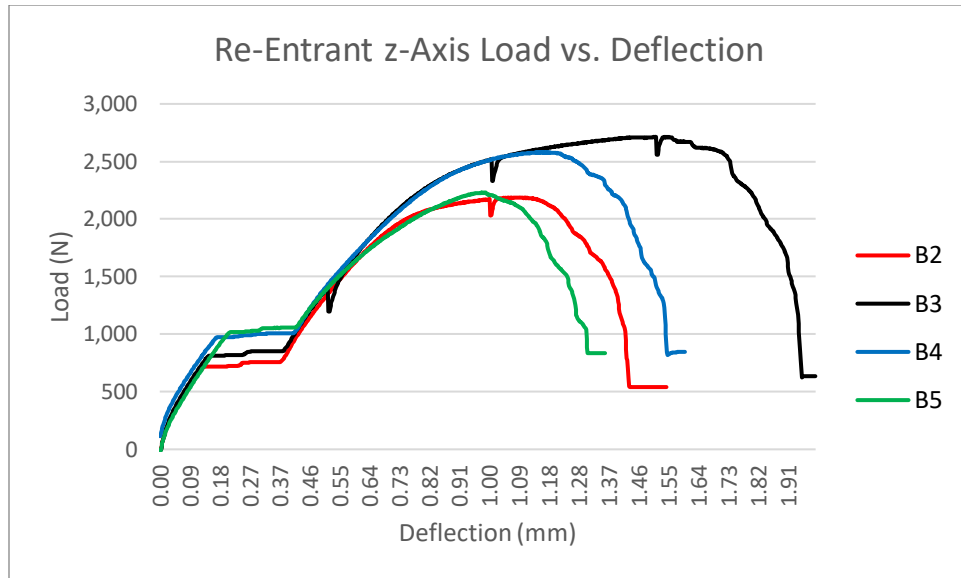
*Figure 54: Re-Entrant x-Axis Specimen Load vs. Deflection*

Figure 55 displays the load vs. deflection curve for the re-entrant y-axis-oriented specimen variant. Each of the specimen curves were almost identical until a load of 1,400 N was reached. After that, each of the curves had varying loads and deflections like in the cubic specimen variant.



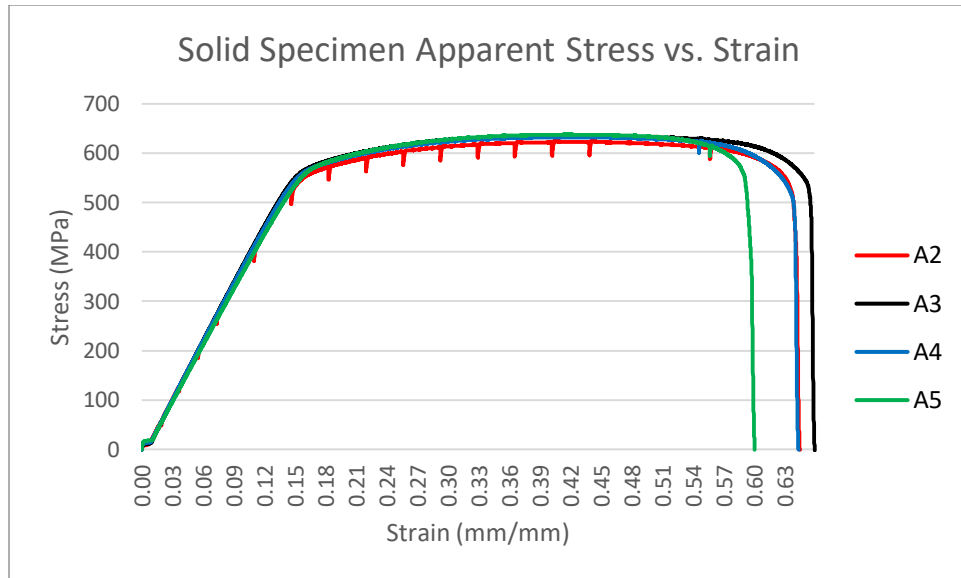
*Figure 55: Re-Entrant y-Axis Specimen Load vs. Deflection*

Figure 56 displays the load vs. deflection curve for the re-entrant z-axis-oriented specimen variant. Each of the curves were similar until a load of roughly 1,750 N. However, each of the curves had varying deflections after that like in the cubic and y-axis variants. Specimens B2 and B5 were able to withstand similar loads, similar to how specimens B3 and B4 were able to withstand similar loads.



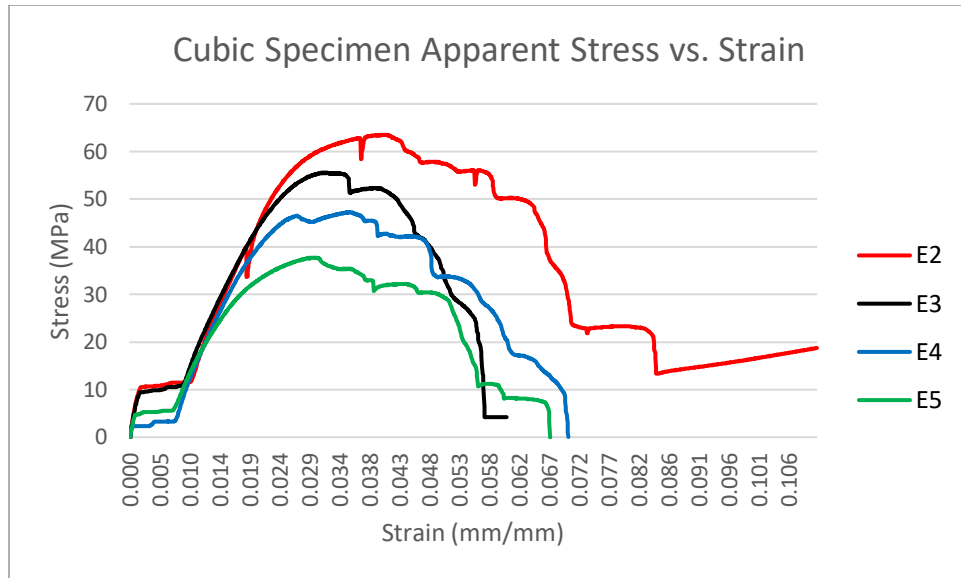
*Figure 56: Re-Entrant z-Axis Specimen Load vs. Deflection*

**4.1.2 Stress vs. strain curves.** Figure 57 displays the apparent stress vs. strain curves for the solid specimen variant (A2-A5). Each of the solid specimens had a similar curve, aside from having varying fracture strengths. Specimens A2 and A4 had curves that were almost identical in shape.



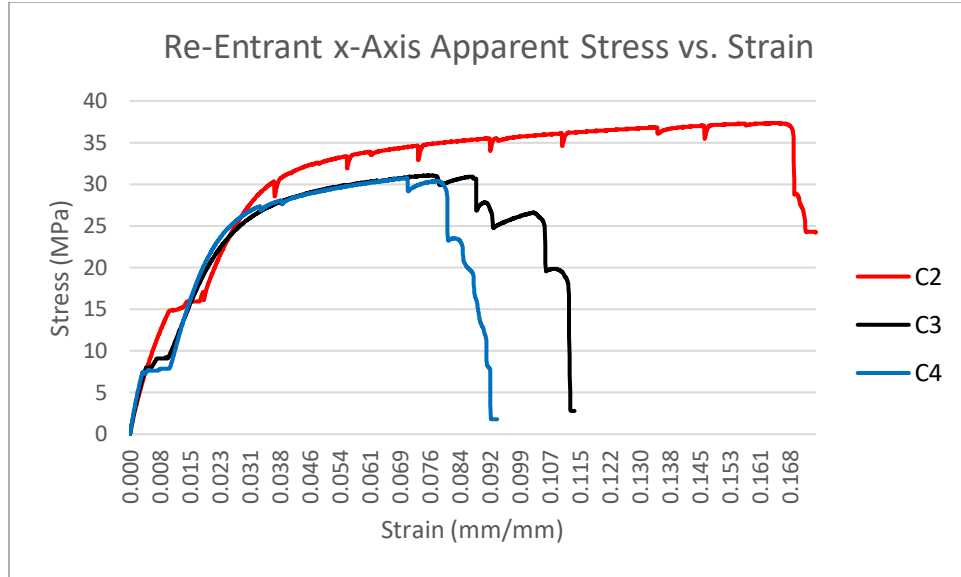
*Figure 57: Solid Specimen True Stress vs. Strain*

Figure 58 displays the apparent stress vs. strain curves for the cubic specimen variant (E2-E5). Each of the curves were similar within the elastic region. After that, the curves varied in yield and fracture strength. Each sequential specimen that was tested seemed to be able to withstand less amounts of stress. The quality of the specimens may be the reason for this being that specimen E5 was of lower quality and withstood the least amount of stress.



*Figure 58: Cubic Specimen Apparent Stress vs. Strain*

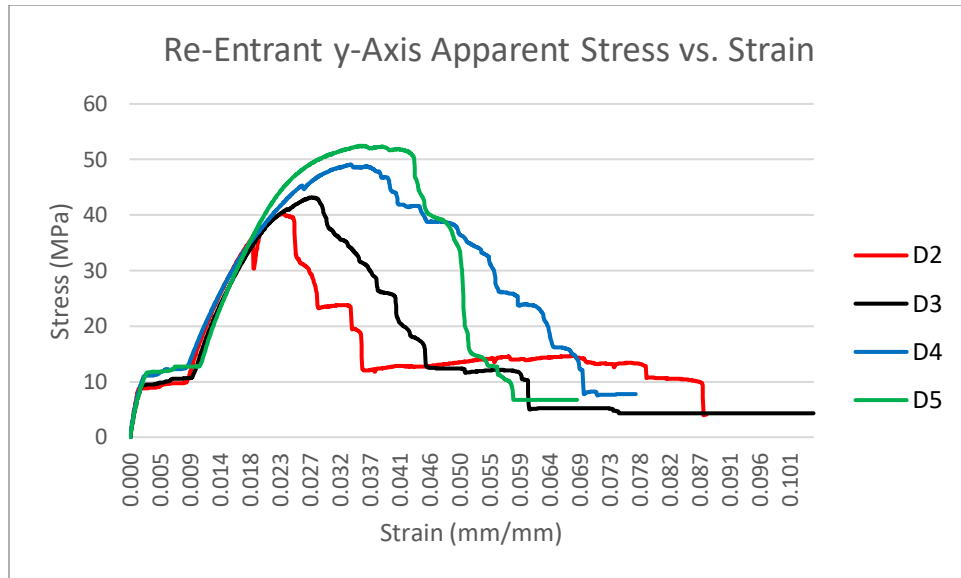
Figure 59 displays the apparent stress vs. strain curves for the re-entrant hexagonal x-axis-oriented specimen variant (C2-C4). Each of the curves were similar within the elastic region like in the cubic specimen variant. Specimen C4 strained further under similar amounts of stress than the remaining two specimens.



*Figure 59: Re-Entrant x-Axis Specimen Apparent Stress vs. Strain*

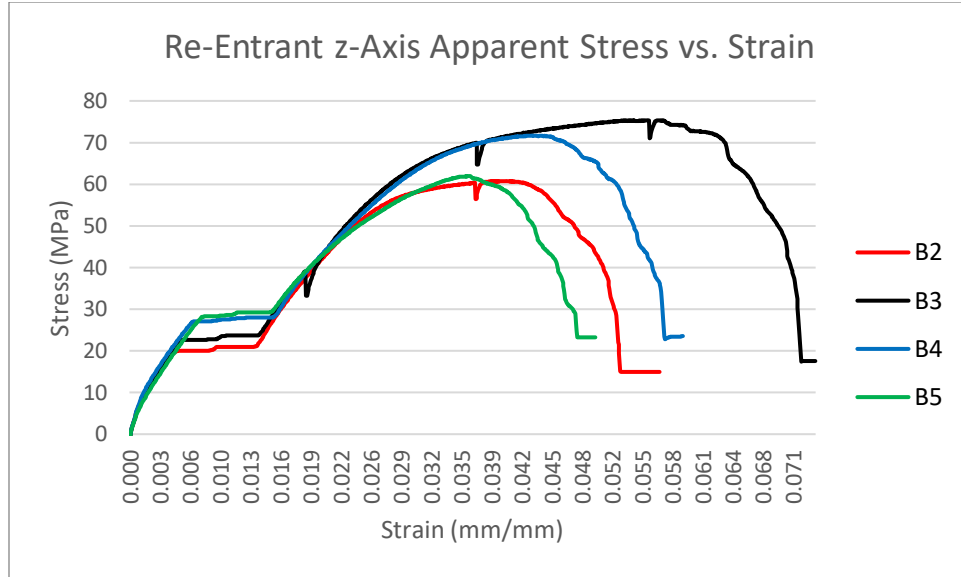
Figure 60 displays the apparent stress vs. strain curves for the re-entrant hexagonal y-axis-oriented specimen variant (D2-D5). Each of the curves were similar within the elastic region like in the cubic and x-axis specimen variants. After that, the curves varied in yield and fracture strength as well. The curves were not smooth because individual struts within the mesoscale structures tended to fracture before the entire structure fractured.





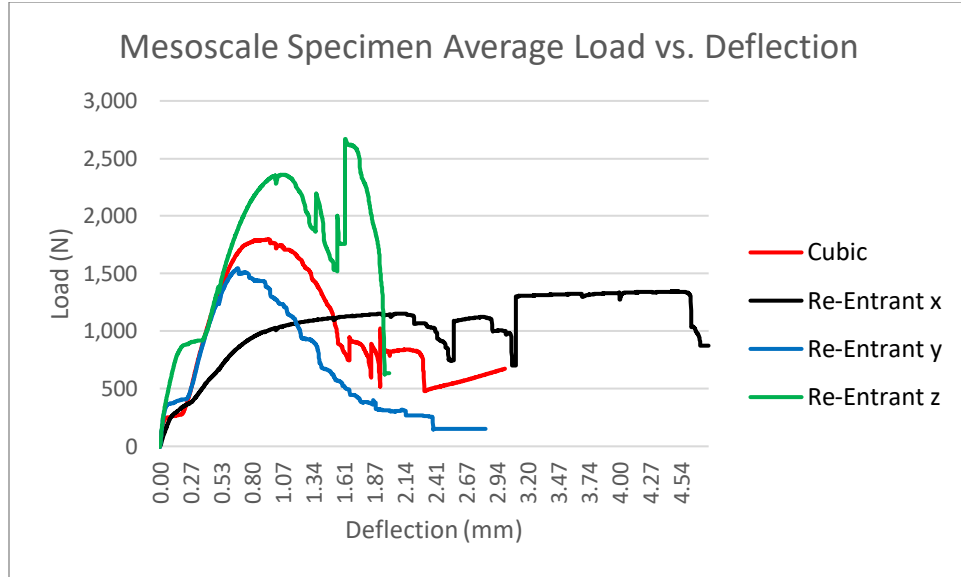
*Figure 60: Re-Entrant y-Axis Specimen Apparent Stress vs. Strain*

Figure 61 displays the apparent stress vs. strain curves for the re-entrant hexagonal z-axis-oriented specimen variant (B2-B5). Each of the curves were similar within the elastic region like before. Again, the curves all varied in yield and fracture strength as well. Specimen B3 was able to withstand the greatest amount of stress, while straining the furthest.



*Figure 61: Re-Entrant z-Axis Specimen Apparent Stress vs. Strain*

**4.1.3 Average curves.** An average load vs. deflection curve is displayed for each specimen variant containing mesoscale structures in Figure 62. An average load vs. deflection and true stress vs. strain curve for the solid specimen variant is not shown because all specimens within the variant had similar curves. Each of the mesoscale specimen variants had similar curves until a load of roughly 1,500 N, aside from the re-entrant hexagonal x-axis-oriented specimen variant (C2-C4). The re-entrant hexagonal x-axis-oriented specimen variant (C2-C4) was able to withstand the least loads but elongated the furthest. The re-entrant hexagonal z-axis-oriented specimen variant (B2-B5) was able to withstand the greatest loads but elongated the least. The cubic (E2-E5) and re-entrant hexagonal y-axis-oriented specimen (D2-D5) variants had curves that were the most similar to each other than any of the other mesoscale variants.



*Figure 62: Mesoscale Specimen Average Load vs. Deflection*

An average apparent stress vs strain curve is displayed for each specimen variant containing mesoscale structures in Figure 63. Each of the mesoscale specimen variants had similar curves within the elastic region, aside from the re-entrant hexagonal x-axis-oriented specimen variant (C2-C4). Each of the variants had varying yield and fracture strengths. The re-entrant hexagonal z-axis-oriented specimen variant (B2-B5) was able to withstand the most stress before fracture, while the x-axis variant (C2-C4) had the largest strain values.

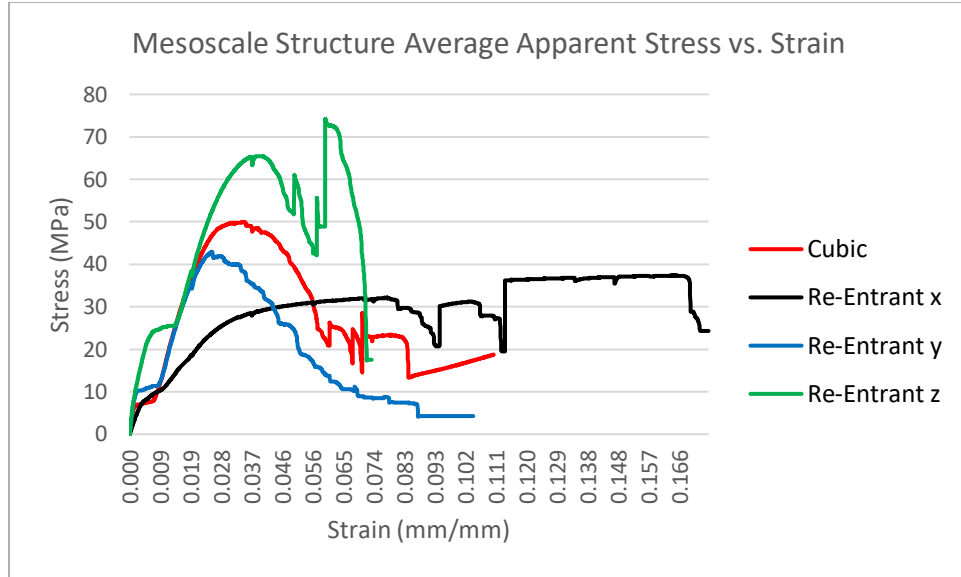


*Figure 63: Mesoscale Specimen Average Apparent Stress vs. Strain*

## 4.2 Material Property Results

Material properties of each specimen variant are displayed within this section. The properties were determined by analyzing the apparent stress vs. strain curves that were generated. The identified material properties include the apparent yield strength, elongation at yield, Poisson's ratio, apparent elastic modulus, and apparent fracture strength, along with average values of each. Bar graphs were generated that compare these average material property values for each specimen variant. Error bars in the graphs display the variation among specimens within each variant. The error bar values were determined by subtracting the minimum value from the average value and the average from the maximum.

**4.2.1 Apparent yield strength.** Table 4 displays the apparent yield strength of each specimen. The specimen variants containing mesoscale structures yielded under less amounts of stress than the solid specimen variant (A2-A5) because they did not have a solid cross-section. The re-entrant hexagonal x-axis-oriented specimen variant (C2-C4) had the lowest yield strength, roughly 20 times less than that of the solid specimen variant.

*Table 4: Apparent Yield Strength Results*

Variant	Specimen	Apparent Yield Strength (MPa)	Apparent Average (MPa)
Solid	A2	531	538
	A3	547	
	A4	542	
	A5	531	
Cubic	E2	58	48
	E3	52	
	E4	46	
	E5	33	
Re-Entrant x	C2	31	27
	C3	24	
	C4	26	
Re-Entrant y	D2	40	44
	D3	43	
	D4	45	
	D5	46	
Re-Entrant z	B2	56	62
	B3	63	
	B4	65	
	B5	62	

Figure 64 displays the average apparent yield strength comparison among each specimen variant. The solid specimen (A2-A5) had the highest average apparent yield strength, at roughly 538 MPa, being that it was not a porous structure. The cubic (E2-E5), the re-entrant hexagonal y-axis-oriented (D2-D5), and the re-entrant hexagonal z-axis-oriented specimens (B2-B5) had a lower modulus than the solid specimen, on average, between roughly 44 MPa and 62 MPa. The re-entrant hexagonal x-axis-oriented specimen (C2-C4) had the lowest average apparent yield strength of roughly 27 GPa. Error bars show that the apparent yield strength had little variation among specimens within each specimen variant.

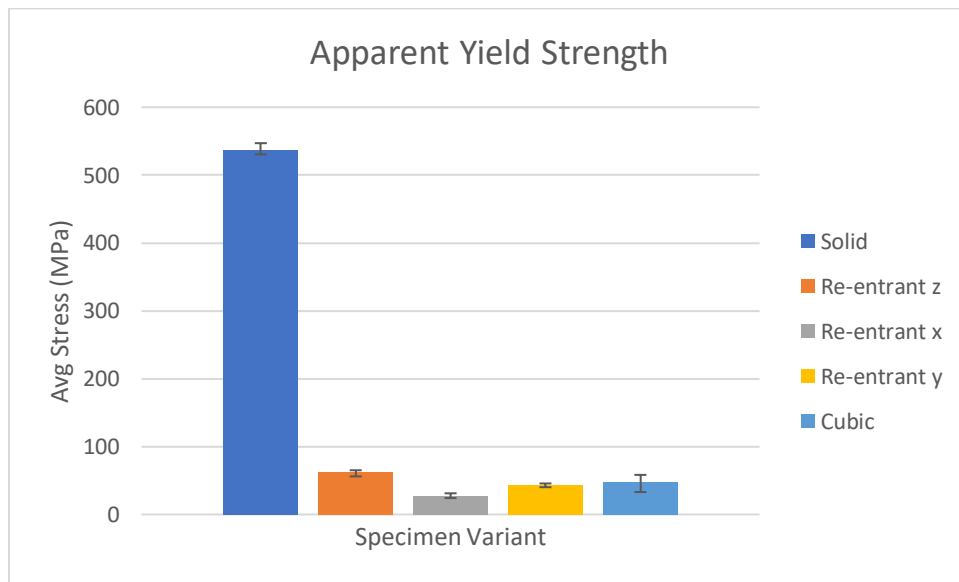


*Figure 64: Apparent Yield Strength Comparison*

**4.2.2 Elongation at yield.** Table 5 displays the elongation at yield of each specimen. The specimen variants containing mesoscale structures (excluding the solid specimen variant) elongated at yield equally on average. The solid specimen variant (A2-A5) elongated roughly five times as much as the other variants because it had a solid cross-section.

*Table 5: Elongation at Yield Results*

Variant	Specimen	Elongation at Yield (%)	Average (%)
Solid	A2	15.00	15.00
	A3	15.01	
	A4	15.00	
	A5	15.00	
Cubic	E2	2.81	2.54
	E3	2.60	
	E4	2.70	
	E5	2.07	
Re-entrant x	C2	4.00	3.12
	C3	2.64	
	C4	2.71	
Re-entrant y	D2	2.30	2.53
	D3	2.79	
	D4	2.62	
	D5	2.40	
Re-entrant z	B2	2.81	3.15
	B3	3.00	
	B4	3.20	
	B5	3.61	

Figure 65 displays the average elongation at yield comparison among each specimen variant. The solid specimens (A2-A5) elongated at yield the most on average, at 15 percent. The remaining specimen variants elongated much less on average, between 2.53 percent and 3.15 percent. The solid specimen exhibited ductile behavior since it elongated much further before fracture. Each of the mesoscale specimen variants exhibited brittle behavior being that they broke without significant deformation. Error bars show that the elongation at yield varied the most among each of the re-entrant hexagonal x-axis-oriented specimens (C2-C4) that were tested, at roughly 1.36 percent. The remaining specimen variants had little variation in elongation at yield.

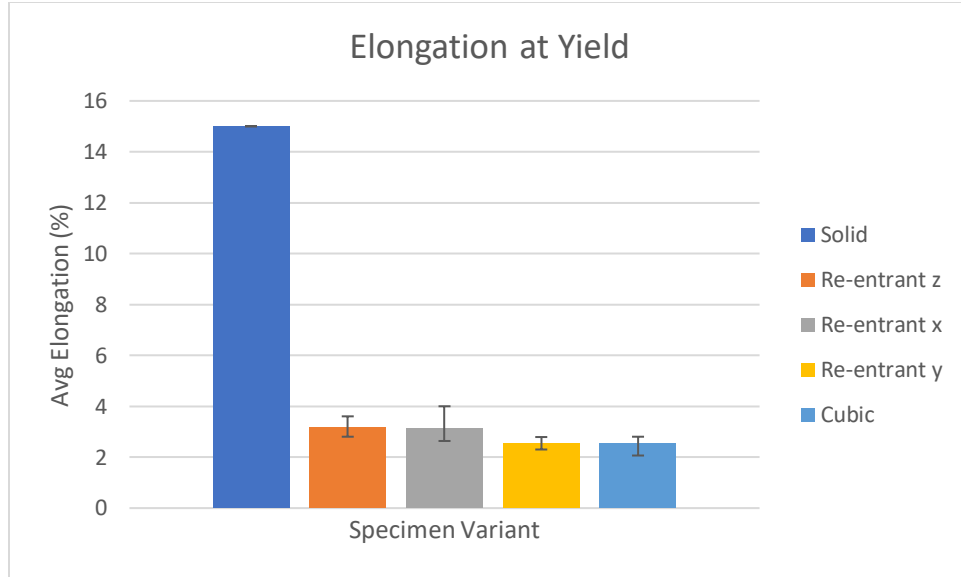


*Figure 65: Elongation at Yield Comparison*

**4.2.3 Poisson's ratio.** Table 6 displays the Poisson's ratio of each specimen. The average Poisson's ratio of the re-entrant hexagonal x-axis-oriented specimen variant (C2-C4) was roughly 3.6 to 7.3 times greater than the other variants. The ratio was negative because of the nature of the structure when oriented along its x-axis.



*Table 6: Poisson's Ratio Results*

Variant	Specimen	Poisson's Ratio	Average
Solid	A2	0.250	0.250
	A3	0.235	
	A4	0.268	
	A5	0.245	
Cubic	E2	0.310	0.284
	E3	0.236	
	E4	0.363	
	E5	0.226	
Re-entrant x	C2	-1.784	-1.84
	C3	-1.915	
	C4	-1.823	
Re-entrant y	D2	0.456	0.507
	D3	0.459	
	D4	0.592	
	D5	0.521	
Re-entrant z	B2	0.490	0.493
	B3	0.492	
	B4	0.485	
	B5	0.507	

Figure 66 displays the average Poisson's ratio comparison among each specimen variant. Error bars show that the Poisson's ratio varied little among each of the specimen variants that were tested. The solid (A2-A5) and cubic specimens (E2-E5) had similar average Poisson's ratios, at roughly 0.250 .and 0.284, respectively. The re-entrant hexagonal z-axis oriented (B2-B5) and y-axis-oriented specimens (D2-D5) had similar average ratios, as well, at roughly 0.507 and 0.493, respectively. Error bars show that the Poisson's ratio within each specimen variant varied little.

The re-entrant hexagonal x-axis-oriented specimen (C2-C4) had the highest average Poisson's ratio, at roughly 1.84. The ratio will always be positive for materials with a solid cross-section because the cross-section tends to become smaller when a tensile force is applied. The cross-section of the re-entrant hexagonal x-axis-oriented mesoscale structure became larger when a tensile force was applied, therefore making the ratio negative.

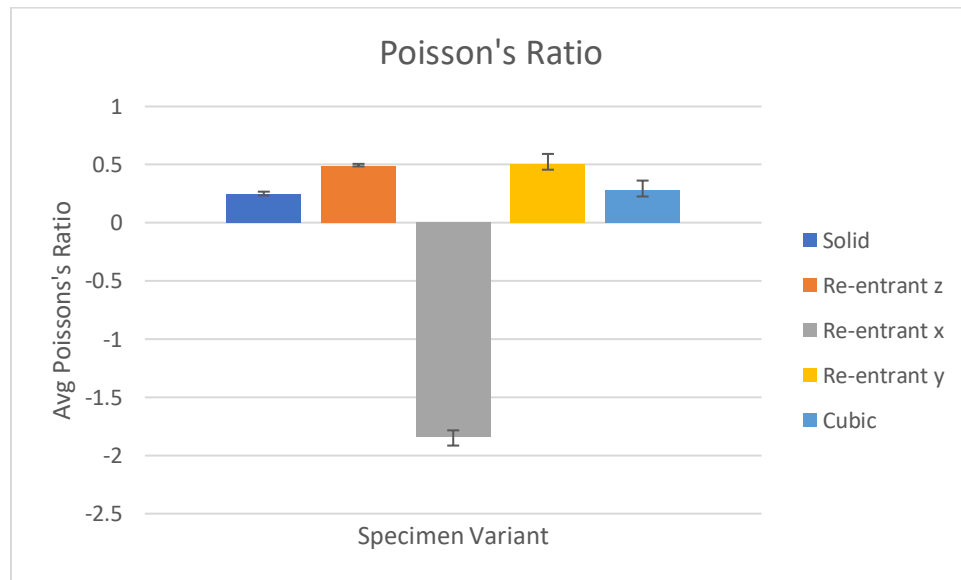


*Figure 66: Poisson's Ratio Comparison*

**4.2.4 Apparent elastic modulus.** Table 7 displays the apparent elastic modulus of each specimen. The specimen variants containing mesoscale structures had a 1.9 to 3.7 times lower modulus than the solid specimen variant (A2-A5) in the apparent stress calculation. The open areas within the cross-section were included in the calculation, therefore making the mesoscale specimen variants have a lower elastic modulus.

*Table 7: Apparent Elastic Modulus Results*

Variant	Specimen	Apparent Elastic Modulus (GPa)	Apparent Average (GPa)
Solid	A2	3.67	3.66
	A3	3.71	
	A4	3.70	
	A5	3.56	
Cubic	E2	2.03	1.86
	E3	2.04	
	E4	1.78	
	E5	1.61	
Re-Entrant x	C2	0.90	0.98
	C3	1.01	
	C4	1.02	
Re-Entrant y	D2	1.72	1.78
	D3	1.70	
	D4	1.87	
	D5	1.85	
Re-Entrant z	B2	1.86	1.90
	B3	1.92	
	B4	1.87	
	B5	1.94	

Figure 67 displays the average apparent elastic modulus comparison of each specimen variant. The solid specimen (A2-A5) had the highest average apparent elastic modulus, at roughly 3.66 GPa. The true and apparent elastic modulus of the solid specimen variant were equivalent because it was not a porous structure. The cubic (E2-E5), the re-entrant hexagonal y-axis-oriented (D2-D5), and the re-entrant hexagonal z-axis-oriented specimens (B2-B5) had roughly half the modulus as the solid specimen, on average, between roughly 1.78 GPa and 1.90 GPa. The re-entrant hexagonal x-axis-oriented specimen (C2-C4) had a lower modulus than the other specimen variants on average, at 0.98 GPa. Error bars show that the apparent modulus varied the most among each of the cubic specimens (E2-E5) that were tested, at roughly 0.4 GPa. Each of the remaining specimen variants had little variation.

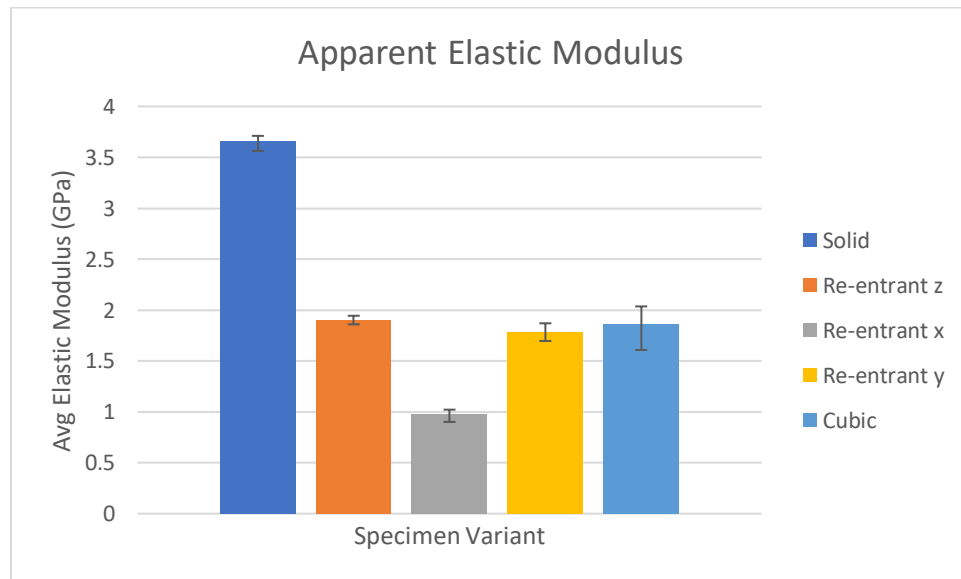


*Figure 67: Apparent Elastic Modulus Comparison*

**4.2.5 Apparent fracture strength.** Table 8 displays the apparent fracture strength of each specimen. The specimen variants containing mesoscale structures fractured before the solid specimen variant (A2-A5) in the apparent fracture calculation. Again, the lower fracture strength values are due to less volume of material within the cross-section of the specimen.

*Table 8: Apparent Fracture Results*

Variant	Specimen	Apparent Fracture (MPa)	Apparent Average (MPa)
Solid	A2	540	541
	A3	540	
	A4	523	
	A5	561	
Cubic	E2	49	43
	E3	44	
	E4	42	
	E5	35	
Re-Entrant x	C2	37	32
	C3	31	
	C4	29	
Re-Entrant y	D2	39	43
	D3	40	
	D4	42	
	D5	50	
Re-Entrant z	B2	42	51
	B3	48	
	B4	60	
	B5	51	

Figure 68 displays the average apparent fracture strength comparison among each specimen variant. The solid specimens (A2-A5) had the highest apparent average fracture strength, at 541 megapascals (MPa). The remaining specimen variants fractured between roughly 32 MPa and 51 MPa on average. Error bars show that the apparent fracture strength varied little among each of the specimen variants.

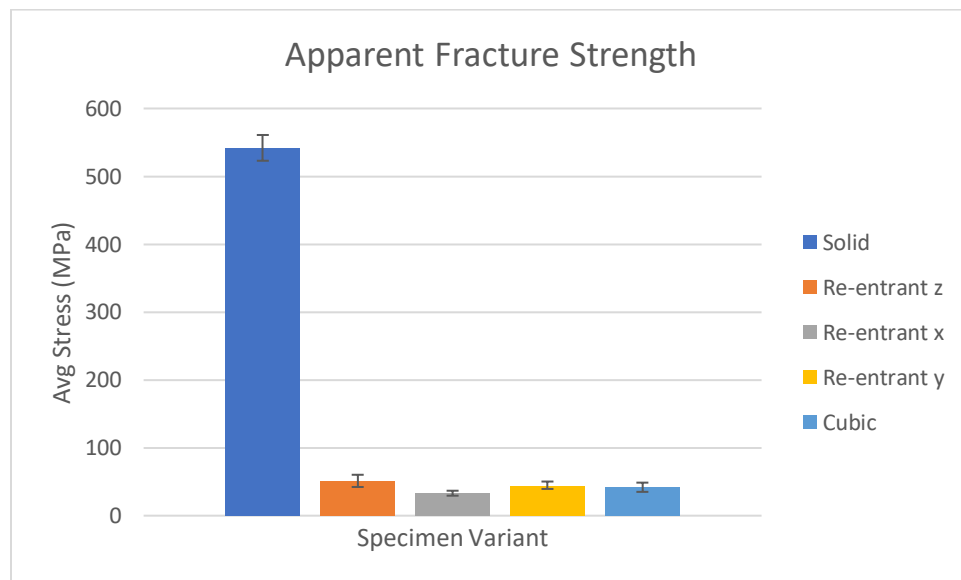


*Figure 68: Apparent Fracture Strength Comparison*

### **4.3 Apparent Elastic Modulus to Volume Ratio**

The apparent elastic modulus to volume ratio in the necked down region of the solid specimen variant was 1 GPa /315 mm<sup>3</sup>. The ratio was 1 GPa/307 mm<sup>3</sup> for the cubic specimen variant. The ratio ranged from 1 GPa/158 mm<sup>3</sup> to 1 GPa/169 mm<sup>3</sup> for the re-entrant hexagonal specimen variant oriented along each of its axes. The solid and cubic specimen variants had similar ratios although the solid variant had 3.8 times the volume of material within the necked down region of the specimen. The re-entrant hexagonal specimen variants had the same volume of material as the cubic specimen but had roughly half the modulus to volume ratio as the solid and cubic specimen variants.

### **4.4 Statistical Analysis Results**

Statistical analysis results are included within this section. Table 9 displays an example of an apparent yield strength ANOVA conducted between the specimen variants. The F-statistic was much greater than the F-critical value, meaning that something was statistical significance between the means. The p-value was also much lower than the alpha value of 0.05, which means that the null hypothesis should be rejected. The mesoscale structures were the reason for the difference in apparent yield strength means.

Table 9: Apparent Yield Strength ANOVA

Groups	Count	Sum	Average	Variance		
Solid	4	2150.766861	537.6917152	66.83472613		
Cubic	4	190.0855478	47.52138694	117.0806347		
Re-entrant x	3	80.86370567	26.95456856	13.78800102		
Re-entrant y	4	174.2301677	43.55754192	6.274092944		
Re-entrant z	4	246.5526193	61.63815481	15.54736468		
ANOVA						
Source of Variation	SS	df	MS	F	P-value	F crit
Between Groups	765195.7522	4	191298.938	4153.600159	2.39725E-21	3.112249848
Within Groups	644.7864576	14	46.05617554			
Total	765840.5386	18				

Table 10 displays an example of an apparent yield strength t-test conducted between the solid specimen variant (A2-A5) and the cubic specimen variant (E2-E5). The p-value was much less than the adjusted alpha value of 0.01. Therefore, the null hypothesis was rejected that the mesoscale structure was the reason for the difference in apparent yield strength means.

Table 10: Solid vs. Cubic Apparent Yield Strength t-Test

	Solid	Cubic
Mean	537.6917152	47.52138694
Variance	66.83472613	117.0806347
Observations	4	4
Pooled Variance	91.95768044	
Hypothesized Mean Difference	0	
df	6	
t Stat	72.2883001	
P(T<=t) one-tail	2.35807E-10	
t Critical one-tail	1.943180281	
P(T<=t) two-tail	4.71615E-10	
t Critical two-tail	2.446911851	

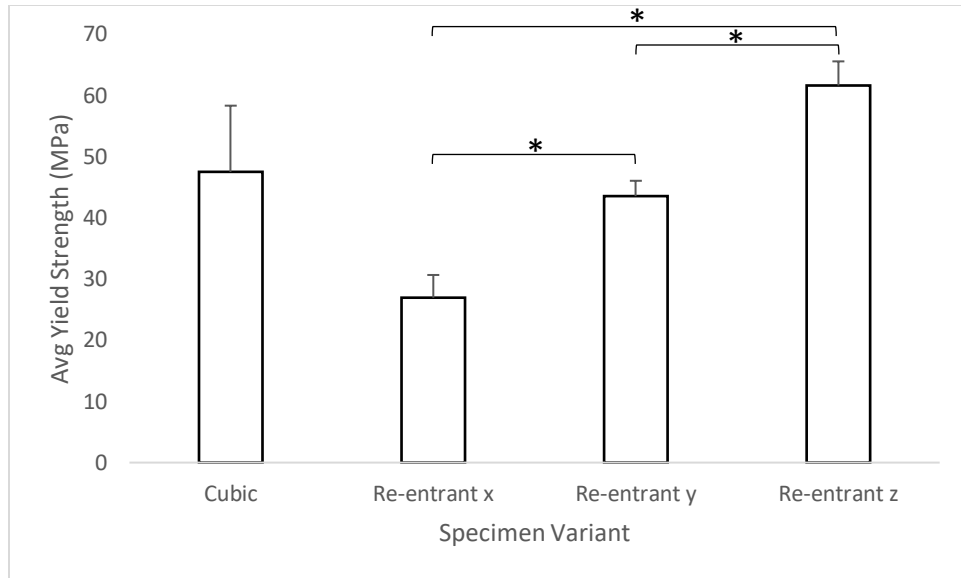


A summary of the remaining material property p-values for each specimen variant comparison are displayed below in Table 11. The asterisks denote if the comparison was significant. The difference in material property means were statistically significant in all solid specimen variant comparisons except when comparing Poisson's ratio means to the cubic specimen. Elongation at yield and apparent fracture strength were not statistically significance in any of the mesoscale specimen variant comparisons.

*Table 11: Summary of P-Values*

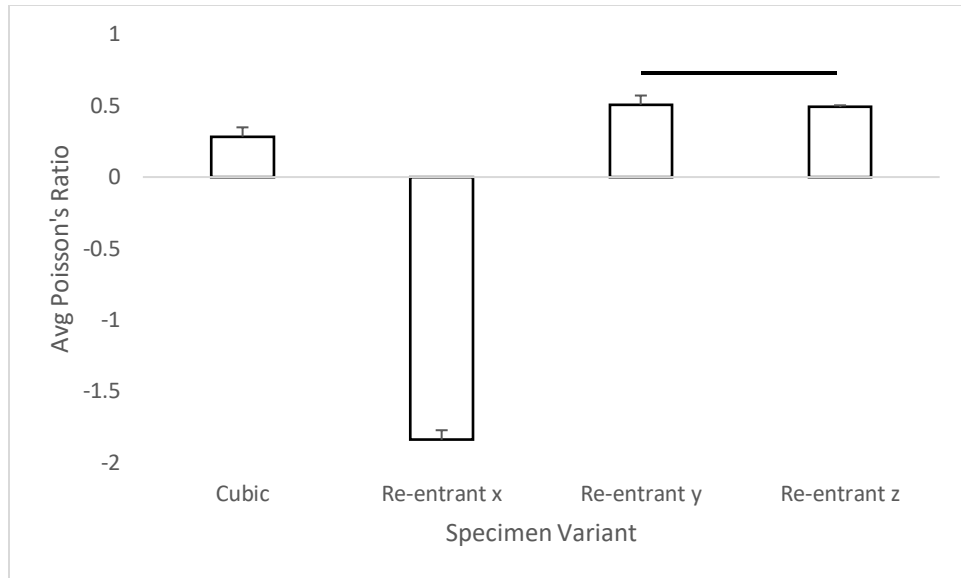
P-Values					
	Yield Strength	Elongation at Yield	Poisson's Ratio	Elastic Modulus	Fracture Strength
Solid vs. Cubic	4.7E-10*	3.5E-10*	0.344	3.4E-06*	1.4E-09*
Solid vs. Re-entrant x	2.0E-09*	5.6E-07*	2.0E-08*	4.7E-08*	4.0E-08*
Solid vs. Re-entrant y	2.8E-11*	3.1E-11*	2.2E-04*	4.4E-08*	1.3E-09*
Solid vs. Re-entrant z	5.1E-11*	6.1E-10*	1.1E-07*	8.2E-09*	2.0E-09*
Cubic vs. Re-entrant x	0.027	0.231	1.4E-07*	9.4E-04*	0.045
Cubic vs. Re-entrant y	0.502	0.943	2.7E-03*	0.501	0.938
Cubic vs. Re-entrant z	0.050	0.042	6.8E-04*	0.768	0.141
Re-entrant x vs. Re-entrant y	8.4E-04*	0.196	8.2E-08*	4.3E-05*	0.032
Re-entrant x vs. Re-entrant z	7.7E-05*	0.931	1.1E-08*	2.6E-06*	0.013
Re-entrant y vs. Re-entrant z	2.4E-04*	0.022	0.683	0.055	0.142

Figure 69 displays a summary of the post hoc apparent yield strength t-tests. A bracket spanning two adjacent bars indicates which specimen variants were statistically significant. Error bars display the standard deviation of the associated mean. A statistically significant difference in apparent yield strength means existed between the re-entrant hexagonal specimen variant oriented along each of its axes.



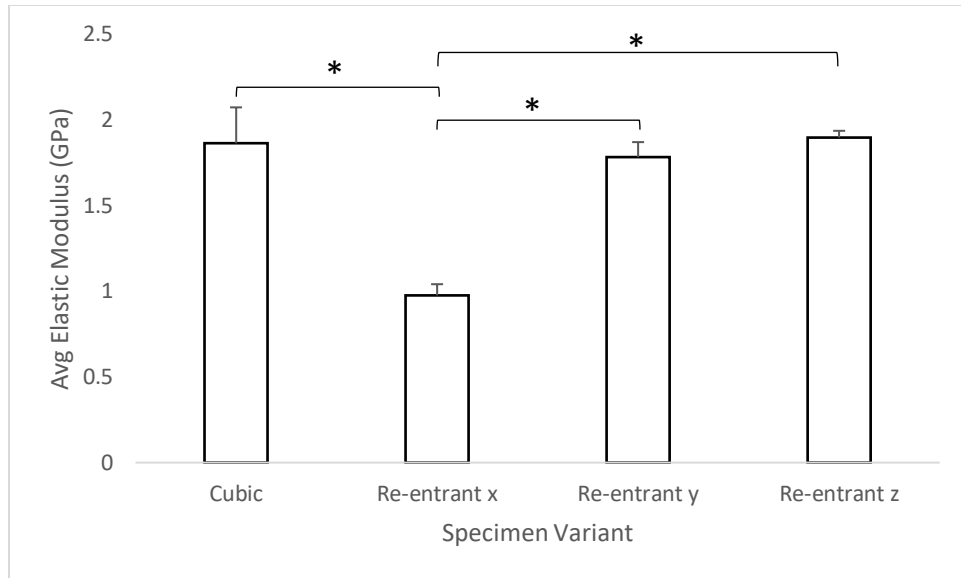
*Figure 69: Apparent Yield Strength  $t$ -Test Summary*

Figure 70 displays a summary of the post hoc Poisson's ratio  $t$ -tests. A line spanning two adjacent bars indicates that the specimen variants were not statistically significant. A statistically significant difference in Poisson's ratio means existed between each specimen variant comparison, aside from the re-entrant y and z-axis comparison. The insignificance between the re-entrant y and z-axis comparison may be due to the orientation being a rotation of the structure.



*Figure 70: Poisson's Ratio t-Test Summary*

A summary of the post hoc apparent elastic modulus t-tests are shown below in Figure 71. The cubic structure was only statistically significant when compared to the re-entrant hexagonal x-axis-oriented structure. The re-entrant hexagonal structure was only significant when comparing its x-axis to its y and z-axes like it was in the previous Poisson's ratio comparison. A summary is not shown for the elongation at yield and fracture strength t-tests because none of the mesoscale structures was statistically significant when compared.



*Figure 71: Apparent Elastic Modulus t-Test Summary*

## CHAPTER FIVE: DISCUSSION

### 5.1 Specimen Variant Comparison

The solid specimen variant was roughly 1.9 to 3.7 times greater in apparent elastic modulus than any of the mesoscale specimen variants. The ANOVA and post hoc t-tests showed that the differences in apparent elastic modulus means were due to the mesoscale structures. The greater apparent modulus values were expected for the solid variant because it had a solid cross-section. However, the interesting fact is that each of the mesoscale specimens had roughly 3.8 times less volume within the necked down region as the solid specimen variant. The cubic specimen had half the elastic modulus as the solid, while only having roughly one-third of the material. Apparent elastic modulus vs. weight ratio is applicable in the aerospace industry because it is important to maximize desirable properties (elastic modulus) while suppressing the less desirable properties (weight) (Al-Shammari & Abdullah, 2018).

The apparent elastic modulus to volume ratio in the necked down region of the solid specimen variant was 1 GPa/315 mm<sup>3</sup>. The ratio was 1 GPa/307 mm<sup>3</sup> for the cubic specimen variant. The ratio ranged from 1 GPa/158 mm<sup>3</sup> to 1 GPa/169 mm<sup>3</sup> for the re-entrant hexagonal specimen variant oriented along each of its axes. Post hoc t-tests indicated that the configuration of the cubic structure was the reason for the difference in elastic moduli means when compared to the re-entrant structure oriented along its x-axis, but not when compared to the y and z-axes because the values were similar. A significant difference in elastic modulus existed when comparing the re-entrant x-axis to its y-axis and its z-axis. However, there was not a significant difference in elastic modulus when comparing the y and z-axes to each other because it was a rotation of the structure. The ratios and statistical comparisons suggest that creating the mesoscale structures on a smaller scale, like the microscale, may result in behavior that is more homogeneous. A smaller scale would allow more struts to be created in the same amount of volume, while maintaining the same solid to open volume ratio. The material properties would then be more identical at each point within the structure, and the structure would be less likely to fracture at the point of connection to a solid member.

The ANOVA showed that there was significance when comparing the Poisson's ratio means of all the specimen variants. The measured Poisson's ratio of the cubic specimen variant was 12% greater than the solid variant, which was similar. Post hoc t-tests showed that the configuration of the cubic structure was not the reason for the difference in Poisson's ratio means when compared to the solid variant, which makes the similar measured values make sense. The re-entrant hexagonal structure oriented along each of its axes had much greater Poisson's ratios than the solid and cubic specimen variants. The ratio was roughly 1.8 to 2.0 times greater when oriented along its y-and z-axes, and was roughly 6.5 to 7.4 greater when oriented along its x-axis. Post-hoc t-tests show that the re-entrant structure oriented along each of its axes was the reason for the differences in Poisson's ratio in both the solid and cubic variants. Again, these statistical results add validity to the measured results. The measured Poisson's ratio results of the re-entrant structure oriented along each of its axes can also be verified when analyzing the statistical results. The analysis shows that there was a statistical difference when comparing the x-axis orientation to the y and z-axis orientation, but shows no significance when comparing the y-axis to the z-axis. The measured results support this analysis being that Poisson's ratio for the x-axis orientation was much greater than the y and z-axes, and similar in the y and z-axes.

An interesting result regarding the Poisson's ratio of the re-entrant structure was that it was negative when oriented along its x-axis. The auxetic behavior was expected because of the hourglass shape of the structure in that orientation. The structure increased in its lateral dimension as it also increased in its axial dimension when an axial load was applied to it, meaning that it became fatter as it was stretched. Auxetic materials are applicable in military operations where lightweight resistance to ballistic and blast damage is desired. Materials like these are ideal for this application due to their negative Poisson's ratio and weight reduction. Lightweight armor systems are used where weight restrictions are introduced, such as in personal protection, helicopters, or boats. The armor systems need to remain lightweight while having the ability to absorb energy and spread it quickly. Auxetic materials absorb and spread energy well because they contract in the directions orthogonal to a compressive load. The material becomes denser because of the orthogonal contraction (Defense Applications of Auxetic Materials, 2019).



Regarding the remaining material properties that were measured, the means of each property (apparent yield strength, elongation at yield, and apparent fracture strength) were significant when compared in the ANOVAs. Post hoc t-test show that the mesoscale structures were the reason for the difference in all the means when comparing the solid structure to each of the mesoscale variants. The measured results support the analysis since the mesoscale specimen variants all had similar means, and these means were all much less than the associated material property mean of the solid variant. The configuration of the cubic structure had no effect on the apparent yield strength when compared to the re-entrant structure oriented along each of its axes, because the mean values were all similar. However, the axis on which the re-entrant structure was oriented had a significant effect on the apparent yield strength when comparing each axis. None of the structures was significant in changing the elongation at yield when compared to each other. The structures did not affect the elongation at yield because they all exhibited a brittle fracture during tensile testing. Post hoc t-tests also concluded that the structures had no statistical significance on the apparent fracture strength when compared to each other, like in the elongation at yield comparisons.

## 5.2 Apparent Elastic Modulus Comparison to Human Bone/Current Implants

Table 12 displays the comparison between the apparent elastic modulus of human bone and the apparent elastic modulus of each specimen variant that was analyzed in this study. The solid specimen variant had a higher elastic modulus than all variants containing mesoscale structures, and roughly one-fourth the modulus of human bone. Each of the specimen variants containing mesoscale structures were 48 to 73% less in modulus than the solid specimen variant because the open area was included in the apparent modulus calculation. The comparison suggests that none of the specimen variants had a modulus equivalent to human bone on a mesoscale. However, the structures may be more homogeneous if created on a smaller scale, such as the microscale. Material properties may improve, possibly eliminating the mesoscale. Research at the University of Michigan focuses on the miniaturization of manufacturing equipment for microscale components and products (Ni, 2021). Miniaturized manufacturing equipment may be ideal for bridging the gap between the microscale and mesoscale.

*Table 12: Apparent Human Bone Apparent Elastic Modulus Comparison*

	Typical Human Radius Elastic Modulus	Typical Cortical Bone Elastic Modulus	Typical Trabecular Bone Elastic Modulus	Solid	Cubic	Re-entrant x	Re-entrant y	Re-entrant z
Modulus (GPa)	16.0	20.7	14.8	3.7	1.86	0.98	1.78	1.90

The relationship between the apparent elastic modulus results in this study, and results in the literature about orthopedic implants, is important since implants were not tested in this study. Titanium alloy implants have a roughly 26 to 30 times increased modulus than the mesoscale structure tested that had the greatest modulus (re-entrant z), and roughly 13.5 to 18.9 times the

modulus of the solid structure. The elastic moduli of the structures tested in this study were significantly less than that of titanium alloy implants. Additional mesoscale structures may be explored that could be greater in elastic modulus than the structures tested in this study. The structure of a spider web may be investigated, being that the spider silk itself had an elastic modulus that was greater than other nylon fibers when compared in a previous study (Ko & Jovicic, 2004).

### **5.3 Limitations**

The experimental findings were not compared to theoretical results. Finite Element Analysis (FEA) may be performed on the variants created in this study. The analysis would supplement the tensile test results by providing a comparison to the measured material property values.

In addition, the sample size was small. This was by design in order to reduce the cost of this exploratory study when the findings were unknown. However, due to the loss of samples during processing, in one instance only three of the planned five samples were available for testing. As a result, there may be additional cases where significant differences exist, but could not be detected due to low sample size.

## CHAPTER SIX: CONCLUSIONS

It was found that mesoscale structures could be used to reduce the elastic modulus of a 3D printed metal part while retaining the overall exterior shape. Dramatic change in elastic modulus is possible. The modulus of the 316l Stainless Steel structures created with DMLS were found to be, at most, roughly one-fourth that of human bone. Titanium alloy orthopedic implants were determined to be up to 30 times greater in elastic modulus than the mesoscale structures. Additional mesoscale structures that may increase the modulus could be investigated in the future, such as the structure of spider silk.

In addition, use of mesoscale structures enabled the Poisson's ratio to be altered as well. The Poisson's ratio for the re-entrant hexagonal x-axis-oriented specimen was negative, by design, and this auxetic behavior was observed in the physical experiments. The ability to control this parameter in a material could have wide reaching implications. A particular application for auxetic materials exists during military operations. They exhibit ideal properties for combat armor due to their negative Poisson's ratio when a compressive load is applied.

Future research may include creating sequential mesoscale structure specimens, like the ones created in this study, but varying the lengths and widths of the struts within the structures. By doing this, a table could be created in order to make correlations between the dimensional values of the struts and the resulting elastic moduli values. The dimensions of the struts of the structure may be directly correlated to the modulus of the structure itself. Furthermore, as 3D printing capabilities increase, utilizing a smaller scale mesoscale structure may create structures that are more homogeneous. The use of smaller scale structures may improve material properties.

One may also investigate the effect that the build orientation of the struts created with DMLS has on the elastic modulus of the mesoscale structure. The direction that the laser sinters the struts of the structure may have a direct effect on the strain values of the created structure. Increasing the strain values of mesoscale structures created with DMLS would enable the creation of structures that are higher in elastic modulus.

## REFERENCES

- AIP Publishing. (2015, December). *Review of Selective Laser Melting: Materials and Applications*. Retrieved from Applied Physics Reviews:  
<http://aip.scitation.org/doi/abs/10.1063/1.4935926?journalCode=are&>
- Al-Shammari, M. A., & Abdullah, S. E. (2018). Stiffness to Weight Ratio of Various Mechanical and Thermal Loaded Hyper Composite Plate Structures. *2nd International Conference on Engineering Sciences* . Kerbala: IOP Publishing.
- Bosisio, M. R., Talmant, M., Skalli, W., Laugier, P., & Mitton, D. (2006). Apparent Young's modulus of human radius using inverse finite-element method . *Journal of Biomechanics*.
- Burnett, C. (2016, 3 22). *Metal Strength and Stiffness: What's the Difference?* Retrieved from Thermo Fisher Scientific: <https://www.thermofisher.com/blog/metals/metal-strength-and-stiffness-whats-the-difference/>
- Chao, J. (2015, March 5). *Between Micro and Macro, Berkeley Lab Mathematicians Model Fluids at the Mesoscale*. Retrieved from Berkeley Lab:  
<https://newscenter.lbl.gov/2015/03/05/micro-macro-berkeley-lab-mathematicians-model-fluids-mesoscale/>
- Cheruvu, B., Venkatarayappa, I., & Goswami, T. (2019). Stress Shielding in Cemented Hip Implants Assessed from Computed Tomography. *Biomedical Journal of Scientific and Technical Research*.
- Dallas, M. E. (2019). The 10 Most Common Surgeries in the U.S. . *healthgrades*.
- Defense Applications of Auxetic Materials*. (2019, 11 2). Retrieved from Defense Systems Information and Analysis Center: <https://www.dsiac.org/resources/articles/defense-applications-of-auxetic-materials/>

- Douglass E. Padgett, M., & Russel E. Windsor, M. (2013, 8 13). *Understanding Implants in Knee and Hip Replacement*. Retrieved from Hospital for Special Surgery:  
[https://www.hss.edu/conditions\\_understanding-implants-in-knee-and-hip-replacement.asp](https://www.hss.edu/conditions_understanding-implants-in-knee-and-hip-replacement.asp)
- Engineers Edge. (2020, 10 1). Poissons's Ratio Definition Equation. Retrieved from  
<http://www.instron.us/en-us/our-company/library/test-types/tensile-test>
- EOS. (2017). *EOS M 290*. Retrieved from Electro Optical Systems: <https://www.eos.info/eos-m290>
- EOS. (2017). *Welcome to EOS*. Retrieved from Electro Optical Systems: <https://www.eos.info/en>
- Hart, N., Nimphius, S., Rantalainen, T., Ireland, A., Siafarikas, A., & Newton, R. (2017). Mechanical basis of bone strength: influence of bone material, bone structure and muscle action. *Journal of Musculoskeletal and Neuronal Interactions*, 114-139.
- Hendrickson, J. W. (2015). *Use of Direct Metal Laser Sintering for Tooling in High Volume Production*. Utah: All Graduate Plan B and other Reports.
- Hu, H., & Zulifqar, A. (2017). Auxetic textile materials - A review . *Journal of Textile Engineering and Fashion Technology*.
- Instron. (2017). *Tensile Testing*. Retrieved from Instron: <http://www.instron.us/en-us/our-company/library/test-types/tensile-test>
- Ko, F., & Jovicic, J. (2004). Modeling of Mechanical Properties and Structural Design of Spider Web. *Biomacromolecules*.
- Lindstrom, A. (2012, December 6). *Selective Laser Sintering, Birth of an Industry*. Retrieved from The University of Texas at Austin Mechanical Engineering:  
<http://www.me.utexas.edu/news/news/selective-laser-sintering-birth-of-an-industry>

- Linke, R. (2017, December 7). *Additive manufacturing, explained*. Retrieved from MIT Management Sloan School: <https://mitsloan.mit.edu/ideas-made-to-matter/additive-manufacturing-explained>
- Mayo Clinic. (2014). First nationwide prevalence study of hip and knee arthroplasty shows 7.2 million Americans living with implants. *American Academy of Orthopedic Surgeons*.
- Morgan, E. F., Unnikrisnan, G. U., & Hussein, A. I. (2018). Bone Mechanical Properties in Healthy and Diseased States. *US National Library of Medicine*.
- NDT Resource Center. (2018). *Stress and Strain*. Retrieved from NDT Resource Center: <https://www.nde-ed.org/EducationResources/CommunityCollege/Materials/Mechanical/StressStrain.htm>
- Ni, J. (2021). *Micro/Meso-scale Manufacturing Systems*. Retrieved from Michigan Engineering: [https://wumrc.engin.umich.edu/research/micro\\_man/](https://wumrc.engin.umich.edu/research/micro_man/)
- PennState. (2021). *S.3.1 Hypothesis Testing (Critical Value Approach)*. Retrieved from PennState Elberly College of Science: <https://online.stat.psu.edu/statprogram/reviews/statistical-concepts/hypothesis-testing/critical-value-approach>
- Rho, J. Y., Ashman, R. B., & Turner, C. H. (1991). Young's modulus of trabecular and cortical bone material: Ultrasonic and microtensile measurements. *Journal of Biomechanics*.
- Rodriguez-Ramirez, J., Mendez-Lagunas, L., & Torres, S. S. (2012). True Density and Apparent Density During the Drying Process for Vegetables and Fruits: A Review. *Journal of Food Science*.
- Scheker, J. (2015). *Closing the Mesoscale Gap*. Los Alamos: Los Alamos National Laboratory.



- Science Alert. (2007, March). *Problem of Stress Shielding and Improvememnt to the Hip Implant Designs: A Review*. Retrieved from Science Alert: An Open Access Publisher:  
<http://scialert.net/fulltext/?doi=jms.2007.460.467&org=11>
- Science Direct. (2021). *Stress Concentration Factor*. Retrieved from Science Direct:  
<https://www.sciencedirect.com/topics/engineering/stress-concentration-factor>
- Siegle, D. (n.d.). *Educational Research Basics*. Retrieved from Univeristy of Connecticut:  
<https://researchbasics.education.uconn.edu/t-test/#>
- Statistics How To. (2021). *The Practically Cheating Statistics Handbook*. Retrieved from Statistics How to: <https://www.statisticshowto.com/probability-and-statistics/f-statistic-value-test/>
- Straffellni, G., Fontanari, V., & Molinari, A. (1999, February). *True and apparent Young's modulus in ferrous porous alloys*. Retrieved from Science Direct:  
<https://www.sciencedirect.com/science/article/abs/pii/S0921509398009605>
- Surgeons, A. A. (2016, April). *Knee Replacement Implants*. Retrieved from OrthoInfo:  
<https://orthoinfo.aaos.org/en/treatment/knee-replacement-implants/>
- Tang, Y., & Zhao, Y. F. (n.d.). *A survey of the design methods for additive manufacturing to improve functional performance*. Montreal: Department of Mechanical Engineering, McGill University.
- Tapscott, D. C., & Wattowa, C. (2020). Orthopedic Implant Materials. *National Center for Biotechnology Information*.
- U.S. Food & Drug Administration. (2019, 30 9). *Implants and Prosthetics*. Retrieved from U.S. Food & Drug Administration: <https://www.fda.gov/medical-devices/products-and-medical-procedures/implants-and-prosthetics>

University of Michigan. (n.d.). *BME 332: Introduction to Biosolid Mechanics*. Retrieved from  
University of Michigan: <http://umich.edu/~bme332/ch9bone/bme332bone.htm>

University of Wisconsin-Madison. (2017). *Negative Poisson's ratio materials: names- anti-rubber, auxetic, dilational*. Retrieved from University of Wisconsin-Madison:  
<http://silver.neep.wisc.edu/~lakes/PoissonFAT.html>

Zhang, X., & Yang, D. (2016). Mechanical Properties of Auxetic Cellular Material Consisting of Re-Entrant Hexagonal Honeycombs. *MDPI*.